Modified chitosan nano-substrates for mycobacterial capture

by

Lisa Fortuin

Thesis presented in partial fulfilment of the requirements for the degree

Master of Science in Chemistry and Polymer Science at

Stellenbosch University

Supervisor: Dr. Lizl Cronje

December 2015

Declaration

By submitting this thesis/dissertation electronically, I declare that the entirety of the work contained therein is my own, original work, that I am the sole author thereof (save to the extent explicitly otherwise stated), that reproduction and publication thereof by Stellenbosch University will not infringe third party rights and that I have not previously in its entirety or in part submitted it for obtaining any qualification.

December 2015

Abstract

Tuberculosis (TB) is one of the world's deadliest diseases, with one third of the population being infected by it. The diagnosis of active tuberculosis entails finding and identifying *Mycobacterium tuberculosis (Mtb)*, the causative pathogen in a specimen of bodily fluid from the patient. Multiple samples will improve the diagnostic yield and specimen volumes should therefore be as large as possible, which is often challenging for patients and especially younger children. Alternatively, a smaller volume could be required if there was a manner in which to concentrate the bacteria within a specimen, through use of a substrate which has an affinity for the pathogenic species. Polymers having intrinsic cellular activity are of interest as such substrates, one such being the natural polysaccharide, chitosan.

In this thesis, a variety of modified chitosan derivatives were prepared as potential *Mtb*-capturing substrates. This was achieved by modifying chitosan with a variety of moieties, selected based on possible interactions with the *Mtb* cell wall, to render various quaternary ammonium salts of the polymer chitosan. The quaternized chitosan derivatives were then used to synthesize nano-substrates having an affinity for *Mtb*. Polymer coated superparamagnetic magnetite nanoparticles (SPMNs) were synthesized via an *in situ* co-precipitation technique, in which modified chitosan is able to chelate with the metal core. Polymer nanofibers were also electrospun via the electrospinning technique. The prepared derivative, *N*-trimethylammonium chitosan chloride (TMC), was electrospun into nanofibers by blending with suitable non-ionogenic polymers, namely polyvinyl alcohol (PVA), polyethylene oxide (PEO), polyvinyl pyrrolidone (PVP) and polyacrylamide (PAM), required to facilitate nanofiber formation.

Affinity studies were conducted between the modified chitosan nano-substrates and the bacillus Calmette-Guérin (BCG) strain of *Mycobacterium bovis*, the attenuated *Mtb*-mimic bacteria, for evaluation as mycobacterium capturing substrates. The successful capture of BCG onto the surfaces of the various modified chitosan nanofibers and modified chitosan coated superparamagnetic nanoparticles was confirmed by fluorescence microscopy (FM), light microscopy (LM), transmission electron microscopy (TEM) and field emission scanning electron microscopy (FE-SEM). Analysis of the FM, TEM and FE-SEM images indicated that the chitosan coated nanoparticles functionalized with a C_{12} aliphatic quaternary ammonium moiety (CS-qC_{12}), captured the most BCG through a combination of ionic and hydrophobic interaction. TMC blended with PVA, to produce nanofibers crosslinked with genipin, were found to have the strongest interaction with BCG of the nanofibrous mats tested. These findings were corroborated by water contact angle measurements, which established that PVA was the least hydrophilic of the non-ionogenic polymers and had hydrogen bond donating groups only, factors influencing the cellular adhesive properties of affinity substrates.

Opsomming

Tuberkulose (TB) is een van die wêreld se mees dodelikste siektes, met ‘n derde van die bevolking wat geïnfekteer is daarmee. Ten einde aktiewe TB te diagnoseer moet *Mycobacterium tuberculosis (Mtb)*, die voorsakende patogeen in ’n monster van die pasiënt se liggaamlike vloeistof, gevind en ïdentifiseer word. Veelvuldige monsters sal die diagnotiese opbrengs verhoog en monster volumes moet dus so groot as moontlik wees wat dikwels ’n uitdaging vir pasiënte en veral jonger kinders kan bied. Alternatiewelik kan ’n kleiner monster van die pasiënt vereis word indien daar ’n manier was om die bakterieë in ’n monster te konsentreer deur die gebruik van ’n substraat wat ’n affiniteit toon vir die patogeniese spesie. Polimere met ’n intrinsieke sellulêre aktiwiteit, wek belangstelling as sodanige substraat, een synde die natuurlike polisakkaried, chitosan.

In hierdie tesis is ’n verskeidenheid gemodifiseerde chitosan afgeleides voorberei as potensiële *Mtb*-vaslegging substrate. Dit is gedoen deur chitosan te modifiseer met ’n verskeidenheid funksionele groepe, gekies op grond van moontlike interaksies met die *Mtb* selwand, ten einde ’n verskeidenheid kwaternêre ammonium soute van die chitosan polimeer te bekom. Die kwaternêre chitosan afgeleides is gevolglik gebruik om nano-substrate te sintetiseer wat ’n affiniteit toon vir *Mtb*. Polimeer bedekte superparamagnetiese magnetiet nanopartikels (SPMNs) is gesintetiseer via ’n *in situ* mede-neerslag metode, waarvolgens die gemodifiseerde chitosan polimere in staat is om met die metaal kern te chelaat. Polimeer nanovesels is ook geëlektrospin deur die elektrospin tegniek te gebruik. Die voorbereide afgeleide *N*-trimetielammonium chitosan chloried (TMC) is tot nanovesels geëlektrospin deur vermenging met geskikte nie-ionogeniese polimere, naamlik poliviniel-alkohol (PVA), polietilene-oksied (PEO), poliviniel-pirrolidoon (PVP) en poliakrielamied (PAM), wat vereis word ten einde nanovesels te produseer.

Affiniteit studies is uitgevoer tussen die gemodifiseerde chitosan nano-substrate en die bacillus Calmette-Guérin (BCG) stam van *Mycobacterium bovis,* die verswakte *Mtb*-mimiek bakterieë vir evaluering as mycobakterium-vaslegging substrate. Die suksesvolle vasvang van BCG op die oppervlaktes van die verskillende gemodifiseerde chitosan nanovesels en gemodifiseerde chitosan bedekte SPMNs is bevestig deur fluoressensie mikroskopie (FM), lig mikroskopie (LM), transmissie elektron mikroskopie (TEM) en veld-emissie-skandering elektron mikroskopie (FE-SEM). Analise van die FM, TEM en FE-SEM beelde het getoon dat die chitosan bedekte nanopartikels met byvoeging van ’n C_{12} alifatiese kwaternêre ammonium groep, die meeste BCG vasgevang het deur ’n kombinasie van ioniese en hidrofobiese interaksie. TMC vermeng met PVA om nanovesels te vorm, gekruisbind met genipin, is gevind om die sterkste interaksie met BCG te toon. Hierdie bevindings is bevestig deur water-kontak-hoek-metings, wat getoon het dat PVA die minste hidrofilies van die nie-ionogeniese polimere was en slegs waterstof-binding skenkings groepe het, alles faktore wat die sellulêre bindingskwaliteite van affiniteit-substrate sal beïnvloed.

Acknowledgements

First and foremost I would like to thank my supervisor and mentor, Dr. Lizl Cronje for her guidance and support throughout this project and my postgraduate studies. One simply could not wish for a better supervisor.

I would like to thank all of the staff at the Department of Chemistry and Polymer Science, especially Calvin Maart, Jim Motshweni, Deon Koen, Aneli Fourie and Erinda Cooper; as well as Adine Gericke and Professor Mallon, for their kindness and support throughout my studies.

I would like to thank the staff of the Central Analytical Facility: Lize Engelbrecht (and Rozanne) for their time, expertise and creative problem solving in obtaining incredible FM images; Madeleine Frazenburg for her special effort with SEM and EDX analyses; Elsa Malherbe for NMR analyses; Dr Vincent Smith for P-XRD training and analyses as well as Prem Lama for conducting BET analyses.

I would like to thank Mohammed Jaffer for his skill and availability in TEM imaging at UCT and I would like to extend a special thank you to Tiaan Heunis from the Biomedical Tuberculosis Research Centre of SU, for growing the BCG cultures and for the friendliness and aid during all of the experiments conducted at Tygerberg Medical Campus.

I would like to thank the Olefins Research group as well as Professor van Reenen and Dr Lutz. Friday's group meetings were always pleasant and constructive. I'd like to thank Divann, who made sure that the laboratory ran smoothly and I would also like to thank Elrika Harmzen, for her knowledge and time spent over the years.

I would like to thank my parents and grandparents. My achievements and strengths are as a result of their unconditional love and support in every way. To my sisters, you bring such sunshine into in my life. Words cannot describe the appreciation I feel to have been blessed with such an incredible family. I'd also like to thank Walter and his family for the abundance of love and motivation along the way.

Lastly, I would like to thank the Stellenbosch University and the National Research Foundation for financial support during my studies.

Table of Contents

List of Figures

List of Schemes

List of Tables

List of Abbreviations and Acronyms

γ-Fe_2O_3	Maghemite
$\propto$-Fe_2O_3	Hematite
AcOH	Acetic acid
$AgNO_3$	Silver Nitrate
ATR-FTIR	Attenuated total reflectance Fourier transform infrared
BCG	Bacillus Calmette–Guérin
BET	Brunauer, Emmett and Teller
CFDA,SE	Carboxyfluorescein diacetate succinimidyl ester
Co	Cobalt
CS	Chitosan
CS-qC_8	*N*-propyl-3-*N',N'*-dimethyl-*N'*-octylammonium chitosan chloride
CS-qC_{10}	*N*-propyl-3-*N',N'*-dimethyl-*N'*-decylammonium chitosan chloride
CS-qC_{12}	*N*-propyl-3-*N',N'*-dimethyl-*N'*-dodecylammonium chitosan chloride
DA	Degree of *N*-acetylation
DAPI	4',6-diamidino-2-phenylindone
DDA	Degree of *N*-deacetylation
DNA	Deoxyribonucleic acid
DOM	Degree of *O*-Methylation
ELISA	Enzyme-linked immunosorbent assay
FCC	Face-centred cubic
Fe	Iron
Fe^{2+}	Ferrous ion
Fe^{3+}	Ferric ion
Fe_3O_4	Magnetite
$Fe(OH)_3$	Iron(III) oxide-hydroxide
FE-SEM	Field emission scanning electron microscopy

FM	Fluorescence microscopy
$FeTiO_3$	Ilmenite
GA	Glutaraldehyde
GlcN	2-amino-2-deoxy-β-d-glycopyranose
GlcNAc	2-acetamide-2-deoxy-β-d-glycopyranose
GTMAC	Glycidyltrimethylammonium chloride
HIV/AIDS	Human immunodeficiency virus infection and acquired immune deficiency syndrome
HTCC	*N*-(2-hydroxy)propyl-3-trimethylammonium chitosan chloride
IR	Infrared
LM	Light Microscopy
MDR-TB	Multidrug-resistant tuberculosis
N	Nickel
NMP	*N*-methyl-2-pyrrolidone
NMR	Nuclear magnetic resonance
PAM	Polyacrylamide
PBS	Phosphate buffered solution
PCR	Polymerase chain reaction
PEO	Polyethylene oxide
pH	Power of hydrogen ion
ppm	Parts per million
PVA	Polyvinyl alcohol
PVP	Polyvinyl pyrrolidone
P-TB	Pulmonary tuberculosis
P-XRD	Powder X-ray diffraction
SEM	Scanning electron microscopy
SPMNs	Superparamagnetic magnetite nanoparticles
SQUID	Superconducting quantum interference device
TB	Tuberculosis

TEM	Transmission electron microscopy
TGA	Thermogravimetric analysis
TMC	*N*-trimethylammonium chitosan chloride
TPP	Sodium tripolyphosphate
XDR-TB	Extensively drug-resistant tuberculosis
ZN	Ziehl-Neelsen

List of Symbols

λ	X-ray wavelength
ρ	Density
Å	Angstrom
C	Concentration
D_m	Average size of magnetic domains
D_P	Average size of crystallite domains
E	Electric field strength
H	External magnetic field
H_C	Coercivity
m	Mass
M_W	Weight average molecular weight
M	Magnetization
M_S	Saturation magnetization
M_r	Remanent magnetization
V	Volume
k	Dimensionless shape factor
k_B	Blotzmann's constant
K	Kelvin
kV	Kilovolts

Chapter One

Prologue

1.1 Introduction

Tuberculosis (TB) is one of the world's deadliest diseases, with one third of the population being infected by it.[1] The relatively poor performance of existing TB test methods and the lack of suitable tools for both diagnosis and susceptibility testing in developing and high-disease burden countries leaves many patients undiagnosed or mismanaged.[2] Diagnostic examination of bacterial infections is limited by the difficulty to detect in a specific manner, low populations of bacteria. The diagnosis of active tuberculosis entails finding and identifying the *Mycobacterium tuberculosis*, the causative pathogen in a specimen of bodily fluid from the patient. Obtaining good quality specimens, containing the highest possible numbers of mycobacteria is therefore integral to the fast and accurate diagnosis of TB.[3] Multiple samples will improve the diagnostic yield and specimen volumes should be as large as possible,[4] which is often challenging for patients and especially younger children. Alternatively, a smaller volume could be required from the patient if there was a manner in which to concentrate the bacteria within a specimen of sputum, through use of a substrate which has an affinity for the pathogenic species.

Polymers having intrinsic cellular activity are of interest as such substrates. The natural polysaccharide, chitosan, is reported to possess advantageous biological properties, for example, biocompatibility and biodegradability, non-toxicity, intrinsic antibacterial properties and bioadhesive function. Quaternized derivatives of chitosan have exhibited higher bacterial activity and a broader range of activity towards bacteria.[5-7] Combining new knowledge of nanotechnology and polymer science with the existing knowledge of cellular and molecular functions, is allowing for the development of novel and advanced tactics in which to address devastating diseases, of which TB is but one.

Nanotechnology entails the use of materials in the nanoscale, lending unique and tuneable properties to those materials with high specific surface areas and high aspect ratios, making them

ideal substrates for the capture and concentration of bacteria by the appropriate physical and chemical modifications. Quaternized chitosan can chelate to metallic nanoparticles to form a smooth continuous coating on the metal core; and nanofibers can be electrospun from quaternized chitosan by using the electrospinning technique.[8]

Superparamagnetic nanoparticles are of exceptional interest due to their unique and controllable properties such as magnetism, size, shape, crystallinity and possible functionality with targeting ligands, drugs and fluorescence–directing research evermore towards biomedical applications. The co-precipitation technique is a synthetic archetype where ferrous and ferric ions are co-precipitated in a basic solution, which could be achieved in the presence of coating materials such as quaternized chitosan.[9,10] The volume of pathogenic bacteria within a specimen could therefore be concentrated and immobilized for further diagnostic analysis by inducing an external magnetic field which will ultimately aid the fast and accurate diagnosis of TB.

1.2 Objectives

The basic motivation for this work was to develop a capturing substrate for *Mycobacterium tuberculosis (M. tuberculosis)* able to capture and concentrate the pathogenic mycobacteria within a specimen from the patient being investigated. For this purpose, the polysaccharide chitosan was chosen as polymer to be modified with chemical moieties selected based on possible interactions with the *M. tuberculosis* cell wall. For the primary objective to be met, suitable nano-substrates should be synthesized through the use of modified chitosan polymers having an affinity for *M. tuberculosis*. Due to high specific surface areas and tuneable properties, the nano-substrates of interest were modified chitosan coated superparamagnetic magnetite nanoparticles (SPMNs) and electrospun modified chitosan nanofibers. A suitable non-ionogenic polymer is necessary to facilitate the electrospinning of modified chitosan and these polymers were evaluated for blending with modified chitosan to produce bi-component nanofibers able to bind to mycobacteria. The modified chitosan bi-component nanofibers and coated superparamagnetic nanoparticles should be evaluated as potential capturing platforms for *Mycobacterium bovis* bacillus Calmette-Guérin (BCG) as the attenuated virulent strain of *M. tuberculosis*.

The objectives of the study can therefore be summarized as follows:

1. To synthesize and characterize the following quaternized chitosan polymers, based upon the chemical modification of the parent polymer, chitosan*:*

    a. *N*-trimethylammonium chitosan chloride (TMC)

b. *N*-(2-hydroxy)propyl-3-trimethylammonium chitosan chloride (HTCC)
c. *N*-propyl-3-*N',N'*-dimethyl-*N'*-octylammonium chitosan chloride (CS-qC_8)
d. *N*-propyl-3-*N',N'*-dimethyl-*N'*-decylammonium chitosan chloride (CS-qC_{10})
e. *N*-propyl-3-*N',N'*-dimethyl-*N'*-dodecylammonium chitosan chloride (CS-qC_{12})

2. To synthesize and characterize the superparamagnetic iron oxide (magnetite) nanoparticles (SPMNs) and SPMN nanocomposites created via *in situ* coating with the aforementioned quaternized chitosan polymers.

3. The formation, crosslinking and characterization of bi-component nanofibers consisting of TMC blended with suitable non-ionogenic polymers, which include polyvinyl alcohol (PVA), polyethylene oxide (PEO), polyacrylamide (PAM) and polyvinyl pyrrolidone (PVP), necessary to facilitate the electrospinning of modified chitosan.

4. To evaluate and compare the interaction of mycobacteria and the modified chitosan/non-ionogenic polymer blend nanofibers through the use of TMC blended with PVA, PEO, PVP and PAM.

5. To evaluate and compare the interaction of mycobacteria and the modified chitosan coated SPMNs which include TMC SPMNs, HTCC SPMNs, CS-qC_8 SPMNs, CS-qC_{10} SPMNs and CS-qC_{12} SPMNs.

1.3 Layout of Thesis

1.3.1 Chapter 1 | Prologue

A brief introduction is provided and a clear overview of the specific aims and objectives to be met in this study are discussed.

1.3.2 Chapter 2 | Historical and theoretical background

This chapter introduces the historical and theoretical aspects that relate to the work within this thesis.

1.3.3 Chapter 3 | Precursor polymers

This chapter describes the characterization of pristine chitosan and the synthesis and characterization of quaternized chitosan polymers, namely TMC, HTCC and quaternized *N*-alkyl chitosan derivatives of varying aliphatic chain lengths (CS-qC_8, CS-qC_{10} and CS-qC_{12}).

1.3.4 Chapter 4 | Synthesis and characterization of superparamagnetic magnetite nanoparticles and nanocomposite materials

This chapter details the synthesis and characterization of superparamagnetic magnetite nanoparticles (SPMNs) and SPMN nanocomposite materials constituting a SPMN core and a polymeric coating of quaternized chitosan.

1.3.5 Chapter 5 | Chitosan based bi-component nanofibers

This chapter describes the formation of bi-component polymeric nanofibers of *N*-trimethylammonium chitosan chloride (TMC) blended with suitable non-ionogenic polymer partners to facilitate electrospinning as well as the subsequent crosslinking to produce aqueous stability.

1.3.6 Chapter 6 | Affinity studies between modified chitosan nano-substrates and mycobacteria

This chapter presents the evaluation of modified chitosan bi-component nanofibers and coated superparamagnetic nanoparticles as potential capturing platforms for *M. bovis* BCG, the attenuated virulent strain of *M. tuberculosis*.

1.3.7 Chapter 7 | Conclusions and recommendations

This chapter provides a short summary of the conclusions gathered from this study. It also discusses the challenges encountered and possible solutions for future work.

1.4 References

1. Sudre, P.; ten Dam, G.; Kochi, A. *Bull. World Health Organ.* **1992**, *2,* 149-159.
2. Cohen, G. M. *AIDS* **2007**, S81-7.
3. Liandris, E.; Gazouli, M.; Andreadou, M.; Čomor, M.; Abazovic, N.; Sechi, L. A.; Ikonomopoulos, J. *J. Microbiol. Methods* **2009**, *3,* 260-264.
4. Yeni, P.; Hance, J. *Am. Rev. Respir. Dis.* **1993**, 420-424.
5. Mrksich, M. *Curr. Opin. Chem. Biol.* **2002**, *6,* 794-797.
6. Gray, J. W. *Clin. Biochem.* **2004**, *6,* 450-455.
7. Ignatova, M.; Starbova, K.; Markova, N.; Manolova, N.; Rashkov, I. *Carbohydr. Res.* **2006**, *12,* 2098-2107.
8. Vinsova, J.; Vavrikova, E. *Curr. Pharm. Des.* **2011**, *32,* 3596-3607.
9. Akbarzadeh, A.; Samiei, M.; Davaran, S. *Nanoscale Res. Lett.* **2012**, *1,* 1-13.
10. Jia, Y.; Demopoulos, G. P. *Water Res.* **2008**, *3,* 661-668.

Chapter Two

Historical and Theoretical Background

2.1 Tuberculosis

2.1.1 Introduction

Tuberculosis (TB) is second only to HIV/AIDS as the greatest cause of death worldwide due to a single infectious agent. In 2012 alone, 8.6 million people fell ill with TB and 1.3 million people died of TB, despite it being a curable and preventable disease. Over 95% of deaths attributed to TB occur in low- and middle-income countries.[1] In recent years, substantial efforts have been made to revive control activities currently under way. This is occurring largely because of the increased occurrence of TB in many HIV-epidemic countries such as South Africa as well as the realisation that TB control is one of the most cost-effective health interventions in developing countries.[2,3] The currently available vaccine strain *Mycobacterium bovis* Bacillus Calmette–Guérin (BCG) provides some defence against childhood tuberculosis, but its protective capacity against the most common form, pulmonary tuberculosis in adults, is insufficient and highly variable.[4]

TB is caused by the pathogenic bacterial species called *Mycobacterium tuberculosis* (*M. tuberculosis*) and is transmitted by the inhalation of 1 - 5 µm droplet nuclei (refer to Figure 2.1 for a scanning electron microscopy image of *M. tuberculosis*). These pathogen containing droplets are of respiratory secretions and are ejected into the air by coughing, sneezing, and talking. Each cough could potentially expel up to 600 000 droplet nuclei.[5] The infectious droplet nuclei are inhaled and lodge in the alveoli in the distal airways. *M. tuberculosis* is then taken up by alveolar macrophages, initiating a cascade of events to result in either the effective inhibition of the infection or the progression to active tuberculosis.[6,7]

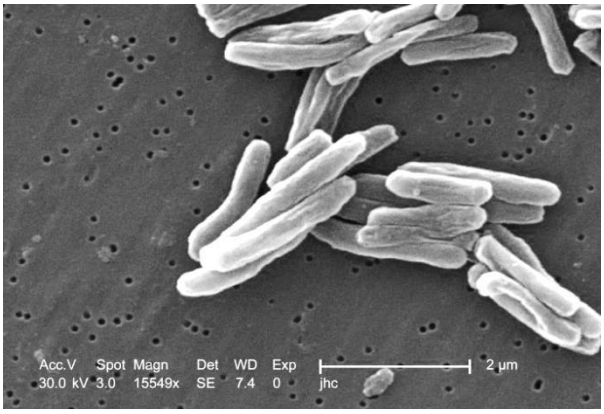

Figure 2.1 Mycobacterium tuberculosis scanning electron micrograph.

M. tuberculosis is a moderately large rod-shaped, non-motile bacterium, indistinctly related to the Actinomycetes. The bacteria are approximately 2 - 4 µm in length and 0.2 - 0.5 µm in width. Larger bacterial colonies tend to amass together. *M. tuberculosis* is an obligate aerobe, which explains why, in the classical case of TB, its complexes are found in the well-aerated upper lobes of the lungs. The bacterium is a facultative intracellular parasite, usually of macrophages. It has a slow generation time of 15 - 20 h, a physiological feature that may contribute towards its virulence.[8] *M. tuberculosis* has a dense cell wall, which is characteristic of the genus *Mycobacterium*. The cell wall has characteristics of both Gram-positive and Gram-negative bacteria and provides an excellent permeability barrier, providing resistance to a large range of antimicrobial agents.[9]

2.1.2 Diagnosis of TB

There are substantial resource constraints for the diagnosis and treatment of TB in low- and middle-income countries. The relatively poor performance of current TB test methods and the lack of suitable tools for both diagnosis and susceptibility testing in developing and high-disease burden countries leaves many patients undiagnosed or mismanaged. Consequently, more than 400 000 new cases of multidrug-resistant TB (MDR-TB) are being reported annually, and the situation has become worse with the emergence of extensively drug-resistant TB (XDR-TB).[1,3] Reliable diagnosis of TB depends on laboratory confirmation, but traditional diagnostic procedures have long been recognized as being less than optimal. In recent years, several new diagnostic techniques have been developed to improve the speed and reliability of TB diagnosis. None of these, however, have proven to be a diagnostic 'gold standard'.[10] In developing countries, prominence is placed on passive case finding which is based on diagnosing infectious cases of tuberculosis primarily through direct microscopy of sputum specimens obtained from persons who present themselves to the health facilities.[11] Many countries still depend on a long-used method called sputum smear microscopy to diagnose TB, where trained laboratory technicians observe sputum samples under a microscope to see if TB bacteria are present.

Diagnostic investigation of mycobacterial infections is limited by the difficulty to detect low populations of mycobacteria, or the immunology markers associated with the infections they cause, in a specific manner. The laboratory diagnostic investigation of mycobacterial diseases relies on the light microscopy observation of hematoxylin–eosin (H&E) or Ziehl–Neelsen (ZN) stained sections, mycobacterial culture, the ELISA test and DNA amplification techniques. Each of these approaches has certain benefits and limitations but in general, those with high specificity and low minimum detection limits are usually complex and expensive.[12-15] In most cases the reliable application of these diagnostic methods requires highly trained personnel and very often, dedicated equipment that can be of considerable cost.

The diagnosis of active TB entails finding and identifying the bacterium within a specimen of bodily fluid from the patient. In most cases, *M. tuberculosis* infects the lungs and the bacterium can thus be found in sputum. Sputum is a thick bodily fluid originating in the lower airways, and is usually coughed up.[16] Many people, and especially children, have difficulty in coughing up sputum. It can then be induced by inhaling saline air through a mask, called a nebulizer. The diagnosis of pulmonary tuberculosis (P-TB) presents challenges in children, as symptoms are non-specific and specimens are challenging to obtain. Adequate diagnosis of pediatric TB is especially difficult due to lack of sputum production and scarcity or absence of organisms in respiratory secretions, as TB bacilli typically remain confined to perihilar nodes that do not rupture into the bronchus.[17]

Accurate, rapid microbiological diagnosis of TB and other bacterial infections starts with proper specimen collection.[18] Irrespective of which specimen test method is used as the basic model, most laboratory techniques depend upon the detection of mycobacteria,[19] and obtaining good quality specimens containing the highest numbers of mycobacteria is therefore integral to the diagnosis of TB. More than one sample will improve the diagnostic yield, and specimen volumes should be as large as possible. To provide the best results, the volume of a specimen from the patient should exceed 5 mL.[20] Alternatively, a smaller volume of sputum could be required if there was a manner in which to concentrate the mycobacteria within a sample of sputum or bodily fluid. Combining the new knowledge of nanotechnology and polymer science with existing knowledge of cellular and molecular functions is allowing for the development of novel and advanced techniques in which to address devastating diseases such as TB.

2.2 Nanotechnology

Nanotechnology can be defined as the science and engineering involved in the design, synthesis, characterization and application of materials and devices whose smallest functional organization in at least one dimension is on the nanometre scale, one billionth of a meter.[21] In the last decade, nanotechnology has advanced to such an extent that it has become possible to fabricate, characterize and specifically tailor the functional properties of nanoparticles and nanofibers for biomedical applications and diagnostics. The application of nanotechnology for the treatment, diagnosis, monitoring and control of biological systems is referred to as 'nanomedicine' by the National Institutes of Health. The potential of nanomedicine includes the development of nanoparticles for diagnostic and screening purposes, DNA sequencing, manufacture of drug delivery systems and single virus detection. Nanotechnology has opened vast and new vistas in biomedical research.[22-24]

Previous studies have focused on improving existing TB test methods through the use of nanotechnology in the design of affinity substrates/capturing platforms to facilitate the capture and concentration of *M. tuberculosis* for improved diagnosis. In a study done by Cronje, poly(styrene-*co*-maleic anhydride) (SMA) was functionalized with a C_{12} aliphatic quaternary ammonium moiety which was found to have an affinity for *M. tuberculosis*.[25]

Nanomaterials possess high surface area to volume ratios and often have porous structures, an important consideration in the design of affinity substrates. The specimen volume required for diagnosis could be reduced if the amount of bacteria present in the sample could be concentrated by such a substrate, so as to aid further diagnostic analysis. Nanoparticles and nanofibers are ideally suited to serve as functionalized affinity substrates for the capture of mycobacteria. The use of an external magnetic field to coalesce a group of magnetic nanoparticles coated with a modified polymer, which has an affinity for mycobacteria, could be used to achieve this end. More specifically, a magnetic nanoparticle coated with a mycobacterium-capturing polymer could be used to concentrate the volume of mycobacteria within a sample by inducing an external magnetic field.

2.2.1 Nanoparticles

As intermediates between the molecular and solid states, inorganic nanoparticles combine chemical accessibility in solution with physical properties in the bulk phase.[26] These nanoparticles are therefore ideal for the design and formation of nano-substrates with modifiable physical and chemical properties. Magnetic nanoparticles play a central role in many areas of materials science,

physics and chemistry. The unique properties of nanoscale magnetic materials present vital building blocks to create more complex structures and provide opportunities for applications which could range from chemical sensors to therapeutic devices.[27] Magnetic nanoparticles provide exciting opportunities in biomedical applications, such as tuneable sizes ranging from 2 to 20 nm, manipulation by an external magnetic field and function-specific modification.[28] The ability to disperse and control superparamagnetic nanoparticles through use of an external magnetic field which can be switched on and off, is an important advantage for many present and potential applications.[29] The fact that the nanoparticles are minute and motile enables them to be incorporated into a larger structure to render that structure magnetically responsive.

For biomedical applications, materials with highly saturated magnetization (such as transition metals of Fe, Co and Ni as well as metal oxides) are commonly considered.[30] Pure metals possess the highest saturation magnetization, but are extremely toxic and sensitive to oxidation.[31] Disparately, iron oxides are less oxidation-prone and therefore confer a more stable magnetic response.[32] Iron oxide nanoparticles have inherent properties caused by their multivalent oxidation states, abundant polymorphism and mutual polymorphous changes within the nanophase.[33] Depending on the oxidation state (Fe^{2+} or Fe^{3+}), iron oxides exhibit discrete crystal structures, all of which belong to the spinel group ($MgAl_2O_4$). The crystalline polymorphs of magnetite (Fe_3O_4) and maghemite (γ-Fe_2O_3) have been extensively used as magnetic materials and are suitable for many biomedical applications due to their non-toxic, biocompatible and chemically stable nature,[34] unlike that of pure metals.

Magnetite presents the most fascinating properties among all polymorphs of this spinel group due to its unique magnetic structure which arises as a result of the presence of iron cations in two valence states in the crystal structure.[35] Additionally, magnetite may be straightforwardly synthesized and is abundantly found in nature.[33,36] For these reasons, only magnetite and related materials were studied.

2.3 Magnetite

Magnetite is a ferrimagnetic mineral, with the chemical formula of Fe_3O_4. It is the only polymorph of iron oxide that exhibits strong magnetism, whereas others, such as ilmenite ($FrTiO_3$) and hematite (Fe_2O_3), have weak magnetic properties. Most natural magnetite occurs in miniscule grains in nearly all crystalline rocks as well as many sedimentary rocks. A chunk of crystallized magnetite is called lodestone, which was the earliest form of a sailor's compass.[38,39]

Many migratory animals and some microbes possess magnetic nanoparticles within them that are utilized as natural biomagnetic compasses. Salmon, for example, have a series of magnetic nanoparticles in the nasal capsules of their forehead, which are believed to respond to the geomagnetic field of the earth to help them reach home after journeys that can last tens of thousands of kilometres.[39] These crystals are believed to be involved in magnetoreception, the skill of being able to sense the polarity or the inclination of the earth's magnetic field for navigation.[40]

2.3.1 Synthesis of Magnetite

Numerous chemical methods can be used to synthesize magnetic nanoparticles, such as micro-emulsions,[41] sol-gel synthesis,[42] sonochemical reactions,[43] hydrothermal reactions,[44] hydrolysis and thermolysis of precursors,[45] flow injection synthesis[46] and electrospray synthesis.[47] The most commonly used method for the production of magnetite nanoparticles is the chemical co-precipitation technique of iron salts.[48] This chemical method is able to produce a reasonable amount of product (milligrams to grams), with nanoparticles being essentially monodisperse and chemically uniform.[49] These advantages are primarily as a result of the ability to control the reaction conditions, such as pH, temperature and atmosphere, which influence the three dimensional properties of magnetic nanoparticles.

2.3.2 Structure of Magnetite

Figure 2.2 Group of rhombododecahedral magnetite crystals with octahedral pyrite (left) and black octahedral crystals of magnetite on a matrix (right).

The crystals of magnetite are frequently well-shaped octahedrons, and less frequently dodecahedrons. Magnetite is reported to be a cubic (Fd-3m) inverse spinel structure with oxygen forming a face-centred cubic (FCC) close-packed arrangement and Fe cations occupying the interstitial tetrahedral and octahedral sites.[50]

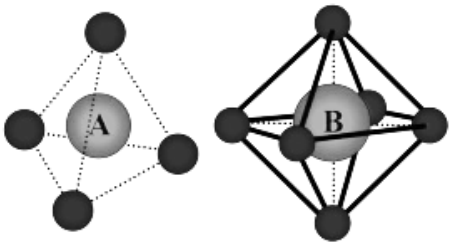

Figure 2.3 A tetrahedral site (A) and an octahedral site (B).

As depicted in Figure 2.3, a tetrahedral atom occupies the centre of a tetrahedron formed by four other lattice atoms (three in-plane atoms and the fourth atom at the symmetrical position on top). An octahedral site for an interstitial atom is the space of the interstices, between six regular atoms to form an octahedron. Four regular atoms are positioned in a plane, and the other two atoms are in a symmetrical position just below or just above.[51]

In magnetite, theoretically, the unit cell is made up of eight cubic units with a lattice d-spacing of 8.396 Å. It contains 56 atoms, including 32 oxygen atoms, 16 Fe^{3+} and 8 Fe^{2+}, and may be denoted as $(Fe^{3+})^{tetr}_8\,[Fe^{3+}Fe^{2+}]^{oct}_8\,O_{32}$. Oxygen anions form a close-packed FCC lattice, as observed in Figure 2.4. There are 64 tetrahedral (A) and 32 octahedral (B) sites in the unit cell. The Fe^{2+} cations occupy a quarter of the octahedral interstitial sites (8 Fe^{2+} and Fe^{3+}) evenly, a quarter of the octahedral sites (i.e. 8 Fe^{3+}) and an eighth of the tetrahedral sites (8 Fe^{3+}).[51,52]

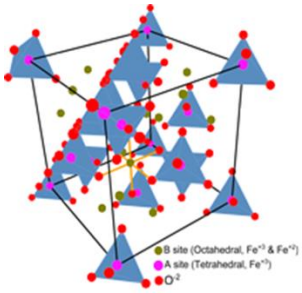

Figure 2.4 Magnetite (Fe_3O_4) crystal structure.

2.3.3 Magnetization

Magnetization is defined as the magnetic dipole moment per unit of volume of material.[53] The magnetic properties of magnetite nanoparticles arise due to electrons in motion. Electrons spinning and revolving in orbits around atomic nuclei generate magnetic dipoles which can either align in opposite directions, causing cancellation, or in the same direction as the applied magnetic field, causing bulk magnetism.[54]

There are several forms of magnetism characteristic to iron oxide nanoparticles that can arise depending on how the magnetic dipoles interact with one another. Any atom or ion of such a material which has one or more unpaired electrons is said to be paramagnetic, and causes the material to be attracted to an externally applied magnetic field.[55] The opposite case holds for diamagnetic materials. In instances where paramagnetic atoms or ions are nearby to one another, and each one is significantly influenced by the orientation of the magnetic dipoles of its neighbours, more complicated forms of magnetism can arise. These include: ferrimagnetism, ferromagnetism and antiferromagnetism. The spontaneous magnetization of a ferromagnet is as a result of the alignment of the magnetic moments of individual atoms.[56] In an antiferromagnet, the atomic moments form two equivalent, but oppositely oriented magnetic sublattices.[53] Four different magnetism classifications are depicted in Figure 2.5.[57]

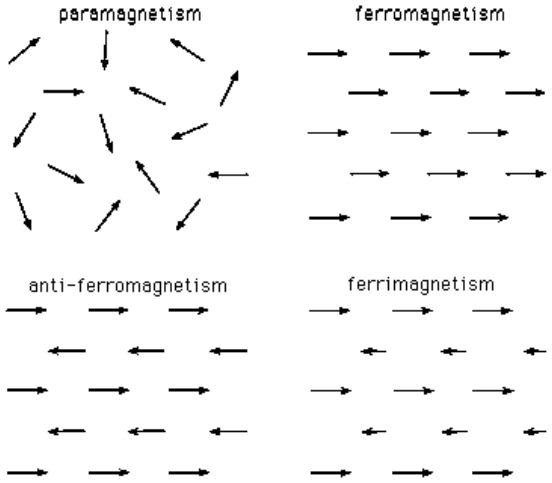

Figure 2.5 The different types of magnetism are classified based on their magnetic behaviour of materials in response to magnetic fields at different temperatures.

2.3.4 Magnetic Properties of Magnetite

The ferrimagnetic order of magnetite arises from a ferromagnetic coupling between iron in tetrahedral sites and ferromagnetic coupling between iron in octahedral sites, while the crossed tetrahedral and octahedral site interaction is antiferromagnetic.[58] Different to other ferrites, magnetite is a fairly good conductor at room temperature. The conductivity is related to its mixed valency, which gives rise to ferromagnetic exchange interactions. Oxides containing a single valency, Fe^{2+} or Fe^{3+}, are magnetic insulators.[59]

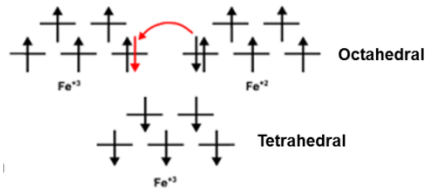

Figure 2.6 Schematic depiction of the splitting of 5d orbitals in octahedral and tetrahedral coordination.

As observed in Figure 2.6, the 5d orbitals are split into two subsets due to the influence of oxide ligands, implying that all of the Fe^{3+} and Fe^{2+} ions have 5 and 4 unpaired electrons, respectively. As can be seen, in the octahedral coordination, Fe^{3+} and Fe^{2+} ions are coupled ferromagnetically through a so called double exchange mechanism. The electron's spin, which is directed in the opposite direction of the others (red), can be exchanged between two octahedral coordinations. Conversely, the Fe^{3+} ions in tetrahedral and octahedral sites are coupled antiferromagnetically via the oxygen atom, implying that the Fe^{3+} spins cancel and thus only unpaired spins of Fe^{2+} in octahedral coordination contribute towards the magnetization. This magnetic moment configuration accounts for the ferrimagnetism observed in magnetite.[60,61]

2.3.5 Nanoscale Magnetism Effects

Many new phenomena have been observed in magnetic nanoparticles that differ from their bulk phase equivalents. In the case of magnetic nanoparticles, the nanoparticle dimension is comparable to that of the magnetic domain. Principal magnetic properties are no longer permanent material characteristics and are therefore disposed to variations in the size, shape and composition of the magnetic nanoparticles. Superparamagnetism is a size dependent phenomenon, and as a result, scaling relationships can be used to tune magnetism from the single domain ferromagnetic regime to the superparamagnetic regime. Surface effects and finite size effects determine the nature of magnetic nanoparticles.[62] The two most studied finite-size effects in nanoparticles are the single domain limit and the superparamagnetic limit.[63]

In large magnetic particles, a multi-domain structure exists where areas of uniform magnetization are divided by domain walls. The creation of the domain walls is a process governed by the equilibrium between the magnetostatic energy and the domain-wall energy. If the sample size is reduced, there is a critical volume below which it requires more energy to create a domain wall than to support the existing external magnetostatic energy of the single-domain state, reached when the magnetostatic energy is equivalent to the domain wall energy. This critical diameter usually lies within the range of a few tens of nanometres and depends upon the material. The

critical diameter is also influenced by the magnetic anisotropic energy, responsible for maintaining the magnetization oriented in certain directions.[64]

As depicted in Figure 2.7, a single domain particle is uniformly magnetized when all of the spins are aligned in the same direction. The exchange-coupled spins rotate in unison, flipping the entire particle's magnetic moment coherently. The switching field or coercivity (H_c) is a maximum for particles at the greatest monodomain size.[65] The magnetization will be switched by spin rotation since there are no domain walls to move, which explains why a smaller particle will have a higher coercivity.[66] Another reason for this observation is due to shape anisotrophy. Surface effects influence the magnetic properties of magnetic nanoparticles. Owing to the large ratio of surface atoms to bulk atoms, the surface spins contribute substantially to the magnetization, essentially causing a local breaking of the symmetry.[67]

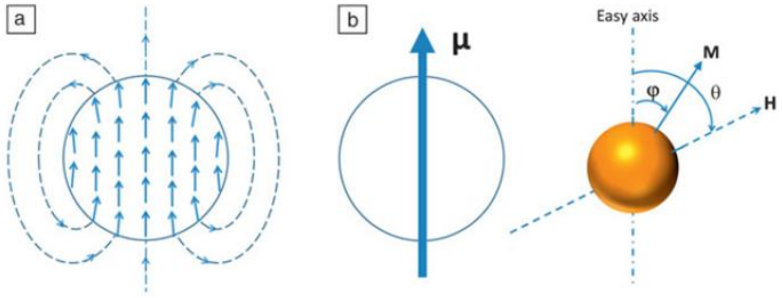

Figure 2.7 (a) A spherical particle has a net magnetic moment resulting from the internal alignment of atomic spins. (b) The equilibrium direction of the single particle magnetization depends on the external magnetic field H and its magnetocrystalline anisotropy easy axis. Where M is the magnetization, φ is the angle between the easy axis and the magnetization and θ is the angle between the easy axis and the applied field.

Bulk materials have magnetic anisotropic energies that are much larger than the thermal energy. Nanoparticles have magnetic anisotropic energies that are comparable to the thermal energy, making the thermal energy adequate to readily reverse the magnetic spin direction, though inadequate to overcome the spin-spin exchange coupling energy.[68]

For iron oxide nanoparticles, the critical diameter below which the particles lose their bulk magnetism and are said to become superparamagnetic is approximately 20 nm.[69] With decreasing particle size, the thermal energy overcomes the energy barrier of the nanoparticles. Magnetization is easily flipped and thermal fluctuations randomly switch the magnetization direction between parallel and antiparallel orientations. Magnetic fluctuations such as these lead to a net magnetization of zero. When this occurs, the system behaves like a paramagnet and instead of atomic magnetic moments, there is now a very large (super) moment inside each particle. A superparamagnet is therefore defined as an assembly of giant magnetic moments which are not interacting, and which can fluctuate when the thermal energy is larger than the anisotropy

energy.[70] The transition temperature from ferromagnetism to superparamagnetism is referred to as the blocking temperature.[68]

Superparamagnetic particles exhibit no remanent magnetization or coercivity, that is, there is no hysteresis in the magnetization curve.[71] The effects of temperature and measurement time on the magnetization curves are depicted in Figure 2.8.

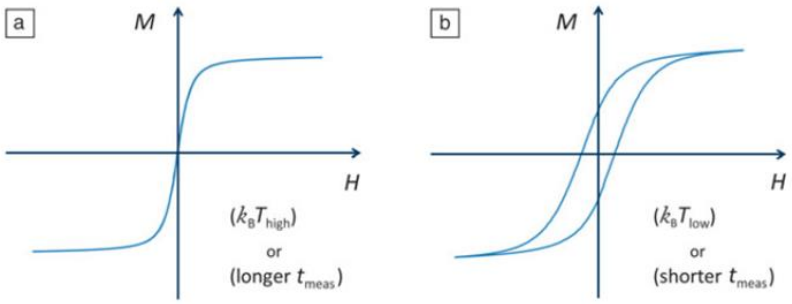

Figure 2.8 Magnetization curves. (a) Superparamagnetic particles with zero coercivity. This occurs when the thermal energy is high relative to the energy barrier or when the measurement time (t_{meas}) is long so that the sample reaches thermal equilibrium. (b) If equilibrium is not reached within the measurement time, then hysteresis will be observed (Note: k_B is Blotzman's constant, T_{high} is a higher temperature, and T_{low} is a lower temperature).

Here an external magnetic field (H) is applied, and the material magnetization (M), parallel to the applied field, is measured. The saturation magnetization (M_s) occurs when the spins of the ferromagnet are fully aligned. The magnetization present after saturation and the subsequent removal of the field is referred to as the remanent magnetization (M_r) at H=0.[72] The reversal of the field in the direction opposite to the remanent magnetization causes the magnetic moments to randomize again. The field required to bring the net magnetization back to zero is called the coercivity (H_c). An ensemble of particles is said to be superparamagnetic if they were originally aligned but have random directions at the time of measurement, due to thermal fluctuations of thermal energy.[27]

These superparamagnetic magnetite nanoparticles will at times be referred to as SPMNs. With SPMNs, it is possible to target a specific substrate or location through use of external magnet fields. SPMNs exhibit superparamagnetism, high-field irreversibility, high saturation fields and extra anisotropy contributions or shifted loops after field cooling.[73] Because of these properties, the nanoparticles no longer exhibit magnetic interaction after the external magnetic field is removed and may accordingly be manipulated.

2.3.6 Aggregation

In the preparation and storage of nanoparticles in colloidal form, the stability of the colloid is very important. In the absence of any surface coating, magnetic iron oxide nanoparticles have hydrophobic surfaces with a large surface area to volume ratio.[74] The singular nanoparticles of magnetite therefore possess high surface energies and have the tendency to interact with one another. The stability of SPMNs in suspension is controlled by three principle forces: (a) hydrophobic-hydrophilic (b) magnetic and (c) van der Waals. When attractive force interactions dominate, Brownian motion leads to irreversible aggregation of the nanoparticles.[37] SPMNs tend to aggregate to micron size aggregates in suspension due to hydrophobic interactions between the sub nanometre scale particles, which occur in order to minimize the total surface energy of the system. Micron size clusters further aggregate due to dipole-dipole interactions and become magnetized by neighbouring clusters. In the presence of an external magnetic field, further magnetization of these clusters can occur, increasing aggregation.[75] These clusters then exhibit strong magnetic dipole-dipole attractions between them and show ferromagnetic behaviour. Additionally, factors such as magnetic field, pH and ionic strength can influence the morphology and size of the aggregates.[46,77]

2.3.7 Coating Superparamagnetic Magnetite Nanoparticles (SPMNs)

Since magnetic nanoparticles are attracted magnetically, in addition to the typical flocculation due to van der Waals forces, surface modification is often vital in the synthesis of magnetic nanoparticles. Significant strides in the synthesis of magnetic nanoparticles have been achieved, but maintaining the stability of these particles over extended periods of time without aggregation or precipitation, is still a pressing issue.

A surfactant or polymer may be used to passivate the surface of the nanoparticles during or after synthesis to avoid aggregation.[46] If magnetite nanoparticles are coated with a suitable polymer, the hybrid magnetic nanoparticles will gain the advantages of good dispersion in aqueous or organic media, high stability against oxidation and available surface functional groups which can be used for further functionalization, as depicted in Figure 2.9.[77]

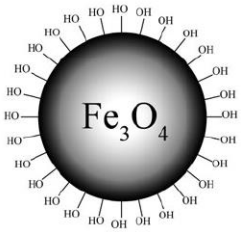

Figure 2.9 Iron Oxide (Fe_3O_4) core.

A polymer can be used to coat magnetic nanoparticles to form a single or double layer, generating steric repulsive forces to balance the magnetic and van der Waals attractive forces acting on the nanoparticles.[78] Two approaches are available for coating nanoparticles: ligand exchange and ligand addition. A ligand exchange mechanism involves the substitution of one or more ligands in a complex ion with one or more different ligands. With the ligand addition mechanism, polymers are physically adsorbed onto the surfaces of the nanoparticles due to electrostatic and hydrophobic interactions as well as hydrogen bonding.[79]

Polymers with functional groups such as hydroxyl, amine and carboxyl groups close to the boundary of the nanoparticles readily adsorb onto their surfaces. Tailoring the surfaces of the nanoparticles with polymers and other materials improves stability, surface charge, functionality and targeting capability. In addition to electrostatic interaction, hydrophobic interactions, entropic effects, hydrogen bonding and cation bridging are a few essential mechanisms in the adsorption of stabilizing agents onto the surface of iron oxides. The formation of covalent bonds may also be explored as an alternative.[79]

The polymeric coating not only protects the nanoparticles from forming aggregates, but can also be tailored to serve a specific end application, dependent on the polymer of choice and its functionalization. Polymers containing moieties such as amino groups, carboxylic acids, phosphates and sulphates can bind to the surface of magnetite.[81,82] Once the ligand exchange is complete, the nanoparticles become stable in water and hence suitable for biological applications.[83] Among the coating polymers studied to date, chitosan has attracted substantial attention.

2.4 Chitosan

Chitosan (CS) is a polycationic, hydrophilic, binary heteropolymer consisting of β-(1-4)-linked D-glucosamine and *N*-acetyl-D-glucosamine monomers, obtained by the deacetylation of chitin.[83] Chitin is the second most abundant natural biopolymer in the world after cellulose and is synthesized by a variety of living organisms.[85,86] It occurs in nature as ordered crystalline microfibrils which form the structural components in the exoskeleton of arthropods (such as insects, arachnids, and crustaceans) and in the cell walls of fungi and yeast.[87,88] A major function of chitin is therefore in the strengthening and reinforcement of organisms. The structures of chitosan and chitin polymers are presented in Figure 2.10.

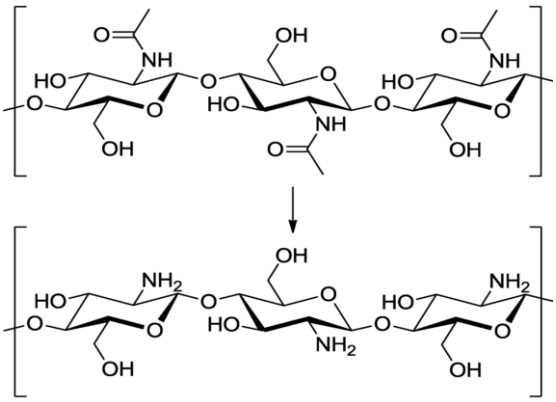

Figure 2.10 Chemical structure of chitin (above) and chitosan (below).

Chitosan is a nontoxic, biodegradable, and biocompatible polymer.[89] It exhibits a positive charge in an acidic environment and has good mucoadhesive and antibacterial properties,[90] bioadherence and cell affinity.[91] As a result, it has been the focus of copious research directed towards biomedical applications.[92] The majority of naturally occurring polysaccharides such as pectin, dextrin, agar, agarose, carragenas and cellulose are acidic in nature, whilst chitosan is a highly basic polysaccharide. Chitosan exhibits special properties such as viscosity, solubility in various media, mucoadhesivity, polyoxysalt formation, polyelectrolyte behaviour, ability to form films, metal chelations, optical and structural characteristics. It also has the potential to bind antagonistically with microbial and mammalian cells.[93]

Unfortunately, in spite of such favourable properties, a major limitation exists in that chitosan is insoluble in water and is only soluble in acidic aqueous media at pH $\leq$ 6.5, required to ensure the protonation of the primary amine group.[94] At higher pH values the amino groups of chitosan macromolecules become deprotonated and at neutral pH values, chitosan loses its charge and precipitates from solution. This interferes with the biomedical applications of the polymer, especially at the physiological pH value of 7.4 where chitosan is insoluble and thus ineffective.

To overcome this obstacle and impart new characteristics to an already advantageous polymer, chitosan's hydroxyl and amino functionalities can be chemically modified. One of the strategies to increase both the solubility and positive charge density of chitosan macromolecules is based on the introduction of quaternary ammonium groups. A schematic illustration of the increased solubility from chitin to substituted chitosan is presented in Figure 2.11. Furthermore, the term "quaternization" of chitosan will be used in spite of it referring to a reaction between an amine and alkyl halide resulting in tetralkylammonium salt formation. The quaternized structure of chitosan inhibits intermolecular bonding between the amine and hydroxyl groups, thus allowing hydrogen bonding with water molecules.[95-102]

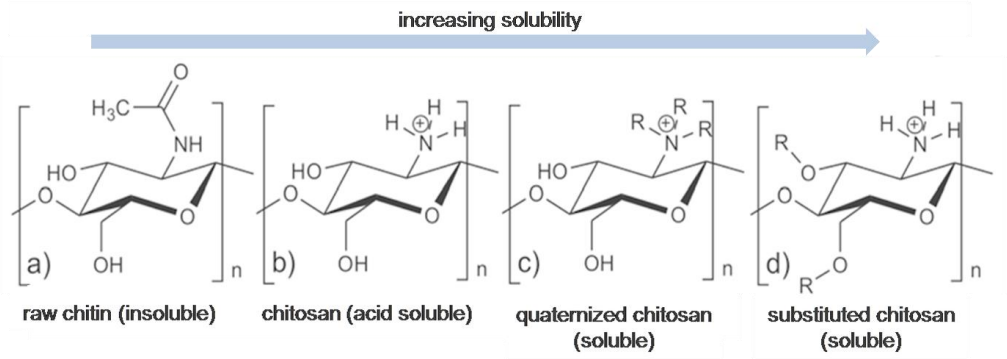

Figure 2.11 Schematic representation of chitin and chitosan derivatives. Specific chemical modification of the structure leads to the enhanced solubility of the almost insoluble biopolymer chitin (a). Quaternized (c) and substituted (d) derivatives also show better solubility under alkaline conditions compared to chitosan (b).

Various modifications of chitosan, specifically quaternized derivatives, present themselves as promising candidates for biological applications involving their use as affinity substrates for the loading of biological cells, such as mycobacteria, onto their structures. Nanotechnology can be used as a vital aid in achieving this goal. Nanomaterials such as nanoparticles and nanofibers exhibit enhanced properties in the nanoscale, as compared to conventional morphologies in larger scales. Nanoparticles made out of metal can chelate with quaternized chitosan to form a smooth continuous coating on a metal core; and nanofibers can be electrospun from quaternized chitosan using the electrospinning technique.

2.5 Electrospinning

Nanofibers are a class of nanomaterials which have diameters of less than 100 nm.[103] The electrospinning of chitosan and its derivatives into nanofibers has recently become very popular.[104] Electrospinning is a simple, robust and versatile technique used to produce continuous nanofibers with high specific surface areas and high aspect ratios,[105] providing ideal attributes for affinity substrate consideration. A high loading of the organism per unit mass of nanofiber may be obtained, making the immobilization of biological molecules such as microbes highly favourable.[106,107] Electrospinning is classically conducted at room temperature with atmospheric conditions. A typical set-up of the electrospinning apparatus is schematically illustrated in Figure 2.12.

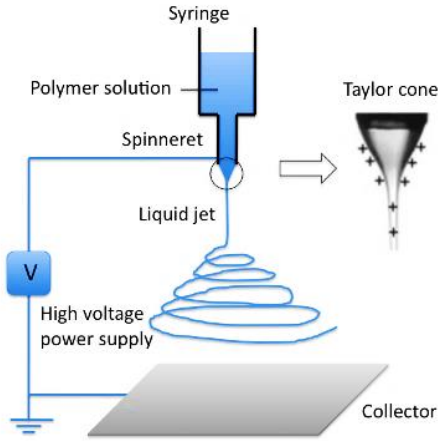

Figure 2.12 Schematic diagram of electrospinning set-up.

A typical electrospinning setup comprises a reservoir of polymer solution with a metallic capillary connected to a high voltage power supply and a metallic collector. Upon increasing the electrostatic field strength up to but not exceeding a critical value, the hemispherical shape of the polymer droplet at the needle tip is destabilized by the accumulated charges on the surface of the droplet.[108] It is then converted to a conical shape commonly known as Taylor's cone. This occurs when a sufficiently high voltage is applied to the polymer solution. At the critical value, a charged polymer jet is ejected from the apex of the cone as a way of relieving the charge built-up on the surface of the pendant drop. The electrical forces thus overcome the surface tension on the droplet and an ultra-fine fiber jet is produced from the tip of the Taylor cone. The ejected charged jet is then carried to the collection screen via the electrostatic force. The Coulombic repulsion force is responsible for the stretching and elongation of the charged jet during its trajectory to the collection screen. This drawing mechanism is limited by the viscosity increase as the charged jet is dried due to solvent evaporation.[109]

To conclude, in this chapter tuberculosis (TB) and the diagnosis thereof have been discussed. The difficulties in diagnosing TB have been highlighted as well as the reasons as to why this is so. A specific requirement for accurate TB diagnosis is that specimen volumes from patients being investigated should be as large as possible in order to obtain the greatest volume of mycobacteria. Nanotechnology and polymer science are rapidly advancing research within the biomedical field in order to address the challenges associated with devastating diseases such as TB.

By using a polymer, which is specifically modified to capture mycobacteria, specimen collection can be enhanced by increasing the yield of *M. tuberculosis* within the specimen, thus improving the likelihood of successfully detecting *M. tuberculosis* and diagnosing TB. Chitosan was identified as a biopolymer with a multitude of favourable biological attributes, ideal for use as an affinity

substrate. This polymer possesses functionalities which can be chemically modified in order to improve the feasibility of mycobacteria-polymer interaction. Nanoparticles and nanofibers are materials having high specific surface areas with tunable properties, thus providing the ideal nano-structures in which to mode chitosan and chitosan derivatives for the most efficient *M. tuberculosis* capture.

2.6 References

1. Dye, C. *The Lancet* **2006**, *9514,* 938-940.
2. Sudre, P.; Ten Dam, G.; Kochi, A. *Bull. World Health Organ.* **1992**, *2,* 149.
3. Kochi, A. *Bull. World Health Organ.* **2001**, *1,* 71-75.
4. Jungblut, P.; Schaible, U.; Mollenkopf, H.; Zimny-Arndt, U.; Raupach, B.; Mattow, J.; Halada, P.; Lamer, S.; Hagens, K.; Kaufmann, S. *Mol. Microbiol.* **1999**, *6,* 1103-1117.
5. Lieberman, A. *Springer Series Chem*. **2012**; .
6. Comstock, G. W.; Livesay, V. T.; Woolpert, S. F. *Am. J. Epidemiol.* **1974**, *2,* 131-138.
7. Sutherland, I. *Adv. Tuberc. Res.* **1976**, 1-63.
8. Armstrong, J. A.; Hart, P. D. *J. Exp. Med.* **1971**, *3 Pt 1,* 713-740.
9. Gray, J. W. *Clin. Biochem.* **2004**, *6,* 450-455.
10. Sreeramareddy, C. T.; Panduru, K. V.; Menten, J.; Van den Ende, J. *BMC Infect. Dis.* **2009**, *9*, 2334.
11. Bancroft, J. D.; Gamble, M. *Theory and practice of histological techniques;* Elsevier, **2008**.
12. Brisson-Noël, A.; Lecossier, D.; Nassif, X.; Gicquel, B.; Lévy-Frébault, V.; Hance, A. *The Lancet.* **1989**, *8671,* 1069-1071.
13. Moussa, O. M.; Eraky, I.; El-Far, M. A.; Osman, H. G.; Ghoneim, M. A. *J. Urol.* **2000**, *2,* 584-588.
14. Trajman, A.; Kaisermann, C.; Luiz, R.; Sperhacke, R.; Rossetti, M.; Féres Saad, M.; Sardella, I.; Spector, N.; Kritski, A. *Scand. J. Clin. Lab. Invest.* **2007**, *8,* 877-884.
15. Ravva, S. V.; Stanker, L. H. *J. Microbiol. Methods* **2005**, *3,* 305-317.
16. Holtz, T. H.; Sternberg, M.; Kammerer, S.; Laserson, K. F.; Riekstina, V.; Zarovska, E.; Skripconoka, V.; Wells, C. D.; Leimane, V. *Ann. Intern. Med.* **2006**, *9,* 650-659.
17. Oberhelman, R. A.; Soto-Castellares, G.; Gilman, R. H.; Caviedes, L.; Castillo, M. E.; Kolevic, L.; Del Pino, T.; Saito, M.; Salazar-Lindo, E.; Negron, E. *The Lancet Infect. Dis.* **2010**, *9,* 612-620.
18. Hale, Y. M.; Pfyffer, G. E.; Salfinger, M. *Clin. Infect. Dis.* **2001**, *6,* 834-846.
19. Gray, J. W. *Clin. Biochem.* **2004**, *6,* 450-455.
20. Warren, J. R.; Bhattacharya, M.; De Almeida, K. N.; Trakas, K.; Peterson, L. R. *Am. J. Respir. Crit. Care Med.* **2000**, *5,* 1559-1562.
21. Silva, G. A. *Surg. Neurol.* **2004**, *3,* 216-220.
22. Gupta, A. K.; Gupta, M. *Biomaterials* **2005**, *18,* 3995-4021.
23. Wagner, V.; Dullaart, A.; Bock, A.; Zweck, A. *Nat. Biotechnol.* **2006**, *10,* 1211-1217.

24. Pandey, R.; Khuller, G. *Tuberculosis* **2005**, *4,* 227-234.

25. Cronje, L. *Surface modification of styrene maleic anhydride nanofibers for efficient capture of Mycobacterium tuberculosis,* PhD Thesis, University of Stellenbosch, South Africa. **2012**.

26. Osterloh, F. E. *J. Am. Chem. Soc.* **2002**, *22,* 6248-6249.

27. Majetich, S. A. *ChemInform* **2008**, *27,*.

28. Gao, J.; Gu, H.; Xu, B. *Acc. Chem. Res.* **2009**, *8,* 1097-1107.

29. Buzea, C.; Pacheco, I. I.; Robbie, K. *Biointerphases* **2007**, *4,* MR17-MR71.

30. Umut, E. *Mod. Surf. Eng. Treatments* **2013**, 185-208.

31. Tran, N.; Webster, T. J. *J. Mater. Chem.* **2010**, *40,* 8760-8767.

32. Huang, S.; Juang, R. *J. Nanopart. Res.* **2011**, *10,* 4411-4430.

33. Woo, K.; Hong, J.; Choi, S.; Lee, H.; Ahn, J.; Kim, C. S.; Lee, S. W. *Chem. Mater.* **2004**, *14,* 2814-2818.

34. Belessi, V.; Zboril, R.; Tucek, J.; Mashlan, M.; Tzitzios, V.; Petridis, D. *Chem. Mater.* **2008**, *10,* 3298-3305.

35. Ranganath, K. V.; Glorius, F. *Catal. Commun.* **2011**, *1,* 13-22.

36. Kirschvink, J. L.; Chang, S. R. *Geology* **1984**, *9,* 559-562.

37. Majewski, P.; Thierry, B. *Crit. Rev. Solid. State* **2007**, *3-4,* 203-215.

38. Majewski, P.; Thierry, B. *Recent Pat. Mat. Sci.* **2008**, *2,* 116-127.

39. Dankers, P. *Geophys. J. Int.* **1981**, *2,* 447-461.

40. Walker, M. M.; Diebel, C. E.; Green, C. R. *J. Appl. Phys.* **2000**, *9,* 4653-4658.

41. Chin, A. B.; Yaacob, I. I. *J. Mater. Process. Technol..* **2007**, *1,* 235-237.

42. Olariu, C. I.; Yiu, H. H.; Bouffier, L. *Springer* **2013**, 85-133.

43. Gedanken, A. *Ultrason. Sonochem.* **2004**, *2,* 47-55.

44. Wang, Z.; Xiao, P.; He, N. *Carbon* **2006**, *15,* 3277-3284.

45. Kimata, M.; Nakagawa, D.; Hasegawa, M. *Powder Technol.* **2003**, *2,* 112-118.

46. Salazar-Alvarez, G.; Muhammed, M.; Zagorodni, A. A. *Chem. Eng. Sci.* **2006**, *14,* 4625-4633.

47. Basak, S.; Chen, D.; Biswas, P. *Chem. Eng. Sci.* **2007**, *4,* 1263-1268.

48. Laurent, S.; Forge, D.; Port, M.; Roch, A.; Robic, C.; Vander Elst, L.; Muller, R. N. *Chem. Rev.* **2008**, *6,* 2064-2110.

49. Majetich, S.; Scott, J.; Kirkpatrick, E.; Chowdary, K.; Gallagher, K.; McHenry, M. *Nan. Sci. Tech.* **1997**, *1,* 291-300.

50. Mahmoudi, M.; Sant, S.; Wang, B.; Laurent, S.; Sen, T. *Adv. Drug Deliv. Rev.* **2011**, *1,* 24-46.

51. Von Hippel, A. R. *Elec. Soc. S.* **1954**, *2*.

52. Bragg, W. *Nature* **1915**, 561.

53. Coey, J. *J. Magn. Magn. Mater.* **2010**, *9,* 1045-1046.

54. Perry, J. L.; Herlihy, K. P.; Napier, M. E.; DeSimone, J. M. *Acc. Chem. Res.* **2011**, *10,* 990-998.

55. Pauling, L. *J. Am. Chem. Soc.* **1931**, *9,* 3225-3237.

56. Caneschi, A.; Gatteschi, D.; Sessoli, R.; Rey, P. *Acc. Chem. Res.* **1989**, *11,* 392-398.

57. Zhang, Z.; Satpathy, S. *Phys. Rev. B.* **1991**, *24,* 13319.

58. de la Figuera, J.; Vergara, L.; N'Diaye, A. T.; Quesada, A.; Schmid, A. K. *Ultramicroscopy* **2013**, 77-81.

59. Benitez, M.; Mishra, D.; Szary, P.; Confalonieri, G. B.; Feyen, M.; Lu, A.; Agudo, L.; Eggeler, G.; Petracic, O.; Zabel, H. *J Phys-Condens. Mat.* **2011**, *12,* 126003.

60. Patil, K. C.; Hegde, M.; Rattan, T.; Aruna, S. *Nature* **2008**.

61. Belov, K. P. *Physics-Uspekhi* **1993**, *5,* 380.

62. Jun, Y.; Seo, J.; Cheon, J. *Acc. Chem. Res.* **2008**, *2,* 179-189.

63. Skumryev, V.; Stoyanov, S.; Zhang, Y.; Hadjipanayis, G.; Givord, D.; Nogues, J. *Nature* **2003**, *6942,* 850-853.

64. Lu, A.; Salabas, E. e.; Schüth, F. *Angew. Chem. Int. Edit.* **2007**, *8,* 1222-1244.

65. Pankhurst, Q. A.; Connolly, J.; Jones, S.; Dobson, J. *J. Phys. D* **2003**, *13,* R167.

66. Iwaki, T.; Kakihara, Y.; Toda, T.; Abdullah, M.; Okuyama, K. *J. Appl. Phys.* **2003**, 6807-6811.

67. Issa, B.; Obaidat, I. M.; Albiss, B. A.; Haik, Y. *Int. J. Mol. Sci.* **2013**, *11,* 21266-21305.

68. Jun, Y.; Seo, J.; Cheon, J. *Acc. Chem. Res.* **2008**, *2,* 179-189.

69. Berry, C. C.; Curtis, A. S. *J. Phys. D* **2003**, *13,* R198.

70. Dormann, J.; Cherkaoui, R.; Spinu, L.; Nogues, M.; Lucari, F.; D'Orazio, F.; Fiorani, D.; Garcia, A.; Tronc, E.; Jolivet, J. *J. Magn. Magn. Mater.* **1998**, *2,* L139-L144.

71. Sun, S.; Zeng, H. *J. Am. Chem. Soc.* **2002**, *28,* 8204-8205.

72. Cullity, B. D.; Graham, C. D. *Introduction to magnetic materials;* John Wiley & Sons, **2011**.

73. Kodama, R. *J. Magn. Magn. Mater.* **1999**, *1,* 359-372.

74. Wu, W.; He, Q.; Jiang, C. *ChemInform* **2009**, *24,* i.

75. Hamley, I. *Angew. Chem. Int. Edit.* **2003**, *15,* 1692-1712.

76. Lakay, E. M. *Superparamagnetic iron-oxide based nanoparticles for the separation and recovery of precious metals from solution,* MSc Thesis, University of Stellenbosch, South Africa. **2009**.

77. Zhou, L.; Yuan, J.; Yuan, W.; Zhou, M.; Wu, S.; Li, Z.; Xing, X.; Shen, D. *Mater. Lett.* **2009**, *18,* 1567-1570.

78. Mornet, S.; Vasseur, S.; Grasset, F.; Duguet, E. *J. Mater. Chem.* **2004**, *14,* 2161-2175.

79. Muthiah, M.; Park, I.; Cho, C. *Biotechnol. Adv.* **2013**, *8,* 1224-1236.

80. Dias, A.; Hussain, A.; Marcos, A.; Roque, A. *Biotechnol. Adv.* **2011**, *1,* 142-155.

81. Cornell, R. M.; Schwertmann, U. *The iron oxides: structure, properties, reactions, occurrences and uses;* John Wiley & Sons, **2006**.

82. Jingmiao, F.; Zhiqiang Q.; Ruoyu, H.; Dongguang, L. H. W. *Chem. Mater.* **2008**, *8*.

83. López-Cruz, A.; Barrera, C.; Calero-DdelC, V. L.; Rinaldi, C. *J. Mater. Chem.* **2009**, *37,* 6870-6876.82.

84. Ilium, L. *Pharm. Res.* **1998**, *9,* 1326-1331.83.

85. Selmer-Olsen, E.; Ratnaweera, H.; Pehrson, R. *Water Sci. Technol.* **1996**, *11,* 33-40.84.

86. Rinaudo, M. *Prog. Polym. Sci.* **2006**, *7,* 603-63.

87. Jayakumar, R.; Prabaharan, M.; Nair, S.; Tamura, H. *Biotechnol. Adv.* **2010**, *1,* 142-150.

88. Cohen, E. *Pest Manag. Sci.* **2001***, 10,* 946-950.

89. Baldrick, P. *Reg. Toxicol. Pharm.* **2010***, 3,* 290-299.

90. Dodane, V.; Vilivalam, V. D. *Pharm. Sci. Technol. Today* **1998***, 6,* 246-253.

91. Kumar, S.; Dutta, J.; Dutta, P. *Int. J. Biol. Macromol.* **2009***, 4,* 330-337.

92. Dash, M.; Chiellini, F.; Ottenbrite, R. M.; Chiellini, E. *Prog. Polym. Sci.* **2011***, 8,* 981-1014.

93. Shukla, S. K.; Mishra, A. K.; Arotiba, O. A.; Mamba, B. B. *Int. J. Biol. Macromol.* **2013**, 46-58.

94. Riva, R.; Ragelle, H.; des Rieux, A.; Duhem, N.; Jérôme, C.; Préat, V. *Springer* **2011**, 19-44.

95. Domard, A.; Gey, C.; Rinaudo, M.; Terrassin, C. *Int. J. Biol. Macromol.* **1987***, 4,* 233-237.

96. Muzzarelli, R.; Tanfani, F. *Pure Appl. Chem.* **1982***, 11,* 2141-2150.

97. Le Dung, P.; Milas, M.; Rinaudo, M.; Desbrières, J. *Carbohydr. Polym.* **1994***, 3,* 209-214.

98. Snyman, D.; Hamman, J.; Kotze, J.; Rollings, J.; Kotze, A. *Carbohydr. Polym.* **2002***, 2,* 145-150.

99. Holappa, J.; Hjálmarsdóttir, M.; Másson, M.; Rúnarsson, Ö.; Asplund, T.; Soininen, P.; Nevalainen, T.; Järvinen, T. *Carbohydr. Polym.* **2006***, 1,* 114-118.

100. Ignatova, M.; Starbova, K.; Markova, N.; Manolova, N.; Rashkov, I. *Carbohydr. Res.* **2006***, 12,* 2098-2107.

101. Stepnova, E. A.; Tikhonov, V. E.; Babushkina, T. A.; Klimova, T. P.; Vorontsov, E. V.; Babak, V. G.; Lopatin, S. A.; Yamskov, I. A. *Eur. Polym. J.* **2007***, 6,* 2414-2421.

102. Belessi, V.; Zboril, R.; Tucek, J.; Mashlan, M.; Tzitzios, V.; Petridis, D. *Chem. Mater.* **2008***, 10,* 3298-3305.

103. Zhang, Y.; Lim, C. T.; Ramakrishna, S.; Huang, Z. *J. Mater. Sci. Mater. Med.* **2005***, 10,* 933-946.

104. Thavasi, V.; Singh, G.; Ramakrishna, S. *Energy Environ. Sci.* **2008***, 2,* 205-221.

105. Chronakis, I. S. *J. Mater. Process. Technol.* **2005***, 2,* 283-293.

106. Griffith, D. E.; Kerr, C. M. *J. Perianest. Nurs.* **1996***, 4,* 240-245.

107. Li, F.; Song, Y.; Zhao, Y. INTECH **2010**.

108. Haider, S.; Park, S. *J. Membr. Sci.* **2009***, 1,* 90-96.

109. Neamnark, A.; Rujiravanit, R.; Supaphol, P. *Carbohydr. Polym.* **2006***, 3,* 298-305.

Chapter Three

Precursor Polymers

3.1 Introduction

Chitosan is a nontoxic, biodegradable and biocompatible polymer. It exhibits a positive charge in an acidic environment and has good mucoadhesive and anti-bacterial properties, bioadherence and cellular affinity. As a result, it has been the focus of widespread research directed towards biomedical applications. Chitosan is, however, only soluble in few dilute acidic solutions, which drastically limits its potential applications.[3-5] Chitosan is a multinucleophilic polymer, so an elegant way to improve or to impart new properties to chitosan is through chemical modification. The unique structural features of chitosan pertain to the presence of primary amine moieties of the D-glucosamine residues and the two hydroxyl functionalities, which are attractive reactive sites for possible chemical modification. The presence of these chemical groups allows for specific chemical reactions and confers important functional properties to chitosan, which could be further exploited for various applications. The initial sites where substitution occurs are the more nucleophilic amino groups.[6] The amino functionality provides the potential for chemical reactions such as acetylation, alkylation, quaternization, grafting and metal chelation.[7,8]

To synthesize amphiphilic chitosan derivatives, hydrophobic functionalities can be grafted onto the chitosan polymer backbone. The hydrophobicity of chitosan can be considerably increased by the introduction of hydrophobic side chains. Additionally, hydrophilic side chains can be introduced to alter its hydrophilic/hydrophobic balance. The quaternary derivatives of *N*-alkyl chitosan have been proven to be effective as antimicrobial agents, apart from finding application in the field of tissue engineering, DNA delivery, drug delivery, and membrane coating.[9] Rabea *et al.* found that the antimicrobial activity of quaternized chitosan derivatives increased with increasing content of the quaternary ammonium moiety and with increasing chain length of the alkyl substituent.[10] This was as a result of the contribution of the increased hydrophobic properties of the derivatives. These results confirmed that the hydrophobicity and cationic charge of the introduced substituent strongly affect the antibacterial activity and thus cellular affinity of quaternary chitosan derivatives. Cellular adhesion is regulated by surface wettability, an important physicochemical property of biomaterials.

Other contributing surface properties include roughness, surface charge, and more notably, chemical functionalities. With respect to surface wettability of polymeric materials, cells effectively adhere onto polymer surfaces presenting moderate wettability with water contact angles of 40 - 70°, owing to wettable surfaces, moderately hydrophilic in nature.[11-14] The water contact angles associated with the different types of surface effects are schematically illustrated in Figure 3.1.

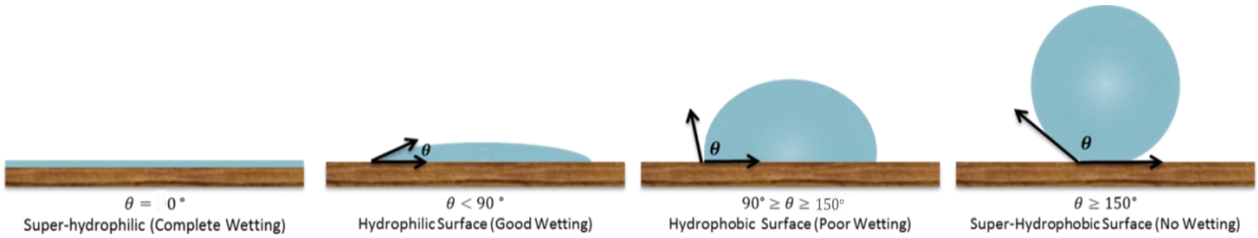

Figure 3.1 On a hydrophilic surface a water drop spreads out to increase the contact surface. On a hydrophobic surface a water drop contracts to minimize the contact surface.

3.2 Results and Discussion

The aim of this section in the study was to synthesize and characterize the quaternized derivatives of chitosan, namely *N*-trimethylammonium chitosan chloride (TMC) and *N*-(2-hydroxy)propyl-3-trimethylammonium chitosan chloride (HTCC) as well as the quaternized *N*-alkylated chitosan derivatives of *N*-propyl-3-*N',N'*-dimethyl-*N'*-octylammonium chitosan chloride (CS-qC$_8$), *N*-propyl-3-*N',N'*-dimethyl-*N'*-decylammonium chitosan chloride (CS-qC$_{10}$) and *N*-propyl-3-*N',N'*-dimethyl-*N'*-dodecylammonium chitosan chloride (CS-qC$_{12}$). These derivatives of chitosan were synthesized based on possible interactions with the *Mycobacterium tuberculosis* cell wall.

3.2.1 Chitosan

Chitosan is a semi-synthetic, linear and random copolymer composed of a variable number of β-(1-4) linked units of 2-acetamide-2-deoxy-β-d-glucopyranose (GlcNAc) and 2-amino-2-deoxy-β-d-glycopyranose (GlcN).[15] The two monomers differ with respect to the C2-substituent in the saccharide ring, which is either an amino or acetamide group, as illustrated in Figure 3.2.

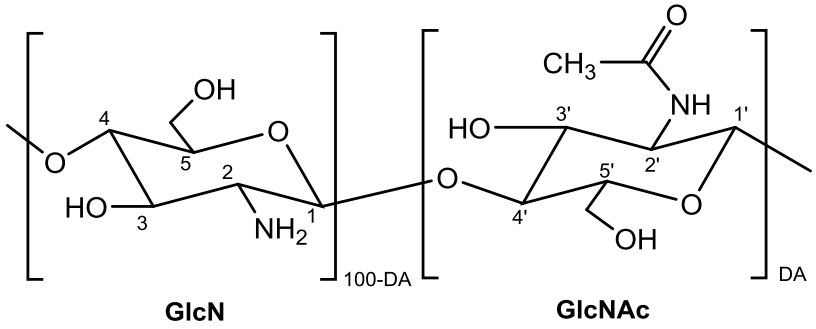

Figure 3.2 Schematic representation of a disaccharide formed by 2-amino-2-deoxy-β-d-glycopyranose (GlcN) bound to 2-acetamide-2-deoxy-β-d-glucopyranose (GlcNAc). GlcN and GlcNAc are the two units which form chitosan.

Chitosan is obtained by the alkaline deacetylation of chitin. The deacetylation reaction, however, seldom proceeds to completion in a normal heterogeneous reaction, leading to a random distribution of GlcNAc and GlcN residues in the chitosan polymer.[16] The degree of *N*-acetylation (DA) of a polymer is a measure of the average number of GlcNAc per 100 chitosan monomers in percentile units. The ratio of the GlcNAc to GlcN structural units determine whether chitin has been converted to chitosan. In chitin, the acetylated units prevail (DA ≥ 90%), whereas chitosan is the fully or partially *N*-deacetylated derivative with a DA of less than 30%,[6] relating to a degree of *N*-deacetylation (DDA) ≥ 70%.

The DA governs important physical and chemical properties such as solubility and conformation; factors which are critical for chitosan's use in various technological applications. Chitosan is not cationic or water soluble unless the pH is below 6.5. It is neutralized at these low pH values to the water-soluble chitosonium salt.[17] In acidic pH conditions, the amino groups on the C-2 of the GlcN unit can undergo protonation, thus making chitosan soluble in water. The solubility of chitosan therefore depends upon the distribution of free amino and *N*-acetyl groups.[18]

a) ATR-FTIR

Chitosan used in this study was obtained as a semi-synthetic polymer, derived from chitin found in crab shells. In this regard, varying degrees of acetylation and molecular weight can be achieved and it is therefore necessary to characterize the polymer before further chemical modification. The representative IR spectrum of pristine chitosan is shown in Figure 3.3 and Table 3.1 summarizes and describes the characteristic absorption bands of pristine chitosan. Analysis thereof was aided by literature.[19-21]

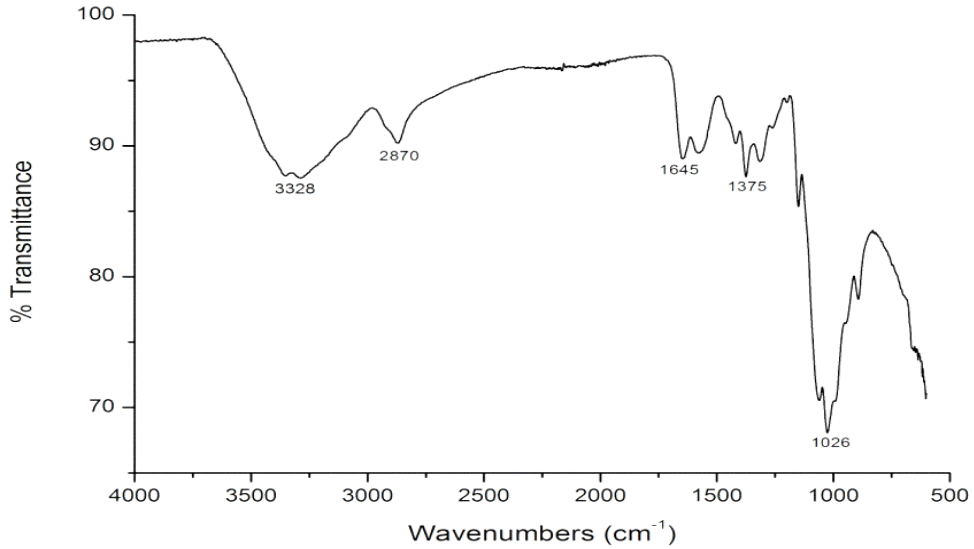

Figure 3.3 FTIR spectrum of chitosan.

Table 3.1 Summary of FTIR spectral absorption bands of chitosan

Absorption bands of chitosan	Attribution
3328 cm^{-1}	Axial stretching of O-H and N-H bonds
2870 cm^{-1}	Axial stretching of C-H bonds
1645 cm^{-1}	Axial stretching of C=O bonds, amide I
1578 cm^{-1}	Angular deformation of the N-H bonds of the amino groups
1420 – 1316 cm^{-1}	Coupling of C-N axial stretching and N-H angular deformation
1150 – 893 cm^{-1}	Glycosidic bonds, C-O and C-O-C stretches

b) ^{1}H NMR

Figure 3.4 presents the representative ^{1}H NMR spectrum of the medium molecular weight (M_w = 129 kD) chitosan with a degree of *N*-deacetylation (DDA) reported to be between 75 – 85%, as purchased. This specific polymer was used as parent polymer for all subsequent chemical modifications thereof.

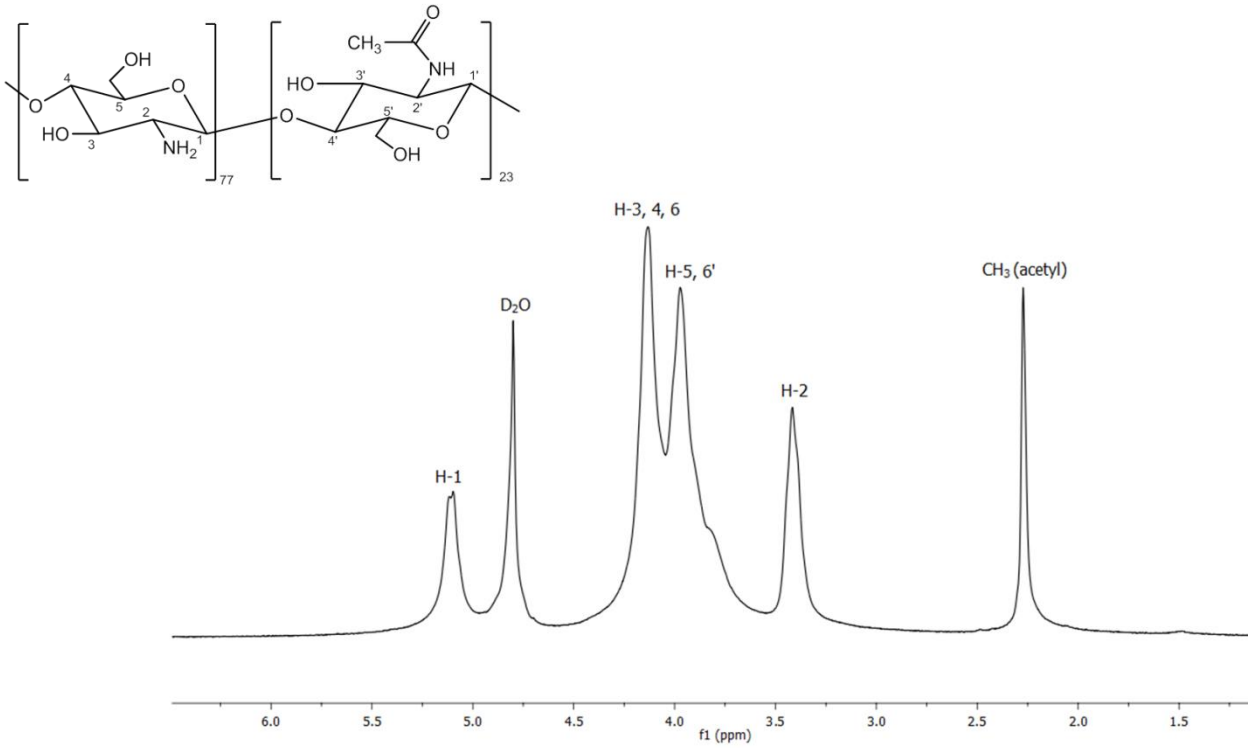

Figure 3.4 [1]H NMR spectrum of chitosan at 50°C in D_2O/HCl (100:1, v/v).

The following characteristic signals are apparent in the [1]H NMR spectrum of chitosan: (a) 5.10 ppm is attributed to the hydrogen bonded to chitosan carbon 1 (C-1); (b) 4.43 ppm is due to hydrogen atoms bonded to the C-3, C-4 and C-6 of the glycopyranose unit; (c) 4.61 - 3.02 is due to hydrogen bonded to the C-5 of the glycopyranose unit and those of C-6' of the glucopyranose unit; (d) 3.05 ppm is attributed to the hydrogen atom bonded to the C-2 of the glycopyranose ring and (e) 2.27 ppm corresponds to the hydrogen atoms of methyl moieties of the acetamido groups, overlapping with the weak acetic acid (AcOH) peak.

The DDA was empirically confirmed using the integrals of the peaks of proton H-1 of the deacetylated monomer (H-1, D) at 5.10 ppm and the three protons of the *N*-acetyl group (H-Ac) at 2.27 ppm, as determined by Equation 3.1.[22,23]

$$DDA(\%) = \left(\frac{H1D}{H1D + \frac{HAc}{3}}\right) \times 100 \qquad (3.1)$$

Chitosan is only soluble in acidic media and was therefore dissolved in dilute acid, which naturally produces the hydrolytic cleavage of the *N*-acetyl groups of chitosan to produce free AcOH.[22] Therefore, for DDA determination, both the *N*-acetyl and the AcOH signals were considered for integration. The DDA of chitosan was calculated to be 77%, reported in percentile units of 100 chitosan monomers.

3.2.2 *N*-trimethylammonium chitosan chloride (TMC)

N-trimethylammonium chitosan chloride (TMC) is the simplest form of quaternized chitosan. It is generally synthesized by chitosan reacting with excess methyl iodide in strong alkaline conditions, using *N*-methyl-2-pyrrolidone (NMP) as solvent and sodium iodide as catalyst.[24] TMC is a cationic polysaccharide and is reported to have the ability to form polyelectrolyte complexes with DNA and proteins.[25] The successful synthesis of TMC was confirmed by ATR-FTIR analysis and ^{1}H NMR spectroscopy. The structure of TMC is illustrated in Figure 3.5.

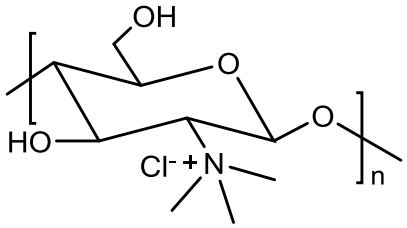

Figure 3.5 TMC.

a) ATR-FTIR

The representative FTIR spectra of (a) pristine chitosan and (b) TMC are shown in Figure 3.6. The observed IR spectrum of TMC is analogous to those found in literature.[26,27]

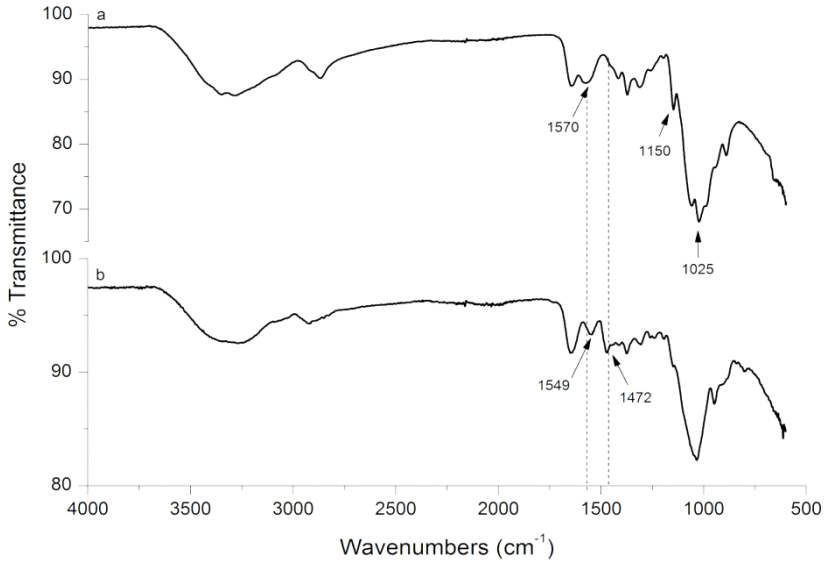

Figure 3.6 FTIR spectra of (a) pristine chitosan and (b) TMC.

Evidences of the methylation of chitosan are most noticeably observed in the region of 1700 – 1200 cm^{-1}. The band due to the angular deformation of the N-H bond of amino groups occurred in both spectra, at 1570 cm^{-1} for chitosan and at 1549 cm^{-1} for TMC, but had a lower intensity in the spectrum of TMC due to the occurrence of *N*-methylation of the primary amine. As supported by

Cao *et al*., a new deformation vibration of a C-H bond appeared at 1472 cm^{-1} in the IR spectrum of TMC, which proved that the primary amino groups of chitosan were substituted by methyl groups, confirming the trimethylation of chitosan. The characteristic absorptions of the primary and secondary alcohol groups at 1150 cm^{-1} and 1025 cm^{-1} appeared unchanged which related towards the specificity of the reaction.[25,28,29]

b) ^{1}H NMR

The NMR spectra of TMC are consistent with those found in literature.[26, 30-32] Refer to Figure 3.7 for the ^{1}H NMR spectrum of *N*-trimethylammonium chitosan chloride.

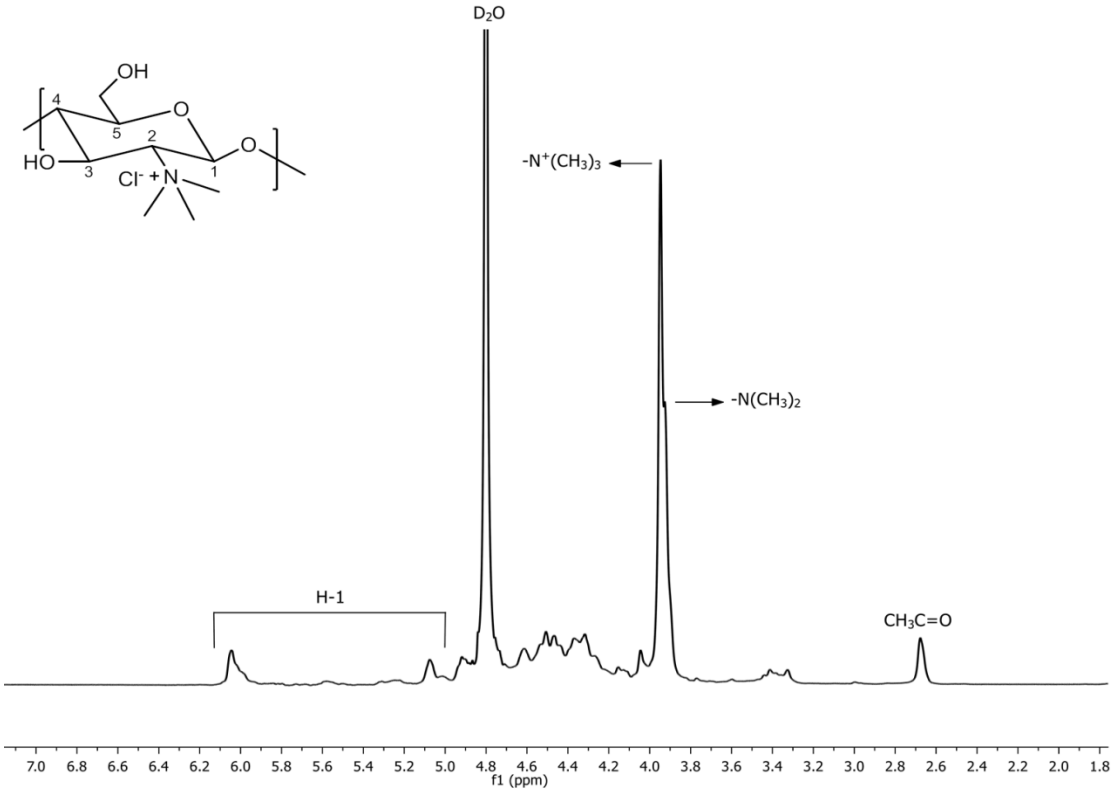

Figure 3.7 ^{1}H NMR spectrum of TMC at 80 °C in deuterated water.

In the ^{1}H NMR spectrum of TMC, a peak was observed at 2.68 ppm and was assigned to the hydrogen atoms of the methyl moieties of the acetamido groups ($CH_3C=O$). The peak at 3.93 ppm was assigned to the hydrogen atoms of the dimethylamino substituent $-N(CH_3)_2$ and at 3.95 ppm to the trimethylammonium substituent $-^{+}N(CH_3)_3$, with overlap of signals. The peaks between 4.0 – 4.2 ppm were assigned to the hydrogen atoms of the *O*-methylated groups attached to carbon atoms C-3 and C-6. The peaks between 5.0 – 6.1 ppm were assigned to hydrogen H-1 bound to the anomeric carbon C-1 attached to the hemiacetal oxygen in the polysaccharide ring. These ^{1}H peaks were used as reference peaks. The signals at 4.2 – 5.0 ppm were attributed to hydrogen

H-3, H-4, H-5 and H-6 of the glycopyranose ring and the signals at 3.2 – 3.5 ppm are assigned to hydrogen H-2 of the glycopyranose ring.

Quaternization (methylation) of the amino groups in chitosan can be achieved with methyl iodide at elevated temperature in a strong alkaline environment to bind the acid being generated during the reaction and to avoid protonation of the unreacted primary amino groups. The degree of quaternization (DQ) is influenced by various parameters such as reaction time, number of reaction steps and the DDA of the chitosan used. At higher degrees of quaternization, evidence of *O*-methylation on the C-3 and C-6 hydroxyl groups of chitosan is found. In general, *O*-methylation leads to less soluble products. It is therefore desirable to prepare *N*-trimethylammonium chitosan (TMC) polymers with a high DQ but with a low degree of *O*-methylation.[33]

To determine the degree of *O*-methylation (DOM) and degree of quaternization (DQ), the ^{1}H NMR spectrum of the quaternized products were measured at 80 °C.

The % DOM was calculated from Equation 3.2,

$$DOM\% = \left[\frac{[(CH_3)_3]}{[H]} \times \frac{1}{3}\right] \times 100 \qquad (3.2)$$

where % DOM is the degree of *O*-methylation as a percentage, $[(CH_3)_3]$ is the combined integrals of the signals at 3.59 ppm and 3.49 ppm belonging to the methyl substituted C-3 or C-6 hydroxyl groups of chitosan, respectively, and [H] is the integral of H-1 peaks between 5.0 and 6.1 ppm, related to the hydrogen atoms bound to C-1 of chitosan, which was taken as the reference signal.

The % DQ was calculated from Equation 3.3,

$$DQ\% = \left[\frac{[(CH_3)_3]}{[H]} \times \frac{1}{9}\right] \times 100 \qquad (3.3)$$

where % DQ is the degree of quaternization as a percentage, $[(CH_3)_3]$ is the integral of the signal at 3.95 ppm belonging to the trimethylammonium substituent and [H] is the integral of H-1 peaks between 5.0 and 6.1 ppm, related to the hydrogen atoms bound to C-1 of chitosan, which was taken as the reference signal.[34]

The degree of dimethylation (DM) was calculated from Equation 3.4,

$$DM\% = \left[\frac{[(CH_3)_2]}{[H]} \times \frac{1}{6}\right] \times 100 \qquad (3.4)$$

where % DM is the degree of dimethylation as a percentage, $[(CH_3)_2]$ the integral of the dimethylamino group peak at 3.93 ppm and [H] the integral of H-1 peaks between 5.0 and 6.1 ppm, related to the hydrogen atoms bound to C-1 of chitosan, which was taken as the reference signal.

Synthesized *N*-trimethylammonium chitosan chloride showed favourable degrees of substitution, having a degree of quaternization of 70%, a degree of dimethylation of 34.5% and a degree of *O*-methylation of 22.7%.

3.2.3 *N*-(2-hydroxy)propyl-3-trimethylammonium chitosan chloride (HTCC)

N-(2-hydroxy)propyl-3-trimethylammonium chitosan chloride (HTCC) is another form of quaternized chitosan, bearing additional hydroxyl and trimethylated quaternary ammonium moieties. HTCC is prepared by chemically modifying chitosan using glycidyltrimethylammonium chloride (GTMAC) in an aqueous solution. The hydroxyl groups of chitosan are not sufficiently nucleophilic to induce ring opening of GTMAC, whereas the amino groups of chitosan are nucleophilic enough and substitution therefore occurs on the C-2 position of chitosan bearing the primary amino group.[35] HTCC has been proven to show better moisture retentiveness, antimicrobial activity, absorptive property, and cell proliferative capacity, compared to pristine chitosan.[36] The successful synthesis of HTCC was confirmed by ATR-FTIR and ^{1}H NMR spectroscopy. The structure of HTCC is presented in Figure 3.8.

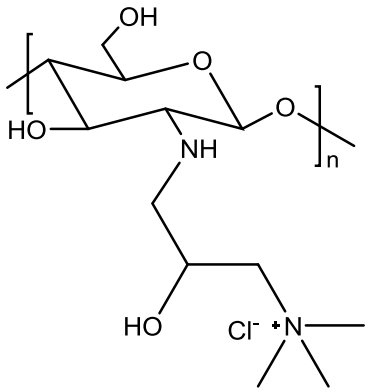

Figure 3.8 HTCC.

a) ATR-FTIR

The FTIR spectra of pristine chitosan and HTCC were analysed and compared in order to ascertain the presence of quaternary ammonium groups introduced onto chitosan's polymer backbone. The IR spectrum is consistent with reported spectra from literature.[37,38] Refer to Figure 3.9 for the representative IR spectra of pristine chitosan and *N*-(2-hydroxy)propyl-3-trimethyl ammonium chitosan chloride.

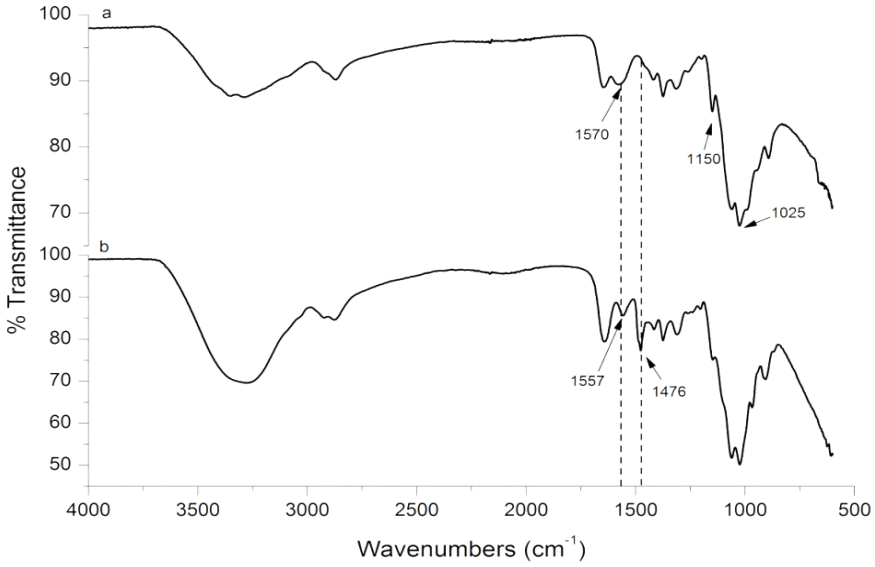

Figure 3.9 FTIR spectra of (a) pristine chitosan and (b) HTCC.

The characteristic -NH_2 band in the IR spectrum of chitosan at 1570 cm^{-1} was observed to have decreased in intensity in the spectrum of HTCC, where the -NH_2 band associated with the N-H bending in the primary amine was seen at 1557 cm^{-1}. In the HTCC IR spectrum, the appearance of a new band at 1476 cm^{-1} was attributed to the C-H asymmetric angular bending of the newly introduced methyl groups of the quaternary ammonium salt. Chitosan's characteristic peaks of the primary alcohol and secondary alcohol moieties between 1150 and 1025 cm^{-1} remained unchanged in the IR spectrum of HTCC, which confirmed the specificity of the introduction of quaternary ammonium groups at the C2-amine sites of the chitosan polymer chains.

The presence of hydrogen bonded –NH_2 and –OH functionalities was observed as the characteristic band around 3300 – 3500 cm^{-1} and absorbed at a greater intensity in the spectrum of HTCC, likely due to the inclusion of the new hydroxyl moiety which absorbs in this range.

b) ^{1}H NMR

^{1}H NMR spectroscopy was used to determine whether the ring opened quaternized GTMAC chain had been substituted onto chitosan's polymer backbone. Refer to Figure 3.10 for the representative ^{1}H NMR spectrum of HTCC.

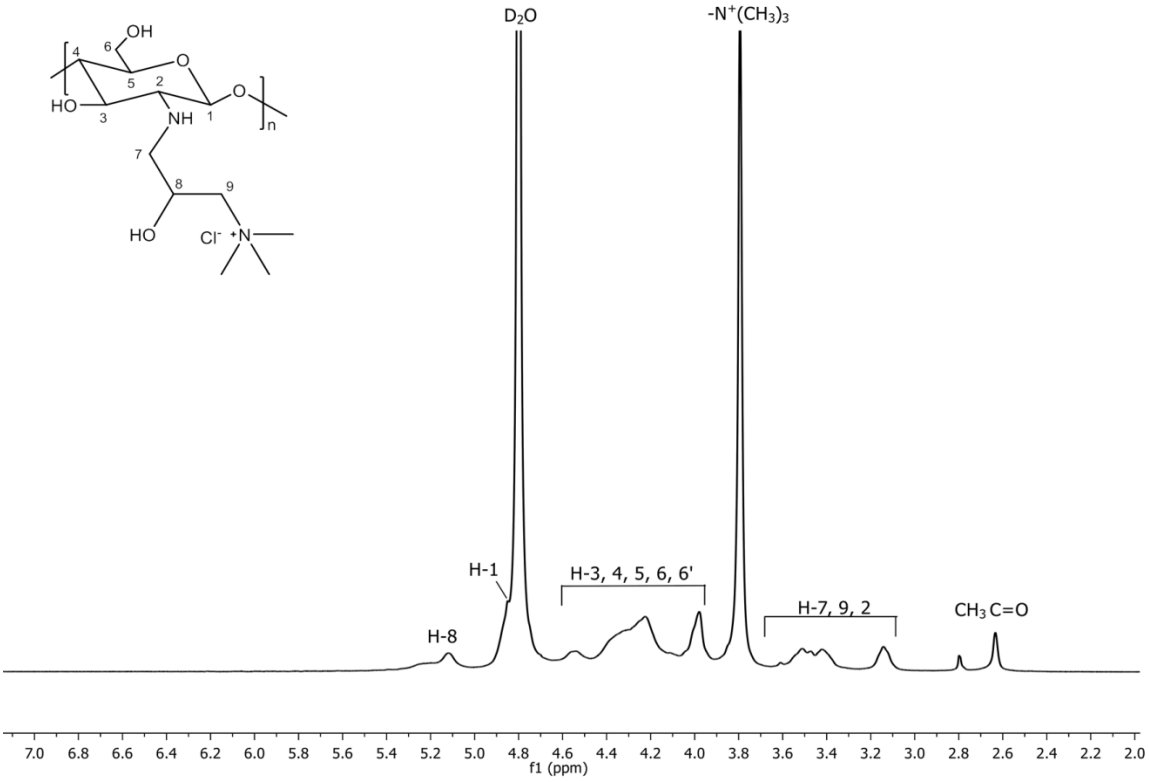

Figure 3.10 ^{1}H NMR spectrum of HTCC at 80°C in deuterated water.

The ^{1}H NMR spectra of HTCC and of pristine chitosan are similar (refer to Figure 3.4: ^{1}H NMR spectrum of pristine chitosan), with the exception of a characteristic signal at 3.79 ppm in the spectrum of HTCC. The peak at this chemical shift is not apparent in the spectrum of pristine chitosan and is attributed to the methyl protons of the quaternary ammonium salt. These results are consistent with reported spectra in literature.[23,39,40]

The degree of quaternization (DQ) was calculated for HTCC using the proportion of hydrogen atoms of the amine moiety being substituted by the quaternary ammonium salt group. This was determined by titrating the amount of Cl^- ions with silver nitrate ($AgNO_3$) aqueous solution. The Mohr method uses chromate ions as an indicator in the titration of chloride ions with a silver nitrate standard solution. After all the chloride has been precipitated as white silver chloride, the first excess of titrant results in the formation of a silver chromate precipitate, which signals the end point.[41] The DQ was thereby calculated using Equation 3.5,

$$DQ = \frac{VC}{VC+(m-VC\ x\ 314)/162} \qquad (3.5)$$

where C (mol.L^{-1}) is the concentration of the $AgNO_3$ solution, V (mL) the volume of the $AgNO_3$ solution and m (g) the mass of HTCC. The values 314 and 162 are the molecular weights in g/mol

of the repeat structural unit of HTCC and chitosan, respectively.[42] The % DQ was calculated as 85.7%.

3.2.4 Quaternized chitosan derivatives with varying alkyl chain lengths

N-propyl-3-*N'*,*N'*-dimethyl-*N'*-octylammonium chitosan chloride (CS-qC$_8$), *N*-propyl-3-*N',N'*-dimethyl-*N'*-decylammonium chitosan chloride (CS-qC$_{10}$) and *N*-propyl-3-*N',N'*-dimethyl-*N'*-dodecylammonium chitosan chloride (CS-qC$_{12}$) were synthesized via a two-step reaction involving the *N*-substitution of pristine chitosan with a suitable modification agent, followed by quaternization of the tertiary amine with the 8-carbon, 10-carbon and 12-carbon chains, respectively. The chemical structures of the chitosan derivatives prepared and characterized in this section are presented in Figure 3.11.

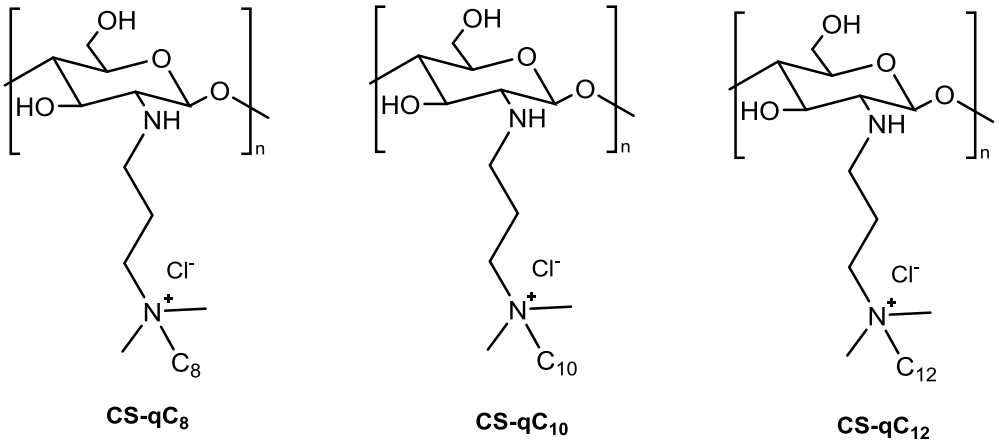

Figure 3.11 Quaternized chitosan derivatives: CS-qC$_8$, CS-qC$_{10}$ and CS-qC$_{12}$.

Each polymer differed only by two carbon atoms and accordingly had similar FTIR and NMR spectra. The successful syntheses of these polymers were confirmed by ATR-FTIR and ^{1}H NMR spectroscopy.

a) ATR-FTIR

Refer to Figure 3.12 for the representative IR spectra of CS-qC$_8$ and pristine chitosan. Shown in the inset is the normalized, superimposed spectrum of CS-qC$_8$, CS-qC$_{10}$ and CS-qC$_{12}$, which was included so as to validate the similarity.

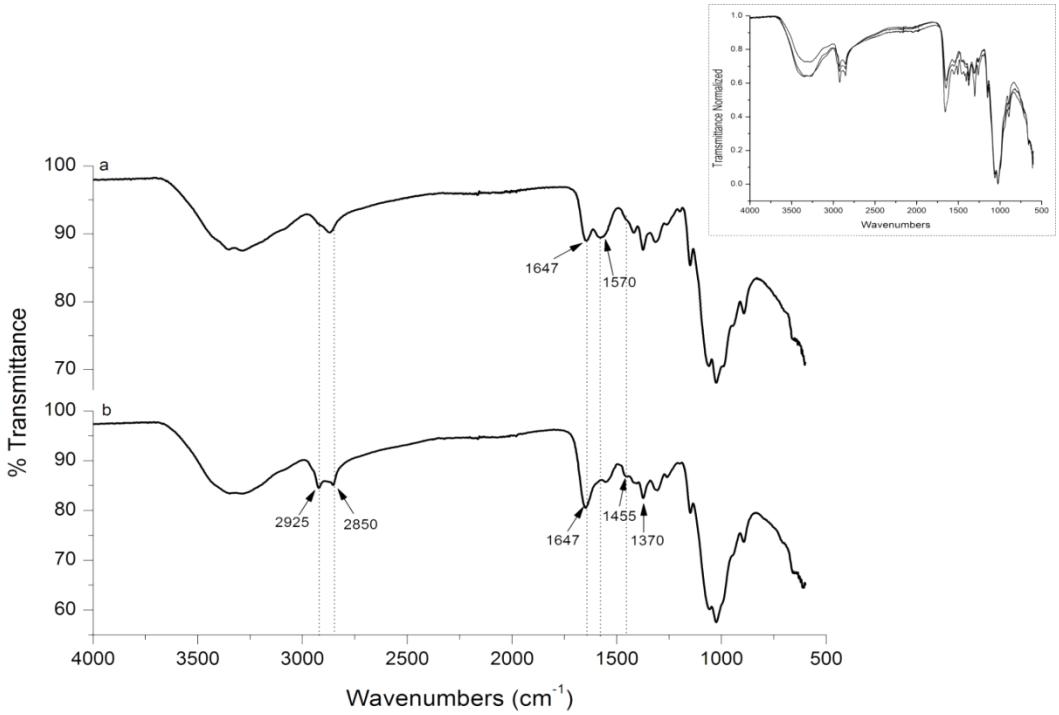

Figure 3.12 FTIR spectra of (a) pristine chitosan and (b) CS-qC$_8$. Shown in the inset is a normalized, superimposed FTIR spectrum of CS-qC$_8$, CS-qC$_{10}$ and CS-qC$_{12}$.

In the IR spectra of pristine chitosan and its quaternized derivatives, the peak corresponding to the primary amine of pristine chitosan at 1570 cm^{-1} dramatically decreases in intensity, revealing the transformation of the primary amine to the secondary amine structure due to the substitution which occurs at the NH_2 sites of chitosan.[43] The peak at 1647 cm^{-1} was assigned to the carbonyl stretching vibration of chitosan's acetamido moiety on the GlcNAc residue. The C=O bond of the amide I increases in intensity post chemical modification of chitosan, and is due to the formation of a more stable amide bond. This holds true for all quaternized chitosan derivatives. This is most likely attributed to the decrease in intramolecular hydrogen bonding of the amide, hydroxyl and amino groups of chitosan. For this reason, quaternized derivatives of chitosan display water solubility by forming hydrogen bonds with water molecules, whereas pristine chitosan does not.

The broad absorption band between 3000 – 3700 cm^{-1} (OH, NH) was evident in the spectra of both chitosan and the quaternized, alkylated chitosan derivatives. The hydrocarbon chains presented bands at 2925 and 2850 cm^{-1} and were attributed to the sp^3 C-H stretch vibration and was indicative of well-ordered alkyl chains with a trans zigzag conformation.[45] This observation was corroborated by the characteristic bending absorption of the methyl and methylene groups at 1370 and 1455 cm^{-1}, respectively. These bands increased in intensity in the spectra of CS-qC$_8$, CS-qC$_{10}$ and CS-qC$_{12}$ and also confirmed the inclusion of long chain aliphatic groups onto the chitosan polymer backbone.[44,46]

b) ^{1}H NMR

^{1}H NMR spectroscopy was used to characterize the quaternized, *N*-alkylated modifications of chitosan. The ^{1}H NMR spectra of the three modified chitosan polymers were similar, as evidenced in Figure 3.13, in which the spectra of CS-qC_8, CS-qC_{10} and CS-qC_{12} are presented in a stacked formation. Refer to Figure 3.14 for the ^{1}H NMR assignments of CS-qC_8.

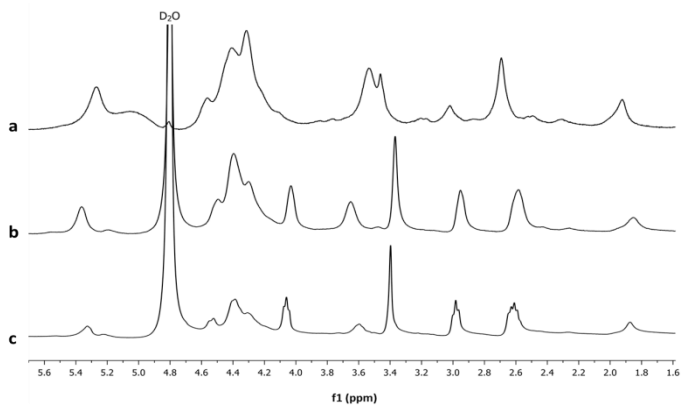

Figure 3.13 ^{1}H NMR stacked spectra of (a) CS-qC_{12}, (b) CS-qC_{10} and (c) CS-qC_8.

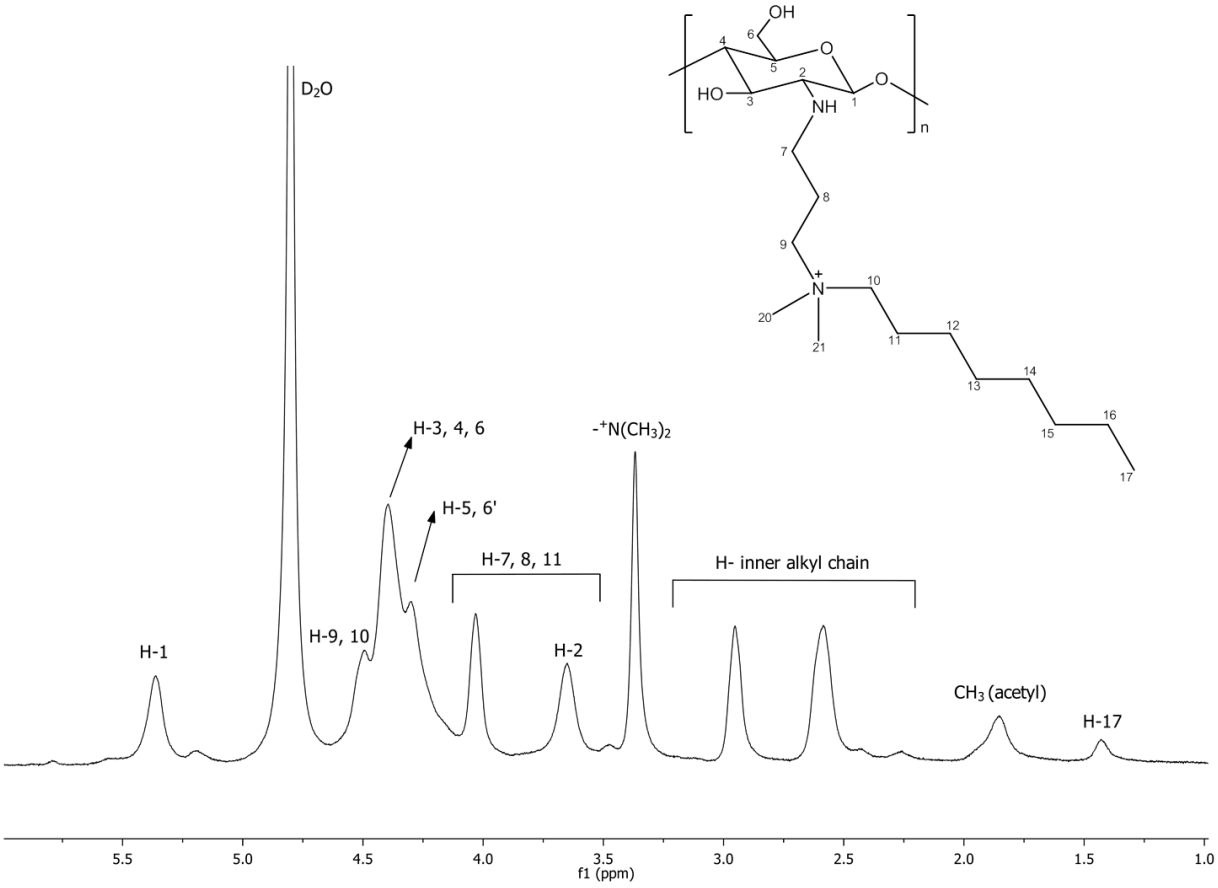

Figure 3.14 ^{1}H NMR spectrum of proton assigned qCS-C_8 at 80°C in deuterated water.

To determine the degree of quaternization (% DQ), the ^{1}H NMR spectra of the *N*-alkylated, *N*-quaternized chitosan derivatives were measured at 80 °C. The % DQ was calculated using Equation 3.6,

$$DQ\% = 1 - \left(\frac{\frac{CH_3\ (acetyl)}{3}}{H(methine)} \right) \times 100 \qquad (3.6)$$

where % DQ is the degree of quaternization as a percentage, determined by the integral area of the ^{1}H peak of the methine proton at 3.5 – 3.7 ppm related to the integral area of the methyl protons of the acetamido moiety of the GlcNAc residue at 1.9 ppm.[47] The % DQ of the quaternized chitosan derivatives was calculated to be 80.8%, 75.5% and 83.1% for CS-q$C_{8,}$ CS-qC_{10} and CS-qC_{12}, respectively.

3.3 Conclusion

The quaternized derivatives of chitosan, namely TMC, HTCC, CS-qC_8, CS-qC_{10} and CS-qC_{12} were successfully synthesized, as confirmed by ATR-FTIR spectroscopy and NMR spectroscopy. The chemical structures of the synthesized polymers were chosen based on possible chemical interaction with mycobacteria, and provide the foundation for subsequent nano-substrate formation.

3.4 Experimental

3.4.1 Materials

Chitosan (Sigma-Aldrich, M_w = 129 000, DDA 77) was used for the synthesis of *N*-trimethylammonium chitosan chloride (TMC), *N*-(2-hydroxy)propyl-3-trimethylammonium chitosan chloride (HTCC), *N*-propyl-3-*N',N'*-dimethyl-*N'*-octylammonium chitosan chloride (CS-qC_8), *N*-propyl-3-*N',N'*-dimethyl-*N'*-decylammonium chitosan chloride (CS-qC_{10}) and *N*-propyl-3-*N',N'*-dimethyl-*N'*-dodecylammonium chitosan chloride (CS-qC_{12}). The following chemicals were utilized in this part of the project: hydrobromic acid (Sigma-Aldrich, 48 wt.% in H_2O), 3-dimethylamino-1-propanol (Aldrich, 99%), *N*-methyl-2-pyrrolidone (Acros Organics, 99%), methyl iodide (Sigma-Aldrich, 99%), sodium iodide (May & Baker, 99.5%), sodium chloride (Merck, 99%), sodium hydroxide pearls (Merck, 98%), glycidyltrimethylammonium chloride (Aldrich, 90%), 1-bromooctane (Aldrich, 99%), 1-bromodecane (Aldrich, 99%), 1-bromododecane (Aldrich, 99%), acetone (Sigma-Aldrich, 99.5%), ethanol (Sigma-Aldrich, 99.5%), deuterated chloroform (Aldrich, 99.9 atom % D) and deuterium oxide (Aldrich, 99.9 atom % D).

3.4.2 Characterization Techniques

a) Attenuated total reflectance Fourier transform infrared (ATR-FTIR) spectroscopy

Infrared spectra were collected using a Nicolet FTIR spectrometer (model nexus) from Thermo-Fischer equipped with a Smart Golden gate ATR accessory with a diamond/ZnSe internal reflection crystal. The spectra were recorded from 4000 cm^{-1} to 600 cm^{-1} with a spectral resolution of 4 cm^{-1} and were the sum of 64 individual scans. No sample preparation was necessary and samples were in the solid state. Omnic software (version 8.1) was used for data acquisition and processing.

b) Nuclear magnetic resonance (NMR) spectroscopy

^{1}H NMR and ^{13}C NMR spectra were obtained using a Varian VXR 400 MHz instrument equipped with a Varian magnet (7.0 T). Depending on the solubility of the synthesized products, deuterated chloroform ($CDCl_3$) and deuterium oxide (D_2O) were used as solvents. For pristine chitosan and *N*-substituted chitosan it was necessary to acidify deuterium oxide D_2O:HCl in a 100:1 (v/v) . The residual water in the NMR sample does not pose difficulty since at 80°C the peak does not interfere with the spectra of the polymers. All chemical shifts are reported in ppm downfield from tetramethylsilane (TMS), used as an internal standard (δ = 0 ppm).

3.4.3 Experimental Procedures

a) (3-Bromopropyl)dimethylamine

The modification agent, (3-bromopropyl)dimethylamine was synthesized in order to modify the parent polymer, chitosan, and is schematically illustrated in Scheme 3.1.

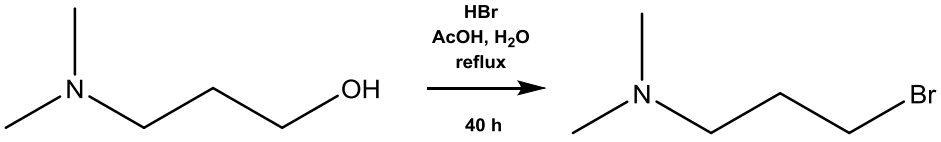

Scheme 3.1 Synthesis of (3-bromopropyl)dimethylamine.

(3-Hydroxypropyl)dimethylamine (7.5 g, 72.8 mmol) was added in acetic acid (50 mL) in an ice bath with stirring. Hydrobromic acid solution (48%, 18.2 mmol) was added to the reaction vessel dropwise and the solution was refluxed for 48 h whereafter it was concentrated under vacuum. Ethanol (200 mL) was added to the brownish residue of the crude product and the solvent was

removed via rotor evaporation. The resultant viscous, brown liquid was poured into a separating funnel and an equal amount of dichloromethane was added along with 10 mL of Milli-Q water. A three-layer separation occurred and the first layer was decanted. The organic layer was washed three times with Milli-Q water and dried over magnesium sulfate crystals for 2 h. The residual solvent was removed via rotor evaporation and was placed in a vacuum oven at 40°C for 24 h. The solid salt was re-crystallized in acetone and a needle-like light yellow crystal of 3-bromopropyl-dimethylamine hydrobromic salt was obtained (11.34 g, 94%). ^{1}H NMR (400 MHz, $CDCl_3$) δ 3.53 (s, 1H, H-8), 3.28 (t, 1H, H-2), 2.89 (d, J = 5.1 Hz, 3H, H-5, H-4), 2.52 – 2.45 (m, 1H, H-3). ^{13}C NMR (400 MHz, $CDCl_3$) δ 57 (C-2), 43.3 (C-4, C-5), 29.3 (C-3), 27.2 (C-8).

b) *N*-trimethylammonium chitosan chloride (TMC)

Quaternization (methylation) of the primary amino groups of chitosan was accomplished using methyl iodide in an alkaline solution of *N*-methyl-2-pyrrolidone. The quaternization takes place at the primary amino group of chitosan at the C-2 position via a nucleophilic substitution reaction with methyl iodide and sodium iodide used as catalysts. TMC was synthesized based on the method by Zarifpour *et al*.[48] The synthesis route is schematically illustrated in Scheme 3.2.

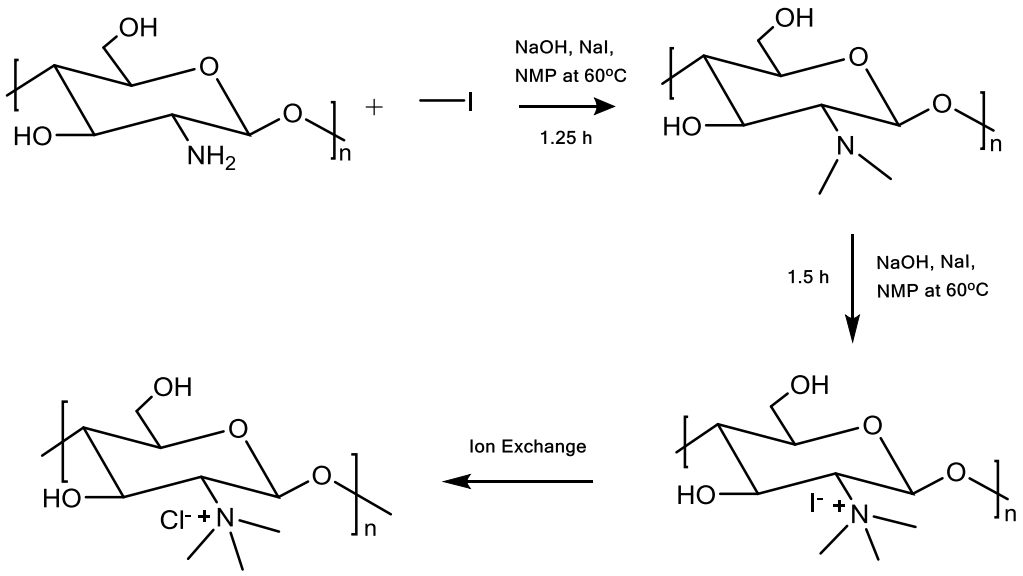

Scheme 3.2 Synthesis of TMC.

Deacetylated chitosan (2 g, 12.4 mmol) was dissolved in *N*-methyl-2-pyrrolidone (80 mL) and stirred in a 3-necked flask connected to a condensation column. A sodium hydroxide solution (15%, 11 mL) was added to the reaction flask, followed by methyl iodide (11.5 mL) and sodium iodide (4.8 g). The solution was heated to 60 °C for 75 min, precipitated in ethanol and then centrifuged (4500 rpm, 10 min). The obtained agglomerated product of dimethyl chitosan iodide was washed with acetone on a sintered glass filter and dried under vacuum at 40°C for 24 h.

In the second stage, *N*-methyl-2-pyrrolidone (80 mL) was added to the dried precipitate and the polymer solution was stirred at 60 °C until dissolved. A sodium hydroxide solution (15%, 11 mL), methyl iodide (7 mL) and sodium iodide (4.8 g) were added successively and the reaction vessel was left to stir for 30 min. An additional amount of methyl iodide (2 mL) and sodium hydroxide pearls (0.6 g) were added and stirred for 1 h. This mixture was precipitated in ethanol (200 mL) and centrifuged (4500 rpm, 10 min), before filtering with acetone on a sintered glass filter to obtain trimethyl chitosan iodide.

In the final stage, the precipitate was dissolved in a sodium chloride solution (10%, 40 mL) to obtain trimethyl chitosan chloride via halogen exchange. The solution was precipitated in ethanol (200 mL). Excess ethanol was avoided as it would precipitate the sodium chloride. The mixture was centrifuged (4500 rpm, 10 min) and the supernatant removed. The precipitate was filtered, washed with acetone and dried under vacuum at 40 °C for 24 h. The product was redissolved Milli-Q water and precipitated in acetone. The product was milled to obtain an off-white water soluble powder (2.71 g, 92%). Major IR absorptions: 3277, 2924, 1648, 1547, 1472, 1411, 1374, 1306, 1034, 948 cm^{-1}. ^{1}H NMR (400 MHz, D_2O) δ 6.1 – 5.0 (m, H-1), 5.0 – 4.2 (m, H-3, 4, 5, 6), 4.2 – 4.0 (m, -O-CH_3 x2), 3.5 – 3.2 (m, H-2), 3.95 (s, -$^{+}N(CH_3)_3$), 3.93 (s, -$N(CH_3)_2$), 2.68 (s, H_3C=O). ^{13}C NMR (400 MHz, D_2O) δ 97.2 (-C=O), 78.7 (C-1), 77.6 (C-2), 76.0 (C-4), 73.8 (C-5), 69.1 (C-3), 61.5 (C-6), 55.1 (-$^{+}N(CH_3)_3$), 53.5 (-$NH(CH_3)_2$), 42.5 (CH_3-**C**=O).

c) *N*-(2-hydroxy)propyl-3-trimethylammonium chitosan chloride (HTCC)

Glycidyltrimethylammonium chloride (GTMAC) was selected as a quaternizing agent due to its inherent quaternary ammonium group. The quaternary ammonium group inclusion is obtained after the ring-opening reaction of the primary amino group of chitosan at the C-2 position with GTMAC, schematically illustrated in Scheme 3.3.

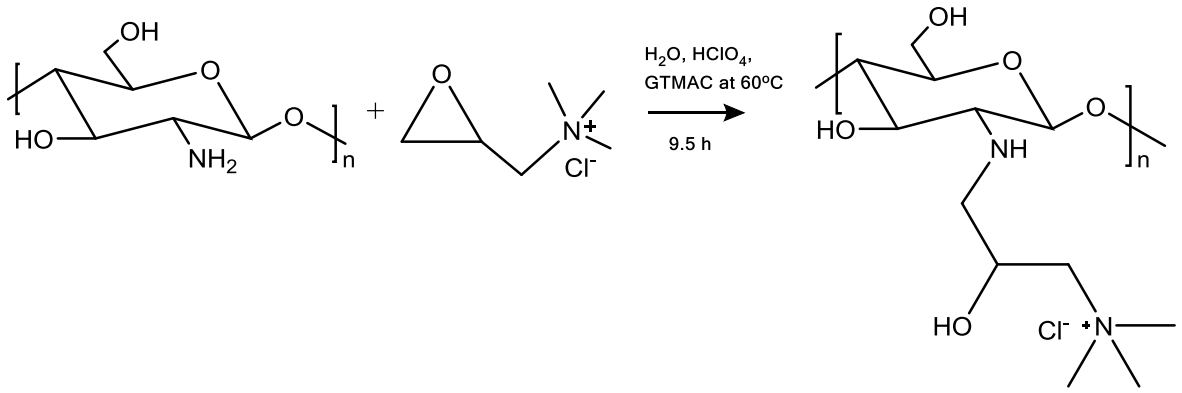

Scheme 3.3 Synthesis of HTCC.

HTCC was synthesized based upon the method of Lang *et al*.,[49] with modifications. Briefly, deacetylated chitosan (2 g, 12.3 mmol) was dispersed in Milli-Q water (60 mL) and completely dissolved by the addition of perchloric acid (1.9 g) at room temperature. An aqueous solution of glycidyltrimethylammonium chloride (15 g, 98.8 mmol) was added to the chitosan suspension at 60 °C in three equal aliquots at intervals of 30 min. This was left to react for 8 h at 80 °C. The turbid, yellowish reaction solution was precipitated in acetone yielding the product. After washing with acetone several times, the product was redissolved in Milli-Q water and precipitated in acetone. The product was filtered and dried under vacuum at 60°C for 24 h (2.67 g, 70%). Major IR absorptions: 3277, 2878, 1641, 1559, 1476, 1417, 137, 1312, 1061, 1024, 907 cm^{-1}. ^{1}H NMR (400 MHz, D_2O) δ 5.12 (m, H-8), 4.85 (s, H-1), 4.56 – 3.25 (m, H-3, 4, 5, 6, 6'), 3.79 (s, $-^{+}N(CH_3)_3$), 3.6 – 3.1 (m, H-7, 9, 2), 2.6 (s, $H_3C{=}O$). ^{13}C NMR (400 MHz, D_2O) δ 103.2 (C-1), 79.3 (C-5), 75.7 (C-4), 70.2 (C-2), 65.9 (C-9), 61.3 (C-6), 55.1 ($-^{+}N(CH_3)_3$), 52.6 (C-7), 23.1 (CH_3-**C**=O).

d) Synthesis of *N*-propyl-3-dimethylamino (*N*-substituted) chitosan

N-Substitution of chitosan happens selectively via a halogen displacement reaction or reductive amination. The direct *N*-substitution of chitosan was achieved by the reaction between the primary amino groups of chitosan and the alkyl halide of the modification agent under heterogeneous conditions in the presence of a strong base. *N*-substituted chitosan and *N*-quaternized chitosan polymers were synthesized based on the method by Guo *et al*. and Cronje, schematically illustrated in Scheme 3.4.[49,50]

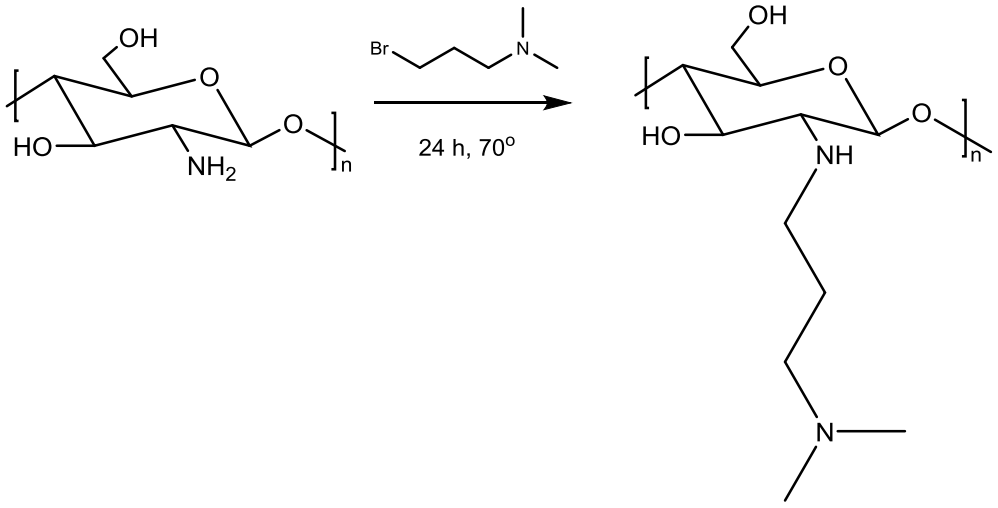

Scheme 3.4 Synthesis of N-substituted chitosan.

Deacetylated chitosan (2 g) was dispersed in isopropanol (60 mL) and 4 M sodium hydroxide solution at 70 °C for 24 h. (3-Bromopropyl)dimethylamine in isopropanol (1.2 molar excess, 20 mL) was added dropwise to the mixture and stirred at 70 °C for 24 h. A colour change was observed

from white to yellow. The solution was precipitated in ethanol (250 mL), centrifuged (4000 rpm, 15 min) and filtered through a sintered glass filter. The resulting off-white powder was then dried under vacuum at 40 °C for 24 h (1.96 g, 98%). Major IR Absorptions: 3358, 2883, 1582, 1476, 1371, 1148, 1022, 892 cm^{-1}.^{1}H NMR (400 MHz, D_2O) δ 5.17 – 4.82 (m, H-1), 4.21 – 4.05 (m, H-5, 6'), 3.95 (m, H-3, 4, 6), 3.31 – 3.12 (m, H-2, -NH-C**H$_2$**-, -N-C**H$_2$**-), 2.34 (d, H_3C=O, -CH_2-C**H$_3$**-CH_2-), 2.19 (-N-C**H$_3$** x2). ^{13}C NMR (400 MHz, D_2O) δ 100.4 (C-1), 78.0 (C-4), 75.6 (C-5), 75.2 (-N-**C**H_2-), 72.5 (C-3), 61.0 (C-6), 56.9 (C-2), 56.3 (-NH-**C**H_2-), 23.9 (-N-CH_3 x2), 22.9 (-CH_2-**C**H_2-CH_2-).

e) Preparation of Quaternized Chitosan Derivatives

Quaternized chitosan derivatives were synthesized by modifying chitosan via the precursor polymer *N*-substituted chitosan to yield the relevant modified chitosan derivatives, schematically illustrated in Scheme 3.5. *N*-substituted chitosan took on a dark orange hue post bromoalkylation, indicative of quaternized nitrogen atoms. The tertiary amine of *N*-substituted chitosan has a lone pair of electrons which preferentially attack the more electropositive carbon attached to bromine, yielding the quaternized chitosan polymers.

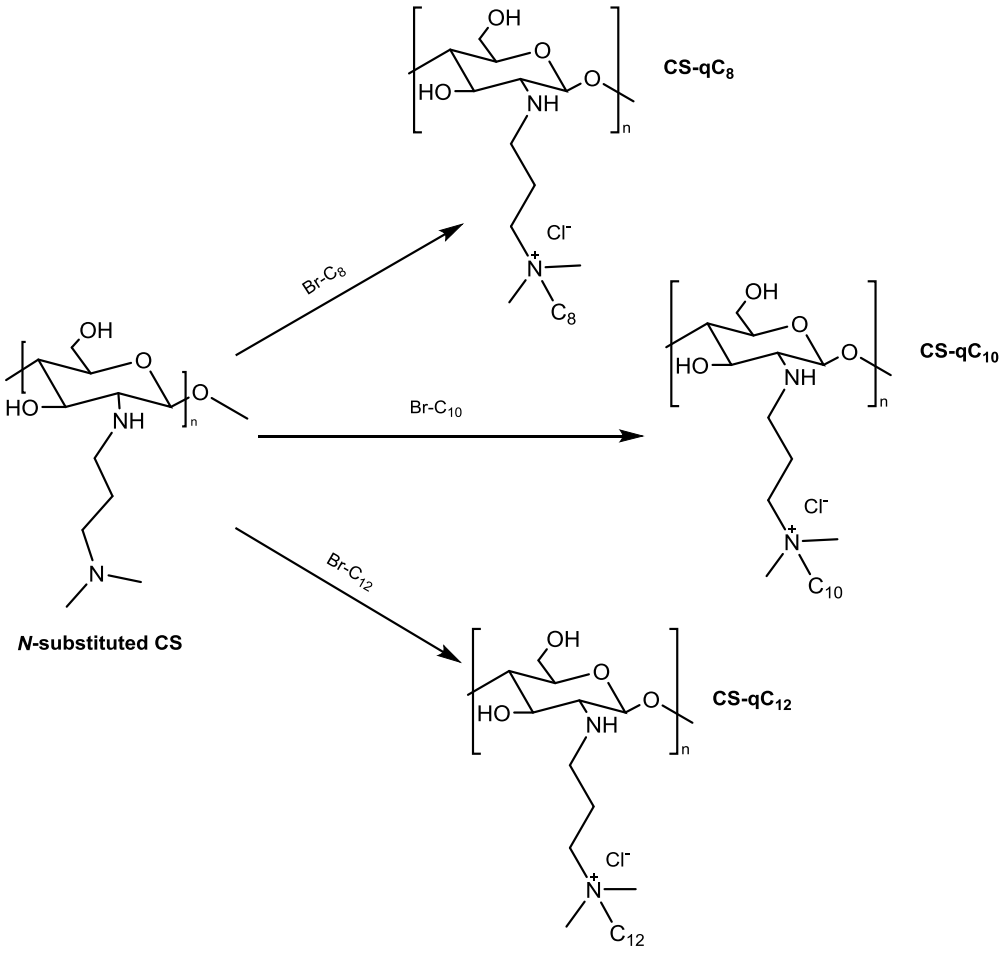

Scheme 3.5 Modification of N-substituted chitosan to yield relevant quaternized chitosan polymers.

i) *N*-propyl-3-*N',N'*-dimethyl-*N'*-octylammonium chitosan chloride (CS-qC$_8$)

To prepare the quaternized chitosan derivative (CS-qC$_8$), *N*-substituted chitosan (1 g) was dispersed in *N*-methyl-2-pyrrolidone (50 mL) for 24 h, after which 1-bromooctane (1.5 molar excess) was added to the reaction vessel in a dropwise manner. The solution was heated to 100 °C and left to stir for 48 h. The polymer was precipitated in excess acetone and dissolved in a sodium chloride solution (10%, 40 mL). It was then reprecipitated in acetone, filtered and dried under vacuum at 60°C for 24 h (1.47 g, 91%). Major IR absorptions: 3310, 2925, 2851, 1647, 1554, 1456, 1370, 1306, 1151, 1026, 892 cm^{-1}.^{1}H NMR (400 MHz, D_2O) δ 5.36 (m, H-1), 4.50 (m, H-9, 10), 4.40 (m, H-3, 4, 6), 4.30 (m, H-5, 6'), 4.03 – 3.42 (m, H-7, 8, 11), 3.65 (s, H-2), 3.37 (-$^+$N(CH$_3$)$_2$), 3.01 – 2.48 (-CH$_2$-), 1.90 (H$_3$C=O), 1.43 (H-17). ^{13}C NMR (400 MHz, D_2O) δ 99.8 (C-1), 78.4 (C-4), 75.7 (C-3), 72.1 (C-3), 61.3 (C-6), 61.1 (-NH-**C**H$_2$-), 57.0 (C-2), 56.5 (-N-**C**H$_2$ x2), 51.1 (-N-**C**H$_3$ x2), 31.6 (-**C**H$_2$-), 31.4 (-**C**H$_2$-), 30.2 (-**C**H$_2$-), 28.6 (-**C**H$_2$-), 22.8 (-**C**H$_2$-CH$_3$), 17.9 (-**C**H$_3$).

ii) *N*-propyl-3-*N',N'*-dimethyl-*N'*-decylammonium chitosan chloride (CS-qC$_{10}$)

To prepare the quaternized chitosan derivative (CS-qC$_{10}$), *N*-substituted chitosan (1 g) was dispersed in *N*-methyl-2-pyrrolidone (50 mL) for 24 h, after which 1-bromodecane (1.5 molar excess) was added to the reaction vessel in a dropwise manner. The solution was heated to 100 °C and left to stir for 48 h. The polymer was precipitated in excess acetone and dissolved in a sodium chloride solution (10%, 40 mL). It was then reprecipitated in acetone, filtered and dried under vacuum at 60°C for 24 h (1.53 g, 88%). Major IR absorptions: 3310, 2925, 2851, 1647, 1554, 1456, 1370, 1306, 1151, 1026, 892 cm^{-1}. ^{1}H NMR (400 MHz, D_2O) δ 5.32 (m, H-1), 4.52 (m, H-9, 10), 4.39 (m, H-3, 4, 6), 4.31 (m, H-5, 6'), 4.13 – 3.46 (m, H-7, 8, 11), 3.60 (s, H-2), 3.40 ($^+$N(CH$_3$)$_2$), 3.03 – 2.50 (-CH$_2$-), 1.88 (H$_3$C=O), 1.45 (H-19). ^{13}C NMR (400 MHz, D_2O) δ 100.7 (C-1), 78.6 (C-4), 75.7 (C-5), 72.8 (C-3), 61.3 (C-6), 61.1 (-NH-**C**H$_2$-), 57.1 (C-2), 56.6 (-N-**C**H$_2$ x2), 51.0 (-N-**C**H$_3$ x2), 31.5 (-**C**H$_2$-), 30.1 (-**C**H$_2$-), 29.5 (-**C**H$_2$-), 29.1 (-**C**H$_2$), 27.7 (-**C**H$_2$-), 23.0 (-**C**H$_2$-), 22.7 (-**C**H$_2$-CH$_3$), 17.9 (-**C**H$_3$).

iii) *N*-propyl-3-*N',N'*-dimethyl-*N'*-dodecylammonium chitosan chloride (CS-qC$_{12}$)

To prepare the quaternized chitosan derivative (CS-qC$_{12}$), *N*-substituted chitosan (1 g) was dispersed in *N*-methyl-2-pyrrolidone (50 mL) for 24 h, after which 1-bromododecane (1.5 molar excess) was added to the reaction vessel in a dropwise manner. The solution was heated to 100 °C and was left to stir for 48 h. The polymer was precipitated in excess acetone and dissolved in a sodium chloride solution (10%, 40 mL). It was then reprecipitated in acetone, filtered and dried under vacuum at 60°C for 24 h (1.68 g, 90%). Major IR absorptions: 3310, 2925, 2851, 1648,

1554, 1456, 1370, 1306, 1151, 1026, 892 cm^{-1}. ^{1}H NMR (400 MHz, D_2O) δ 5.26 (m, H-1), 4.56 (m, H-9, 10), 4.40 (m, H-3, 4, 6), 4.31 (m, H-5, 6'), 4.20 – 3.50 (m, H-7, 8, 11), 3.50 (s, H-2), 3.42 ($-^{+}N(CH_3)_2$), 3.23 – 2.20 ($-CH_2-$), 1.90 ($H_3C=O$), 1.47 (H-21). ^{13}C NMR (400 MHz, D_2O) δ 101.8 (C-1), 78.9 (C-4), 74.8 (C-5), 72.8 (C-3), 61.4 (C-6), 61.0 (-NH-**C**H_2-), 57.3 (C-2), 56.5 (-N-**C**H_2- x2), 51.9 (-N-**C**H_3 x2), 30.2 (-**C**H_2-), 29.5 (-**C**H_2-), 29.4 (-**C**H_2- x2), 27.8 (-**C**H_2- x3), 27.7 (-**C**H_2CH_3), 23.1 (-**C**H_2-CH_3), 20.2 (-**C**H_3).

3.5 References

1. Baldrick, P. *Regul. Toxicol. Pharm.* **2010***, 3,* 290-299.
2. Dodane, V.; Vilivalam, V. D. *Pharm. Sci. Technol. Today* **1998***, 6,* 246-253.
3. Kumar, S.; Dutta, J.; Dutta, P. *Int. J. Biol. Macromol.* **2009***, 4,* 330-337.
4. Dash, M.; Chiellini, F.; Ottenbrite, R.; Chiellini, E. *Prog. Polym. Sci.* **2011***, 8,* 981-1014.
5. Alves, N.; Mano, J. *Int. J. Biol. Macromol.* **2008***, 5,* 401-414.
6. Badawy, M. E.; Rabea, E. I. *Int. J. Carbohyd. Chem.* **2011**.
7. Nicu, R.; Bobu, E.; Miranda, R.; Blanco, A. *BioResources* **2012***, 1,* 768-784.
8. Kumar, M. R.; Muzzarelli, R.; Muzzarelli, C.; Sashiwa, H.; Domb, A. *Chem. Rev.* **2004***, 12,* 6017-6084.
9. Sahariah, P.; Benediktssdóttir, B. E.; Hjálmarsdóttir, M. Á.; Sigurjonsson, O. E.; Sørensen, K. K.; Thygesen, M. B.; Jensen, K. J.; Másson, M. *Biomacromolecules* **2015***, 5,* 1449-1460.
10. Rabea, E. I.; Badawy, M. E.; Stevens, C. V.; Smagghe, G.; Steurbaut, W. *Biomacromolecules* **2003***, 6,* 1457-1465.
11. Van Wachem, P.; Beugeling, T.; Feijen, J.; Bantjes, A.; Detmers, J.; Van Aken, W. *Biomaterials* **1985***, 6,* 403-408.
12. Van Wachem, P.; Hogt, A.; Beugeling, T.; Feijen, J.; Bantjes, A.; Detmers, J.; Van Aken, W. *Biomaterials* **1987***, 5,* 323-328.
13. Tamada, Y.; Ikada, Y. *Springer* **1986**, 101-115.
14. Arima, Y.; Iwata, H. *Biomaterials* **2007***, 20,* 3074-3082.
15. Cunha, R. A.; Franca, E. F.; Pontes, F. J.; Lins, R. D.; Soares, T. A.; Rusu, V. H. INTECH **2012**.
16. Guibal E. *ChemInform*. **2006**, *2*, 37.
17. Goddard, E. D.; Gruber, J. V. CRC Press **1999**.
18. Sannan, T.; Kurita, K.; Iwakura, Y. *Die Makromol. Chem.* **1976***, 12,* 3589-3600.
19. Paulino, A. T.; Simionato, J. I.; Garcia, J. C.; Nozaki, J. *Carbohydr. Polym.* **2006***, 1,* 98-103.
20. Sionkowska, A.; Wisniewski, M.; Skopinska, J.; Kennedy, C.; Wess, T. *Biomaterials* **2004***, 5,* 795-801.
21. Qi, L.; Xu, Z.; Jiang, X.; Hu, C.; Zou, X. *Carbohydr. Res.* **2004***, 16,* 2693-2700.
22. Lavertu, M.; Xia, Z.; Serreqi, A.; Berrada, M.; Rodrigues, A.; Wang, D.; Buschmann, M.; Gupta, A. *J. Pharm. Biomed. Anal.* **2003***, 6,* 1149-1158.

23. Ji, Q. X.; Lü, R.; Zhang, W. Q.; Deng, J.; Chen, X. G. *Carbohydr. Res.* **2009***, 11,* 1297-1302.

24. Xu, T.; Xin, M.; Li, M.; Huang, H.; Zhou, S. *Carbohydr. Polym.* **2010***, 4,* 931-936.

25. Ding, Y.; Xia, X.; Zhang, C. *Nanotechnology* **2006***, 16,* 4156.

26. Mourya, V.; Inamdar, N. N. *J. Mater. Sci. Mater. Med.* **2009***, 5,* 1057-1079.

27. Cao, J.; Sun, J.; Wang, X.; Li, X.; Deng, Y. *Drug Dev. Ind. Pharm.* **2009***, 11,* 1339-1347.

28. Li, Z.; Guan, J. *Expert Opin. Drug Del.* **2011***, 8,* 991-1007.

29. Le Dung, P.; Milas, M.; Rinaudo, M.; Desbrières, J. *Carbohydr. Polym.* **1994***, 3,* 209-214.

30. Rúnarsson, Ö. V.; Holappa, J.; Malainer, C.; Steinsson, H.; Hjálmarsdóttir, M.; Nevalainen, T.; Másson, M. *Eur. Polym. J.* **2010***, 6,* 1251-1267.

31. Sieval, A.; Thanou, M.; Kotze, A.; Verhoef, J.; Brussee, J.; Junginger, H. *Carbohydr. Polym.* **1998***, 2,* 157-165.

32. Thanou, M.; Kotze, A.; Scharringhausen, T.; Luessen, H.; De Boer, A.; Verhoef, J.; Junginger, H. *J. Crs. Bui. Nat.* **2000***, 1,* 15-25.

33. Amidi, M.; Romeijn, S. G.; Borchard, G.; Junginger, H. E.; Hennink, W. E.; Jiskoot, W. *J. Crs. Bui. Nat.* **2006***, 1,* 107-116.

34. Mourya, V.; Inamdar, N. N. *React Funct. Polym.* **2008***, 6,* 1013-1051.

35. Xiao, B.; Wang, X.; Qiu, Z.; Ma, J.; Zhou, L.; Wan, Y.; Zhang, S. *J. Biomed. Mater. Res. A* **2013***, 7,* 1888-1897.

36. Shi, W.; Ji, Y.; Zhang, X.; Shu, S.; Wu, Z. *J. Pharm. Sci.* **2011***, 3,* 886-895.

37. Kim, Y. H.; Nam, C. W.; Choi, J. W.; Jang, J. *J Appl Polym Sci* **2003***, 6,* 1567-1572.

38. Xu, Y.; Du, Y.; Huang, R.; Gao, L. *Biomaterials* **2003***, 27,* 5015-5022.

39. Wu, J.; Su, Z.; Ma, G. *Int. J. Pharm.* **2006***, 1,* 1-11.

40. de Britto, D.; Assis, O. B. *Carbohydr. Polym.* **2007***, 2,* 305-310.

41. Korkmaz, D. *Methods* **2001***, 4*.

42. Huang, J.; Cheng, Z.; Xie, H.; Gong, J.; Lou, J.; Ge, Q.; Wang, Y.; Wu, Y.; Liu, S.; Sun, P. *Int. J. Biol. Macromol.* **2014**, 545-550.

43. Wan, Y.; Peppley, B.; Creber, K. A.; Bui, V. T.; Halliop, E. *J. Power Sources* **2008***, 1,* 183-187.

44. Pavia, D.; Lampman, G.; Kriz, G.; Vyvyan, J. *Introduction to spectroscopy;* Cengage Learning, **2008**.

45. Haro, M.; Giner, B.; Lafuente, C.; López, M. C.; Royo, F. M.; Cea, P. *Langmuir* **2005***, 7,* 2796-2803.

46. Li, F.; Liu, W. G.; De Yao, K. *Biomaterials* **2002***, 2,* 343-347.

47. Sajomsang, W.; Gonil, P.; Tantayanon, S. *Int. J. Biol. Macromol.* **2009***, 5,* 419-427.

48. Zarifpour, M.; Hadizadeh, F.; Iman, M.; Tafaghodi, M. *Transport* **2013**, *4*.

49. Lang, G.; Wendel, H.; Konrad, E. *Process for making quaternary chitosan derivatives for cosmetic agents.* U.S. Patent 4, 921, 949, **1990**.

50. Cronje, L. *Eur. Polym. J.* **2013**, *12,* 3814-3824.

Chapter Four

Synthesis and Characterization of Superparamagnetic Magnetite Nanoparticles and Nanocomposite Materials

4.1 Synthesis of pristine and polymer coated magnetic nanoparticles

4.1.1 Nanoparticle Formation

In a classical synthesis of inorganic nanoparticles, the precursor compound in bulk solution is decomposed to generate atoms. This is followed by precipitation originating from dissolved atoms as building blocks to form the nanoparticles. The precipitation process consists of a nucleation step followed by crystal growth stages.[1]

Generally, there are three kinds of nucleation processes: homogeneous nucleation, heterogeneous nucleation and secondary nucleation. For the chemical nanoparticle synthesis, homogeneous nucleation occurs in the absence of a solid interface by combining solute molecules to produce nuclei. Homogeneous nucleation occurs due to the driving force of thermodynamics because the supersaturated solution is not energy stable. The principles by which monodisperse (standard deviation ~5%) particles can be prepared by liquid phase synthesis are presented by the LaMer diagram, schematically illustrated in Figure 4.1.[2,3]

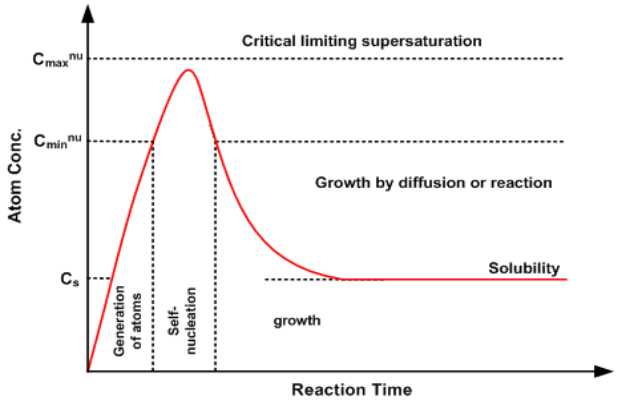

Figure 4.1 LaMer diagram illustrating the pathway for nanoparticle growth.

The requirements for monodispersity are evident from the LaMer diagram, namely:

(1) The rate of nucleation must be high enough so that the concentration does not continue to increase. Instead, a burst of nuclei is created in a short period of time (self-nucleation period).
(2) The rate of growth of these nuclei must be rapid enough to promptly reduce the concentration below the nucleation concentration point. In this way only a limited number of particles are created.
(3) The rate of growth must, however, be slow enough so that the growth period is long compared to the nucleation period. This typically narrows the size of distribution which results from finite nucleation period.[3]

So, by controlling these factors monodisperse superparamagnetic nanoparticles can be obtained.

4.1.2 Synthesis of pristine SPMNs via the co-precipitation technique

The co-precipitation of ferrous (Fe^{2+}) and ferric (Fe^{3+}) ions in an aqueous environment is a commonly used method for the synthesis of superparamagnetic magnetite nanoparticles (SPMNs) as it does not require any hazardous organic solvents or extreme conditions of pressure or temperature.[4] Also, its simplicity makes scaling-up procedures a viable option.

Massart was the first to report this method, in which the addition of a strong base to an aqueous solution of ferrous and ferric ions in a 2:1 stoichiometric ratio produced a black precipitate of spherical magnetite nanoparticles of uniform sizes in an oxygen free environment.[4,6] The control of the size, shape and composition of the nanoparticles depends on the type of salts used (e.g. chlorides, sulphates, nitrates and perchlorates), the Fe^{2+} and Fe^{3+} ratio, pH, stirring speed, order of reactants and ionic strength of the media.

The simplified chemical reaction of Fe_3O_4 precipitation is presented in Reaction 4.1 below:

$$Fe^{2+} + 2Fe^{3+} + 8OH^- \rightarrow Fe_3O_4 + 4H_2O \quad (4.1)$$

According to the thermodynamics of this reaction, a complete precipitation of Fe_3O_4 should be expected between pH 9 and 14, while maintaining a 2:1 molar ratio of Fe^{3+}:Fe^{2+} under a non-oxidising environment. Magnetite nanoparticles are unstable in ambient conditions, and in the presence of oxygen may undergo oxidation to Iron(III) oxide-hydroxide ($Fe(OH)_3$) as per Reaction 4.2, or to maghemite (γ-Fe_2O_3) according to Reaction 4.3.

$$Fe_3O_4 + \frac{1}{4}O_2 + 4\frac{1}{2}H_2O \rightarrow 3Fe(OH)_3 \quad (4.2)$$

$$2Fe_3O_4 + \frac{1}{2}O_2 \rightarrow 3Fe_2O_3 \quad (4.3)$$

To control the reaction kinetics, which is strongly related to the oxidation speed of the iron species, the synthesis of the nanoparticles must take place in an inert gas atmosphere. Bubbling of an inert gas such as argon or nitrogen gas through the solution not only protects the critical oxidation of magnetite but also reduces the particle size when compared to methods without removing oxygen.[7-9]

Iida *et al*. synthesized nanoparticles by hydrolysis in an aqueous solution containing ferrous and ferric salts at various ratios.[10] They found that when the ratio of ferrous to ferric ions was increased, it resulted in an increase in the size of Fe_3O_4 nanoparticles. During the synthesis of Fe_3O_4 (magnetite), precipitation at temperatures below 60 °C typically produces an amorphous hydrated oxyhydroxide which is readily converted to Fe_3O_4. At higher reaction temperatures (over 80 °C) the formation of Fe_3O_4 is favoured. A suitable pH for the rapid formation of Fe_3O_4 is attained by the addition of excess base. Shen *et al.* observed that the product displayed a brownish colour, an indication of the presence of maghemite (γ-Fe_2O_3), if the reaction temperature was below 60 °C or if an insufficient amount of base was added.[11] Hong *et al.* observed that when Fe_3O_4 nanoparticles were precipitated using ammonium hydroxide instead of sodium hydroxide as base, a nanoparticle with better crystallinity, higher saturation magnetization and smaller size can be observed.[2] An increase in the rate of stirring tends to decrease the particle size. In the same way, a decrease of size and greater monodispersity is observed when the base is added to the reactant in comparison with reactant added to the base.[12]

4.1.3 Synthesis of modified chitosan coated SPMNs via the *in situ* co-precipitation technique

For biomedical applications, chitosan coated SPMNs are generally synthesized via an *in situ* coating method, namely, an alkaline co-precipitation of Fe^{2+} and Fe^{3+} precursors in aqueous solutions of hydrophilic chitosan polymers. The polymer is first solubilised in acidic media before the co-precipitation takes place. Chitosan serves to 1) limit the core growth of magnetite during the nucleation stage, 2) stabilize the nanoparticles via steric repulsions when the nanoparticles disperse in aqueous media, and 3) reduce the opsonization process *in vivo*.[13]

Alcohol, amine, amide and ether functional groups present in the chitosan structure can be involved in the formation of hydrogen bonds with substrates by inter- or intramolecular hydrogen bonding, and allow complex formation with metal oxide surfaces. Chitosan coated magnetic nanoparticles therefore become promising candidates for many biomedical applications, due to the core and shell having properties of hydrophilicity,[14] stability,[15] biocompatibility,[16] non-toxicity,[17] bioadhesion (prolonged interaction with biological tissue)[18] and dispersibility in aqueous or organic media.[19] It has also been hypothesized that chitosan directly interacts with cell membranes.[20] In addition, due to the magnetic properties of the iron oxide core, easy separation from the sorption media can be achieved by applying a magnetic field.

4.2 Results and Discussion

The aim of this section of the study was to synthesize and characterize pristine superparamagnetic magnetite nanoparticles (SPMNs) as well as the modified chitosan coated SPMN nanocomposites.

4.2.1 Powder X-ray diffraction

Powder X-ray diffraction (P-XRD) was used to determine the crystallinity and the phase purity of the synthesized pristine Fe_3O_4 nanoparticles. Figure 4.2 shows the representative XRD diffractogram of pristine (uncoated) SPMNs.

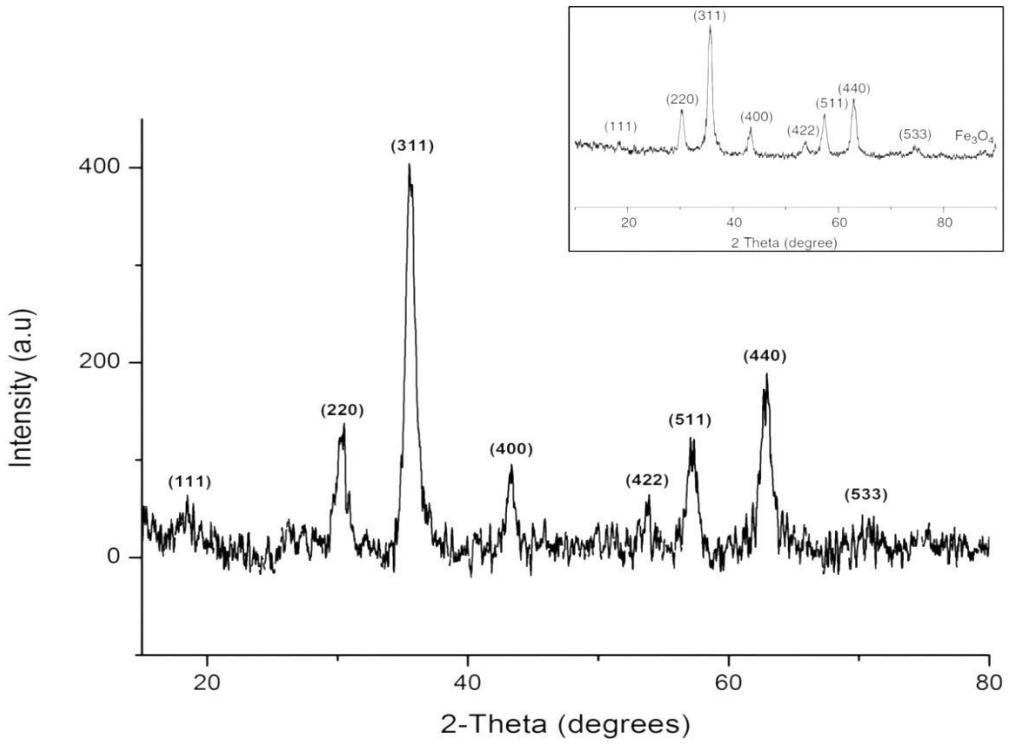

Figure 4.2 Indexed X-ray diffractogram pattern of uncoated Fe_3O_4 nanoparticles.

The relative intensity of the pattern is related to the degree of crystallinity of the material. The XRD diffractogram indicated that the resulting powder attained was consistent with the expected composition of iron oxide (Fe_3O_4). Shown in the inset is an XRD pattern from literature.[21] The results obtained were compared with standard magnetite patterns. In all cases, the XRD pattern shows characteristic peaks at 2θ = 18.2°, 30.0°, 35.4°, 43.0°, 53.4°, 56.9°, 62.5°, and 74.0° corresponding to (111), (220), (311), (400), (422), (511), (440), and (533) planes respectively, and provided clear evidence of the cubic inverse spinel structure. The pattern of the pristine SPMN powder is in good agreement with the database fingerprint pattern of Fe_3O_4. The positions and relative intensities of the diffraction peaks confirmed the crystallization of standard magnetite (Joint Committee on Powder Diffraction Standards, JCPDS file No. 19-0629).

The relatively broad Bragg reflection peaks are an indication of a smaller ordering of diffracting planes, which relates to smaller dimensions of crystallite grain and nanoparticle size. No peaks of any other phases, e.g. maghemite (γ-Fe_2O_3) are detected, indicating phase purity. Maghemite (γ-Fe_2O_3) peaks, such as (110), (210), (211), are not found in the diffractogram of the synthesized nanoparticles, the intensities of which would be stronger than that of (111). Maghemite is reported to have an orange-brown hue, whilst that of magnetite is black.[22] The sample colour (black), lattice spacing and lattice parameter aid the conclusion of phase purity in that Fe_3O_4 is the dominant phase. It cannot be ascertained from the XRD patterns whether the oxidized hematite ($\propto$-Fe_2O_3) phase is present in the sample due to similar lattice type and parameters.[23]

The crystallization of Fe_3O_4 nanoparticles at the strongest diffraction peak, corresponding to the (311) reflection in Fe_3O_4, is related to the mean size of the crystals according to the Scherrer equation.[24] The Scherrer equation can be used to determine the average crystallite size of the Fe_3O_4 nanoparticles, and is given in Equation 4.4. It is based on the full width at half-maximum (FWHM) of the major diffraction peaks observed in the diffractogram,

$$D_P = \frac{k\lambda}{\beta \cos\theta} \qquad (4.4)$$

where D_p = the average size of the crystalline domains, which may be smaller or equal to the actual grain size

k = a dimensionless shape factor, with a value close to unity, *e.g.* 0.89

λ = the X-ray wavelength, for $\lambda_{Cu} = 1.5406$

β = the line broadening at half the maximum intensity (FWHM)

θ = the Bragg angle (position of maximum diffraction)

The average crystallite size of the pristine Fe_3O_4 nanoparticles as calculated from line broadening analysis using the Scherrer equation and was found to be 11.4 nm. It is important to note that the Scherrer formula provides a lower boundary of the particle size estimate of SPMNs. The reason for this is that the crystallite diameter estimated from XRD is statistically related to the volume weighted average particle size; as opposed to the number weighted value resulting from TEM measuremnts.[25] XRD hosts a variety of factors which can contribute to the width of a diffraction peak such as instrumental effects and crystallite size, the most important being inhomogeneous strain and crystal lattice imperfections.[26]

4.2.2 Magnetic Characterization

The magnetic properties of the synthesized pristine magnetite nanoparticles were analysed by a superconducting quantum interference device (SQUID). SQUID can be used to measure the saturation magnetization of the nanoparticles as well as to ascertain their superparamagnetic nature. Superparamagnetism occurs when the particle is small enough so that thermal fluctuations can overcome magnetic anisotropy.[27] The character of ideal superparamagnetic materials with the size less than the critical diameter of 20 nm is zero coercivity and zero remanence.[28] Figure 4.3 shows the magnetization curve of the pristine synthesized magnetite nanoparticles. The magnetization curve expresses the long moment or magnetization as a function of the applied magnetic field, as measured at room temperature (300 K).

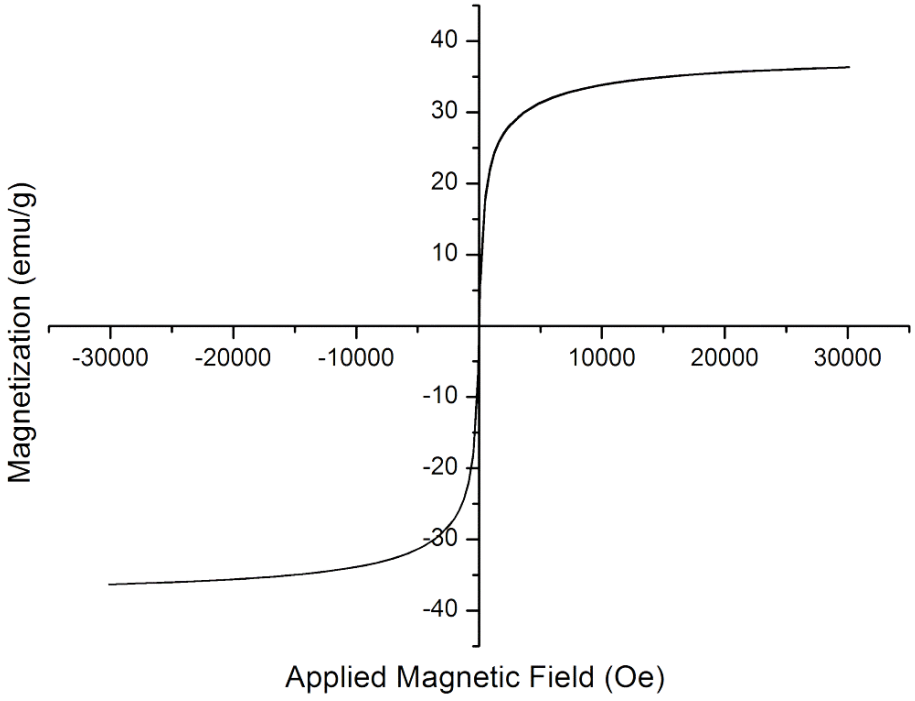

Figure 4.3 Magnetization curve of Fe_3O_4 nanoparticles demonstrating superparamagnetism.

According to the SQUID results, the synthesized pristine magnetite nanoparticles displayed superparamagnetic behaviour, showing zero coercivity and zero remanence above the blocking temperature. In effect, they did not retain any magnetism after removal of the magnetic field. High magnetization and superparamagnetic properties are vitally sought after for biomedical applications.[29]

Within an experimental context, superparamagnetism was observed when synthesizing Fe_3O_4 nanoparticles. This phenomenon is exemplified in Figure 4.4. When an external magnetic field was induced by placing a Teflon magnetic rod near the nanoparticles in dried or ferrofluid form, the nanoparticles were readily manipulated by the current. After the permanent magnet was removed, the nanoparticles were observed to lose all magnetization immediately. Each polymer coated SPMN nanocomposite exhibited this behaviour.

Figure 4.4 Superparamagnetism observed as Fe_3O_4 nanoparticles transform from the (a) unmagnetized state to the (b) and (c) magnetized states.

The diameter of the magnetic cores (D_m) can be calculated from data obtained during the magnetization measurements by assuming lognormal distribution. This was accomplished by using Equation 4.5,

$$D_m = \left(\frac{18kT}{\pi} \sqrt{\frac{\chi_i}{\rho M_s^2}} \right)^{\frac{1}{3}} \tag{4.5}$$

where, χ_i is the initial susceptibility $\chi_i = \left(\frac{dM}{dH}\right)_{H \to 0}$ and ρ is the density of magnetite (5.175 g.cm^{-1}). The initial gradient near the origin was determined from the magnetic plot by curve fitting the linear portion of the data. K is Boltzmann's constant and T is the temperature at which the magnetization data was obtained. The saturation magnetization of the uncoated superparamagnetic Fe_3O_4 nanoparticles is 36.3 emu/g at 300 K. The average diameter of the magnetic cores was therefore calculated as 10.7 nm.

The estimated core size determined from SQUID measurements as 10.7 nm is smaller than the crystallite size estimate from TEM (described in Section 4.2.3) and can be ascribed to magnetically dead layers which cannot be detected by magnetic measurements. Magnetically dead layers are caused by canted spins in the surface layers due to a decrease in the exchange coupling which is caused by the lack of oxygen mediating super exchange mechanism between the nearest iron ions at the surface, causing a non-magnetic layer.

The size obtained from magnetic measurements is smaller than TEM and XRD size measurements, which indicate the existence of magnetic cores and non-magnetic shells. These finite effects could account for the discrepancy between bulk phase magnetite (higher saturation magnetization) and nanoscale magnetite (lower saturation magnetization).[28,29]

Coated materials lead to a decrease in the effective magnetic moment. Due to the polymeric coating, the saturation magnetization is lower for coated nanoparticles than that of the bulk phase.[30] A decrease in the effective magnetic moment was observed for polymer coated SPMNs, yet superparamagnetic behaviour was still obeyed and these nanocomposites were readily manipulated by an external magnetic field. TMC coated SPMNs, as exemplar SPMN nanocomposite, was found to have a saturation magnetization of 22.7 emu/g (refer to Addendum A).

4.2.3 Transmission electron microscopy

Transmission electron microscopy (TEM) was used to determine the morphology, diameter and size distribution of the uncoated SPMNs and polymer coated SPMNs. Figure 4.5 presents TEM images of pristine SPMNs in different solvent environments. Three solvent dispersion conditions of Fe_3O_4 nanoparticles were analysed by TEM of which two are shown in Figure 4.5 (a) and (b).

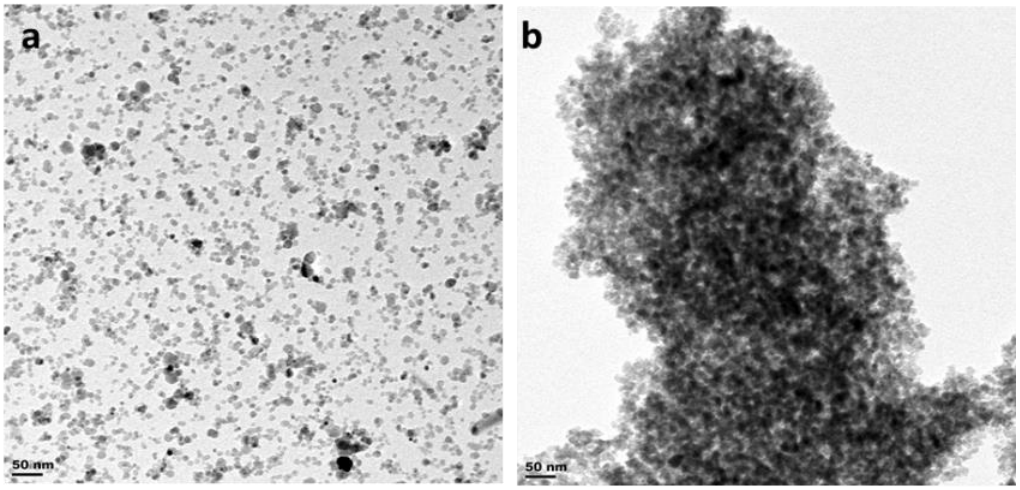

Figure 4.5 TEM images of uncoated SPMNs in (a) aqueous perchloric acid and (b) acetone.

Uncoated SPMNs have large surface area to volume ratios and possess high surface energies. They consequently tend to aggregate so as to minimize these surface energies. Moreover, SPMNs have high chemical activity and are easily oxidized in air, generally resulting in loss of magnetism and dispersibility.[31,32] Providing a proper surface coating in order to stabilize the SPMNs is therefore imperative. This can be done by peptization via acidification (adding charge), which can cause the surface properties of the nanoparticles to change, overcoming aggregation for a short time.

Figure 4.5 (a) is a TEM image of well dispersed, low surface energy SPMNs (uncoated) obtained via peptization of the nanoparticle solution by adding perchloric acid (1% v/v, 2 M). Figure 4.5 (b) is a TEM image of agglomerated, high surface energy SPMNs (uncoated) obtained via dispersing nanoparticles in acetone. For all subsequent transmission electron imaging of modified chitosan coated SPMNs, neutral pH Milli-Q water was used. Refer to Figures 4.6 and 4.7 for the representative TEM images and diameter distribution plots of pristine SPMNs (Fig. 4.6) and TMC SPMNs (Fig. 4.7). Refer to Addendum B for the TEM images and diameter distribution plots of HTCC SPMNs, CS-qC_8 SPMNs, CS-qC_{10} SPMNs and CS-qC_{12} SPMNs.

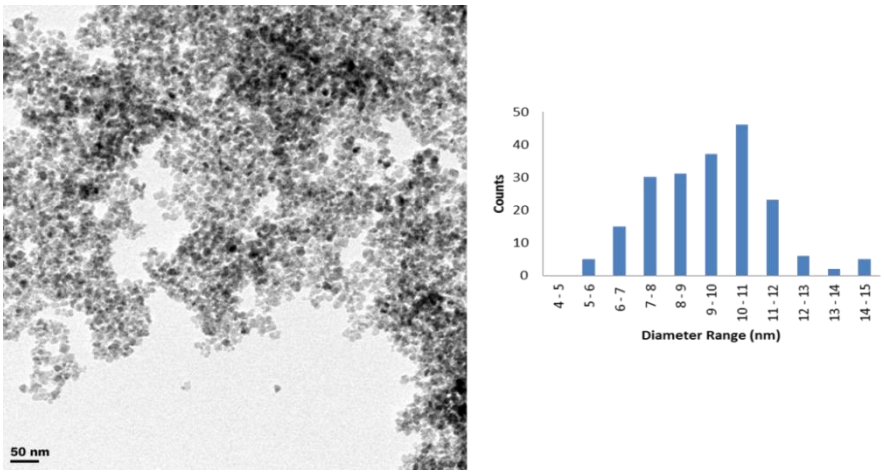

Figure 4.6 TEM image and size distribution histogram of pristine Fe_3O_4 nanoparticles.

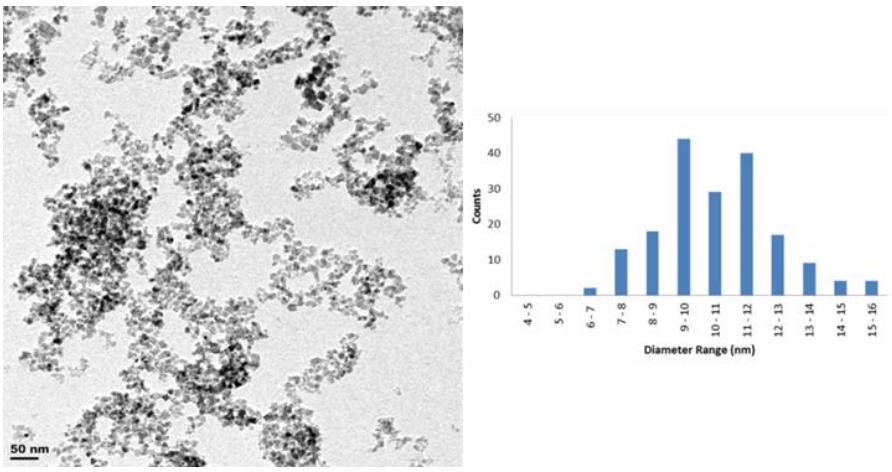

Figure 4.7 TEM image and size distribution histogram of TMC coated Fe_3O_4 nanoparticles.

Table 4.2 Summary of average diameter values and standard deviation values for pristine and polymer coated Fe_3O_4 nanoparticles

	Pristine SPMNs	*TMC SPMNs*	*HTCC SPMNs*	*CS-qC$_8$ SPMNs*	*CS-qC$_{10}$ SPMNs*	*CS-qC$_{12}$ SPMNs*
average diameter (nm)	11.8	10.77	8.11	10.31	8.87	7.54
standard deviation (nm)	2.31	2.07	1.82	2.03	2.15	1.77

Modified chitosan coated SPMNs are quasi-spherical in shape and have comparative size distributions when compared to pristine SPMNs. Chitosan has excellent properties for the adsorption of metal ions, principally due to the presence of amino groups in the polymer backbone, which can interact with metal ions in solution by ion exchange and complexation reactions.[33] Chitosan therefore forms an ultra-thin layer over the magnetite nanoparticles which cannot be directly observed via transmission electron microscopy. The polyelectrolyte property of chitosan stabilized the aqueous suspensions and limited the growth of magnetite during the nucleation stage of the *in situ* co-precipitation procedure, as confirmed by TEM analysis in light of smaller average diameter values for the polyelectrolyte coated SPMNs.

It is noted that the polymer coated nanoparticles display a less dense morphology than the uncoated nanoparticles. A time dependent aggregation study was conducted in order to determine the stability of the modified chitosan coated SPMNs over time. TEM analyses ensued over intervals of 0, 6 and 12 months in order to observe aggregation. The results of this time study are shown in Figure 4.8, and was done using TMC coated SPMNs in ferrofluid form stored in a refrigerator at 4 °C. No significant increase in aggregation is observed over a period of 12 months, as statistically comparable nanoparticle diameters were measured.

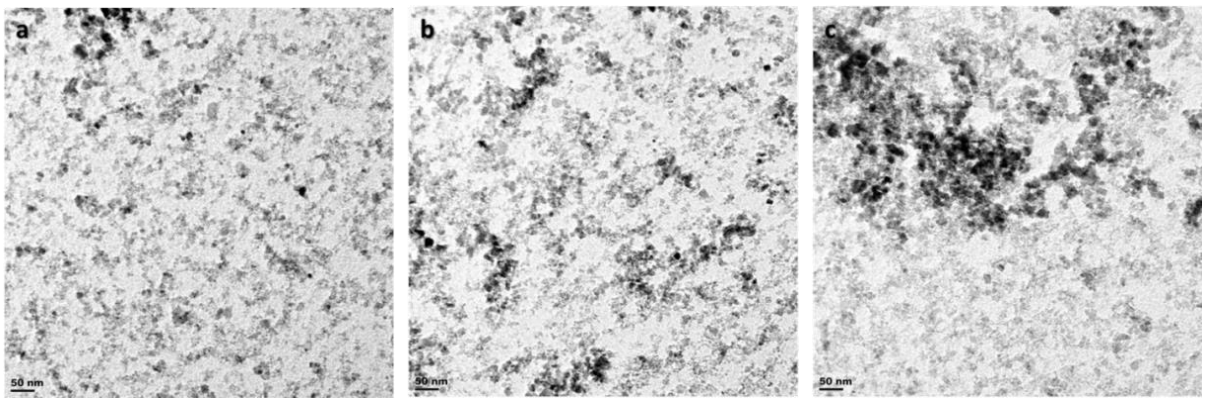

Figure 4.8 Aggregation studies using TEM over time of t = (a) 0 months, (b) 6 months and (c) 12 months.

4.2.4 Energy dispersive X-ray spectroscopy

Elemental composition analyses were performed in order to confirm the presence of major elements in the synthesized iron oxide nanoparticles and polymer coated nanocomposite materials. To achieve this, energy dispersive X-ray (EDX) spectroscopy was used as it is able to determine the elemental composition quantitatively. The presence of carbon, nitrogen and chlorine in the samples confirmed the modified chitosan polymer coating for the SPMNs, as the pristine SPMNs constituted iron and oxygen elements only.

Table 4.3 Table summarising elemental compositions of SPMNs and SPMN nanocomposites

	Carbon%	*Nitrogen%*	*Chlorine%*	*Iron%*	*Oxygen%*
Pristine SPMNs	-	-	-	77.73	22.27
TMC SPMNs	5.72	1.48	1.11	56.12	35.56
HTCC SPMNs	3.15	0.97	1.16	64.97	29.76
CS-qC$_8$ SPMNs	15.83	0.41	0.21	31.26	52.29
CS-qC$_{10}$ SPMNs	11.37	1.79	0.12	39.87	46.84
CS-qC$_{10}$ SPMNs	17.78	0.26	0.20	26.14	55.62

4.2.5 Thermogravimetric analysis

To confirm the presence of the modified chitosan coating and to determine the percentage content of the polymeric coating around the SPMN core, thermogravimetric analysis (TGA) was performed. Figure 4.9 depicts the TGA curves of pristine SPMNs and modified chitosan coated SPMNs. The observed behaviour is consistent to that which is reported in literature, and aided characterization.[4, 34-36]

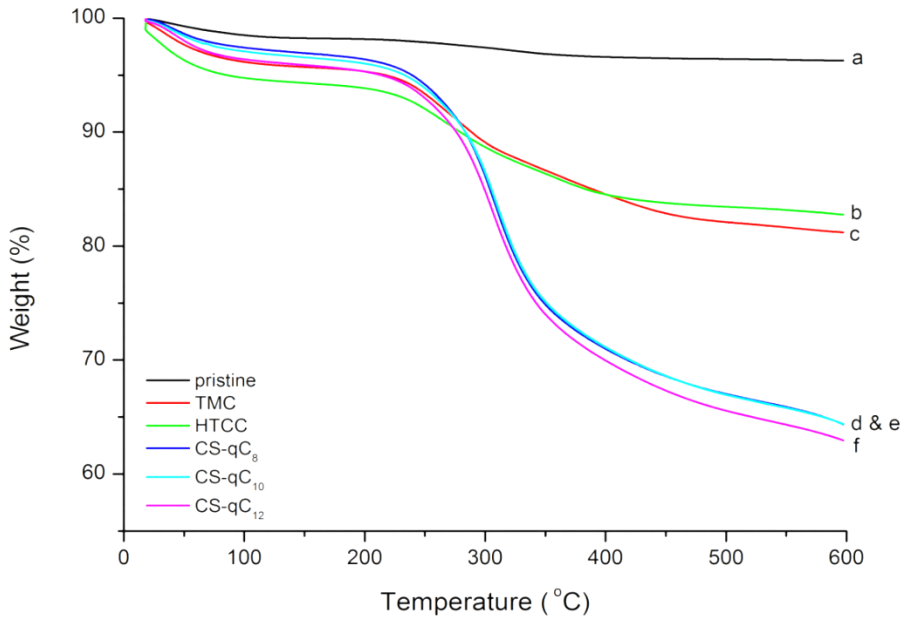

Figure 4.9 TGA curves of (a) pristine SPMNs, (b) HTCC coated SPMNs, (c) TMC coated SPMNs, (d) CS-qC$_8$ coated SPMNs, (e) CS-qC$_{10}$ coated SPMNs and (f) CS-qC$_{12}$ coated SPMNs.

The first derivative weight loss curves of the modified chitosan SPMNs were also plotted in order to provide a clear indication of the temperature range and magnitude of loss during specific degradation steps, the results of which are presented in Figure 4.10.

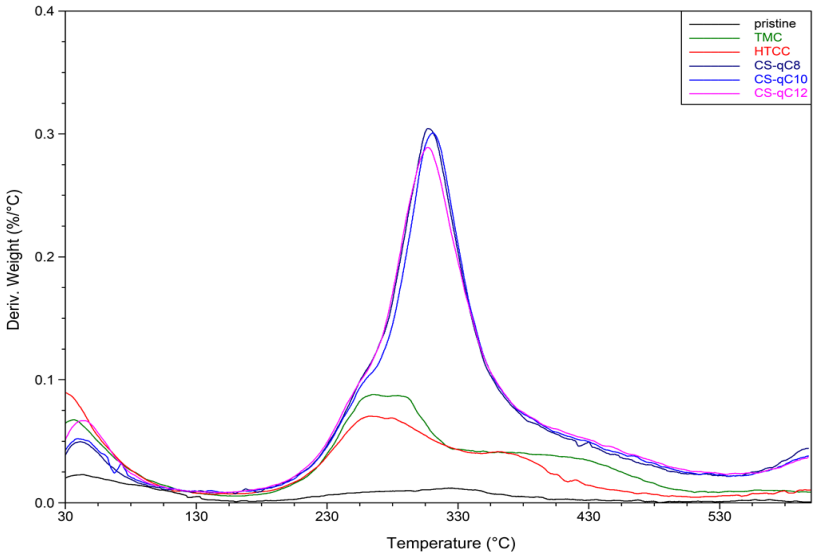

Figure 4.10 TGA first derivative weight loss curves of pristine SPMNs and modified chitosan coated SPMNs.

As can be seen from Figure 4.9 and 4.10, modified chitosan SPMNs showed residue losses over two stages under heating in an inert atmosphere. The first weight loss stage spanned over 30 °C to 200 °C and consisted of a 5 – 10% loss of weight, which related to the loss of adsorbed water from the structure of the biopolymer itself and surface hydroxyls; or in the case of pristine SPMNs,

surface hydroxyls and water loss. The second stage of weight loss started at 200 °C and continued up to 600 °C and can be attributed to the release of volatiles, oxidative decomposition and subsequent disintegration of the coating layer. The percentage residue left in the TGA curves for modified chitosan is due to the two constituting residues of the biopolymer after rupture of the β-glycosidic linkages.

The loss of weight as the temperature increases from room temperature to 120°C is attributed to residual water left in the samples. Minor loss is incurred for the pristine SPMNs over the temperature range of 120 °C to 600 °C (2.1%). For the modified chitosan coated SPMNs, the major loss from 120 °C to 600 °C is therefore due to the modified chitosan component on the nanoparticle surface. The modified chitosan polymer content could therefore be calculated over the temperature range of 120 °C to 600 °C, according to Equation 4.6:

$$\textit{Coating content (\%)} = W_C\,(\%) - W_U\,(\%) \qquad (4.6)$$

where W_C (%) is the percentage weight lost by the modified chitosan coated Fe_3O_4 nanoparticles and W_U (%) is the percentage weight lost by the uncoated Fe_3O_4 nanoparticles.

Table 4.4 Summary of percentage coating of the modified chitosan nanocomposites

	TMC SPMNs	*HTCC SPMNs*	*qCS-C_8 SMNPs*	*qCS-C_{10} SPMNs*	*qCS-C_{12} SPMNs*
% Coating	12.7	9.73	30.8	30.4	31.2

From the results presented in the table, it is clear that the CS-q$C_{8,}$ CS-qC_{10} and CS-qC_{12} SPMNs have similar percentage coatings; higher than that of TMC SPMNs and HTCC SPMNs. The size of the polymer, its structure and therefore the packing density, ionic strength, degree of quaternization and hydrophobicity could all play a role in this observance.

The quaternized carbon-8, 10 and 12 polymer coated SPMNs also have higher temperatures of polymer degradation resulting in polymers nanocomposites with greater thermal stability when compared to TMC SPMNs and HTCC SPMNs. This could be explained by the research of Zhou *et. al*., in that chitosan backbones were able to restrict the mobility of side alkyl chains, thus postponing the melting process of CH_2 units in the aliphatic chains which resulted in the locally ordered packing of methylene segments at the nanoscale level.[37] TGA results are in good agreement with the EDX results, where greater percentages of carbon were recorded for the polymer coated SPMNs with greater percentage polymer coating found by TGA analysis.

4.2.6 Fourier-transform infrared spectroscopy

Fourier transform infrared (FTIR) spectra were acquired to confirm the presence of quaternized chitosan polymer around the superparamagnetic magnetite nanoparticles. As all modifications of chitosan displayed the same trend in terms of FTIR spectra, TMC was selected as the representative polymer and for this subsection will be referred to simply as modified chitosan. Figure 4.11 shows the representative IR spectra of (a) modified chitosan in red, (b) modified chitosan coated SPMNs in black and (c) pristine (uncoated) SPMNs in green. The FTIR spectra stand to prove that modified chitosan was functionalized onto the SPMN core. A detailed summary of the FTIR spectra of chitosan and its derivatives was presented and discussed in Chapter 3.

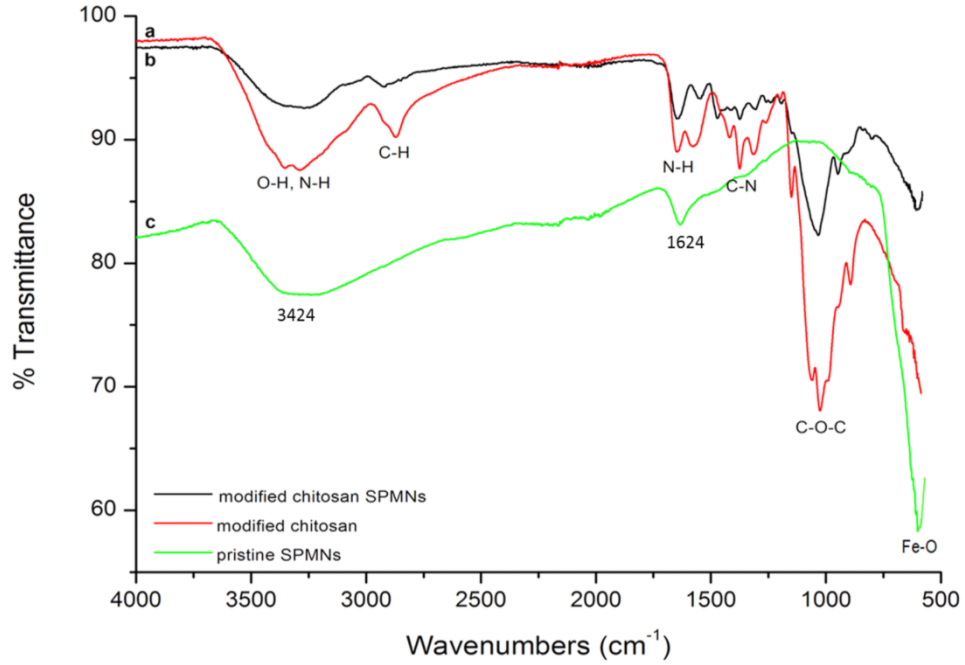

Figure 4.11 Superimposed FTIR spectra of (a) modified chitosan, (b) modified chitosan coated SPMNs and (c) pristine SPMNs.

Pristine magnetite has few functional groups. There is a characteristic peak located around 600 cm^{-1} and can be attributed to the vibrations of the Fe-O bond of magnetite. These characteristic bands are found in the spectra of both modified and unmodified magnetite nanoparticles.[38] Furthermore, two bands around 3424 cm^{-1} and 1624 cm^{-1} can be ascribed to the stretching and bending vibrations of surface hydroxyl groups, respectively.[39]

Abundant characteristic absorption peaks of modified chitosan can be seen in the spectrum of the modified chitosan coated nanoparticles. The characteristic band in the 2850 – 3040 cm^{-1} frequency region originates from the asymmetric and symmetric stretching modes of the C-H group, further confirming the successful coating of magnetite nanoparticles.[40] The bands at 1100 – 1030 cm^{-1} assigned to the C-O stretch vibrations of the secondary alcohol groups in the modified chitosan

SPMNs maintain their position but show a marked decrease in intensity, following the reaction of modified chitosan with the Fe_3O_4 core. A similar decrease is observed in the region above 3000 cm^{-1}. It was postulated by Hernández *et al.* that this decrease may be due to coordination of the hydroxyl neighbour of the amine group in position 3 of the biopolymer unit.[34]

4.2.7 Surface area and porosity analysis

The specific surface area and porosity of the uncoated SPMNs and the modified chitosan coated SPMNs were measured by Brunauer–Emmett–Teller (BET) analysis, the results of which are summarised in Table 4.5.

Table 4.5 Surface area and porosity analysis

	Specific Surface Area *(m^2/g)*	*Pore Volume* *(cm^3/g)*	*Pore Diameter* *(Å)*
Pristine SPMNs	505.2	0.133	10.55
TMC SPMNs	680.2	0.171	10.10
HTCC SPMNs	802.3	0.212	10.59
CS-qC_8 SPMNs	613.5	0.157	10.29
CS-qC_{10} SPMNs	424.9	0.105	9.96
CS-qC_{12} SPMNs	428.4	0.099	9.25

The surface of iron oxides such as SPMNs (Fe_3O_4) has structural sites which are able to interact with gas and soluble species. The specific surface area of a solid is defined as the surface area of a unit mass of material, usually expressed as m^2/g. Applying the BET method, adsorption isotherms were obtained by measuring the amount of nitrogen gas that adsorbed at the boiling point of liquid N_2 (-77 K) on out-gassed SPMNs and SPMN nanocomposites as a function of relative pressure.

Nanoparticles present a higher surface to volume ratio with decreasing size of nanoparticles. Specific surface area is relevant for catalytic reactivity; as the specific surface area of nanoparticles is increased, biological efficacy can increase due to the increase in surface energy. Owing to the

nanometric dimensions, SPMNs had very large specific surface areas. The chitosan based SPMNs have corresponding average pore sizes, which allow for the classification of these compounds into the mesoporous structure group (pore size 2 – 50 Å).[42-43]

4.3 Conclusion

Superparamagnetic magnetite nanoparticles (SPMNs) and modified chitosan coated SPMN nanocomposites were successfully synthesized via the co-precipitation technique. No aggregation of the polymer coated magnetic nanoparticles into micron-sized clusters was detected over a time period of 12 months, indicating stability. Various characterization techniques were used to confirm the phase purity, size and morphology of the SPMNs as well as the presence of the various polymeric coatings onto SPMN cores. Physical characteristics were analysed by surface area and porosity studies and thermal analyses were conducted in order to quantify the percentage polymer coating of the SPMN nanocomposites.

The crystallite size obtained from XRD analysis was calculated to be 11.4 nm, and is comparable to those measured via TEM, averaging 11.8 nm. The average crystallite core size estimated from magnetization measurements as 10.7 nm was smaller than that estimated from TEM measurements. This could be attributed to the phenomenon of magnetically dead layers which form around crystallite spheres, of which SQUID and other magnetization characterization techniques are not able to detect. FTIR, TGA and EDX measurements confirmed the presence of the modified chitosan polymeric coating of the SPMN nanocomposites, of which the syntheses are described in the experimental section of this chapter.

4.4 Experimental

4.4.1 Materials

High purity deionized water (Milli-Q, 18.2 MΩ cm) was deoxygenated by bubbling with pure N_2 gas for 45 min prior to use. *N*-trimethylammonium chitosan chloride (TMC), *N*-(2-hydroxy)propyl-3-trimethylammonium chitosan chloride (HTCC), *N*-propyl-3-*N',N'*-dimethyl-*N'*-octylammonium chitosan chloride (CS-qC_8), *N*-propyl-3-*N',N'*-dimethyl-*N'*-decylammonium chitosan chloride (CS-qC_{10}) and *N*-propyl-3-*N',N'*-dimethyl-*N'*-dodecylammonium chitosan chloride (CS-qC_{12}) were synthesized as outlined in Chapter 3. The following chemicals were utilized in this part of the project: Iron (III) chloride hexahydrate (98%, Sigma-Aldrich), Iron(II) chloride (97%, Sigma-Aldrich), ammonia water (25% in H_2O, Merck), acetone (Sigma-Aldrich, 99.5%) and ethanol (Sigma-Aldrich, 99.5%).

4.4.2 Characterization Techniques

a) Powder X-ray diffraction (P-XRD)

The structural properties of pristine SPMN powder were investigated by XRD using a Siemens D8 Advance diffractometer using Cu K_α radiation (λ = 1.540 Å) operated at 40 kN and 30 mA. XRD patterns were recorded in the range 10 - 80° (2θ) with a scan step of 0.015°. The average crystallite size (<D>, Å) was calculated from line broadening analysis using the Scherrer formula.[43] For sample preparation, a portion of SPMNs was allowed to dry completely under vacuum at room temperature before analysis. Sample preparation plays an integral role in diffractogram quality so care was taken in milling the nanoparticles and ensuring uniform packing in the sample holder. The obtained spectrum was corrected for instrumental line broadening and refined with the XRD analysis program, EVA.[44]

b) Superconducting quantum interference device (SQUID)

A SQUID magnetometer was used in order to determine the magnetic nature of pristine SPMNs. The SQUID magnetometer (7 Tesla Magnet) analysis was performed using a reciprocal sample option. The resolution reached 10^{-7} electromagnetic units (emu). The liquid SPMN sample (50 mg of 50 mmol L^{-1}) was embedded in specific drop-shaped vitreous cuvettes with a 5 mm diameter and 15 mm length. Hysteresis curves were monitored at 300 K fixed temperature and a field strength of -10 to +10 kOe. All measurements were performed in a parallel magnetic field in the longitudinal direction to the cuvette to minimize the background of the diamagnetic part of the cuvette. Based on the signal intensity of the magnetization (emu), the specific magnetization was calculated in emu/g iron using the exact net weight.

c) Transmission electron microscopy (TEM)

Particle size and morphology was determined by TEM, using a JEM 1200EXII model (JEOL, Japan) microscope. In general, an accelerated voltage of 120 kV was used throughout. All samples were dried in a vacuum oven at 60°C for 24 h and milled to obtain fine dry powders. A small amount of dried sample (1 mg) was dispersed in distilled, deionized water and sonicated for 10 min. Afterwards, a drop thereof was placed on a carbon-coated 200 mesh copper grid, followed by drying at ambient conditions before it was attached to the sample holder on the microscope. The mean diameter and size-distribution was determined by measuring more than 100 particles from TEM images using *SEM IMAGE STUDIO,* a public domain image processing program.[44]

d) Elemental composition analysis

Phase compositions were quantified using a Leo® 1430VP Scanning Electron Microscope (SEM) equipped with an Oxford Instruments® 133 KeV detector and Oxford INCA software. With the attachment of an energy dispersive X-ray spectrometer (EDS), the chemical or elemental composition of the materials was obtained. The samples were mounted on a small stub with double sided carbon tape. The sample mounted on the stub was then coated with a thin layer of gold and mounted on the SEM stage in a chamber under high vacuum. The beam conditions during the quantitative analyses were 20 kV and approximately 1.5 nA, with a working distance of 13 mm and a specimen beam current of -3.92 nA.

e) Thermogravimetric analysis (TGA)

TGA was performed using a Q500 TA instrument in the temperature range of 0 - 590 °C, using Pt crucibles with typically 5 mg dried samples, under dynamic N_2 atmosphere (50 mL/min) and a heating rate of 10 °C min^{-1}. Samples were weighed in a sample component that was dried and flushed with nitrogen gas.

f) Attenuated total reflectance Fourier transform infrared (ATR-FTIR) spectroscopy

Attenuated total reflectance Fourier transform infrared (ATR-FTIR) spectra were collected using a Nicolet FTIR spectrometer (model Nexus) from Thermo-Fischer equipped with a Smart Golden gate ATR accessory with a diamond internal reflection crystal. The spectra were recorded from 4000 cm^{-1} to 600 cm^{-1} with a spectral resolution of 4 cm^{-1} and were the sum of 64 individual scans. No sample preparation was necessary and samples were in solid state. Omnic software was used for data acquisition and processing.

g) Surface Area Measurements

The specific surface area (SSA) of pristine SPMNs and modified SPMN samples was determined by the Brunauer, Emmett and Teller (BET) method, with a Micrometrics ASAP 2010 (Accelerated Surface Area and Porosity System) using nitrogen as an adsorbent.[46,47] The samples were activated by degassing under vacuum at 300 °C for 24 h. Each degassed sample (100 – 200 mg) was weighed accurately to four decimal places and placed in a sample tube. Analysis was performed using an automatic multi-point adsorption programme, measuring the volume of nitrogen adsorbed by the sample at a range of N_2 pressures.

4.4.3 Experimental Procedures

a) Synthesis of SPMNs

The synthesis of pristine SPMNs was based on the classical co-precipitation reaction of ferrous and ferric chloride developed by Massart, and modified accordingly based on the research outlined during the introduction of this chapter.[5] Figure 4.12 shows the SPMN reaction vessel before and after ammonia water addition. The dark orange aqueous solutions of ferrous and ferric chloride react to form black colloidal SPMNs.

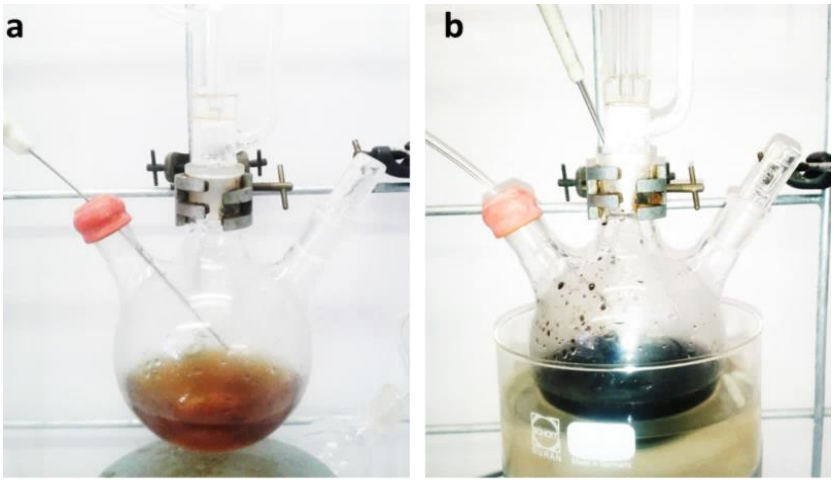

$$Fe^{2+} + Fe^{3+} + 8OH^- \rightarrow Fe_3O_4 + 4H_2O$$

Figure 4.12 Digital images displaying SPMN reaction vessel (a) before and (b) after addition of the base.

In a dropping funnel attached to a three-necked reaction flask, a 0.5% (v/v) aqueous acetic acid solution (100 mL) was bubbled with N_2 gas for 30 min. This was added to iron(III) chloride hexahydrate (1 g, 3.7 mmol) and iron(II) chloride (0.235 g, 1.85 mmol) at 80 °C to obtain a pale brown solution. From another dropping funnel, ammonia water (25%, 17.4 mL), which had been previously deoxygenated, was added rapidly to the reaction vessel with vigorous stirring and under an inert gas atmosphere. An instant black precipitate was observed, indicating the formation of magnetite nanoparticles. The reaction vessel was then irradiated with ultrasonic (>20 kHz) waves for 15 min. Iron oxides must be washed after preparation to remove impurity ions associated with the procedure; in this case the OH^- ions must be removed. The black precipitated powder was readily isolated by applying an external magnetic field (0.35 T), and the supernatant was removed from the precipitate via magnetic decantation. The isolated precipitate was washed at least four times with deoxygenated Milli-Q water. The washed black precipitate could be altered to ferrofluid form by the addition of deoxygenated Milli-Q water (60 mL) at a pH of 2.0 by the addition of lactic acid and D-mannitol (3 g). The SPMNs were otherwise dried in a vacuum oven at room temperature for 24 h.

b) Synthesis of modified chitosan coated SPMNs

In an acidic environment, the free amino groups of chitosan become positively charged after protonation and quaternized chitosan has a permanently charged ammonium ion group. They are therefore able to interact with negatively charged molecules, such as the hydroxyl (Fe-OH) groups on the surface of magnetite nanoparticles.

Ferrous and ferric ions are chelated by the amino groups of chitosan and derivatives and provide a nucleation site for magnetite crystal growth under specific conditions. The crystal growth of magnetite is restricted by the iron ions diffusion, which in turn, is restricted by the chelation effect. The hydrophilic Fe_3O_4 cores precipitate by forming nuclei with high surface energies and rapidly adsorb well-dissolved chitosan and derivative polymers, respectively. In view of these reasons, uniform layers of modified chitosan polymer chains may be assembled by electrostatic interaction on Fe_3O_4 cores to stabilize each individual nanoparticle, enabling narrow size distributions and small diameters.[13,48] A general schematic representation of the interaction is presented in Figure 4.13.

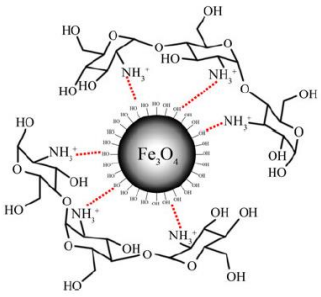

Figure 4.13 Electrostatic interaction between chitosan and magnetite magnetic core.

The coating of the SPMNs was achieved via a chemical co-precipitation *in situ* coating procedure based upon an adapted procedure described by Shen *et al*.[49] The modified chitosan polymers refer to TMC, HTCC, CS-$qC_{8,}$ CS-qC_{10} and CS-$qC_{12.}$

In separate synthesis procedures, the modified chitosan polymer (2.17 mmol) was dissolved in a deoxygenated solution of aqueous acetic acid (0.5% v/v, 100 mL). To this solution, and under an inert gas atmosphere, iron(III) chloride hexahydrate (1 g, 3.7 mmol) and iron(II) chloride (0.235 g, 1.85 mmol) were added to obtain a viscous, pale brown solution. Then, a solution of deoxygenated ammonia water (25%, 7.4 mL) was rapidly added to the solution under vigorous stirring at 80 °C. The reaction vessel was then irradiated with ultrasonic (>20 kHz) waves for 30 min. The black precipitate was isolated with a permanent magnet via magnetic decantation and the precipitate was washed with 95% ethanol at least four times. This *in situ* coating procedure produced TMC coated SPMNs, HTCC coated SPMNs, CS-qC_8 coated SPMNs, CS-qC_{10} coated SPMNs and

CS-qC_{12} coated SPMNs, respectively. The washed black precipitate could be altered to ferrofluid form by the addition of deoxygenated Milli-Q water (60 mL) and adjustment of the pH to 7.0 by the addition of lactic acid and D-mannitol (3 g). The modified chitosan coated SPMNs were otherwise dried under vacuum at room temperature for 24 h.

c) Crosslinked polymer coated SPMNs

Crosslinked, modified chitosan coated SPMNs were synthesized via the procedure described in Section 4.4.3(b) but with the addition of glutaraldehyde (3 mL, 50% in water), after nanoparticle formation. The solution was then left to stir rapidly for 8 h, whereafter the black precipitate was isolated via magnetic decantation and washed twice with ethanol and twice with water, respectively. The washed black precipitate could be affected to ferrofluid form by the addition of deoxygenated Milli-Q water (60 mL) and adjustment of the pH to 7.0 by the addition of lactic acid and D-mannitol (3 g). The modified chitosan coated SPMNs were otherwise dried under vacuum at room temperature for 24 h.

4.4.4 Storage and drying of SPMNs

Vacuum oven drying at 40 °C for 24 h is the most convenient method to dry the synthesized SPMNs. A temperature of 40 °C is low enough to avoid any phase modification or transformation. After drying, the sample is ground in an agate mortar to break up any aggregates. Iron oxides are most conveniently stored as dry powders. If stability over long periods of time (years) is required, then the SPMNs may be affected to ferrofluid form directly after synthesis.[50]

4.5 References

1. Zhang, Q.; Liu, S.; Yu, S. *J. Mater. Chem.* **2009**, *2,* 191-207.
2. Nguyen, T.; Do, T. INTECH. **2011**.
3. Park, J.; Lee, E.; Hwang, N.; Kang, M.; Kim, S. C.; Hwang, Y.; Park, J.; Noh, H.; Kim, J.; Park, J. *Angew. Chem. Int. Edit.* **2005**, *19,* 2932-2937.
4. Faraji, M.; Yamini, Y.; Rezaee, M. *J. Iranian Chem. Soc.* **2010**, *1,* 1-37.
5. Szpak, A.; Kania, G.; Skórka, T.; Tokarz, W.; Zapotoczny, S.; Nowakowska, M. *J. Nanopart. Res.* **2013**, *1,* 1-11.
6. Massart, R. *IEEE Trans. Magn.* **1981**, 1247-1248.
7. Mahmoudi, M.; Sant, S.; Wang, B.; Laurent, S.; Sen, T. *Adv. Drug Deliv. Rev.* **2011**, *1,* 24-46.
8. Gupta, A. K.; Curtis, A. S. *Biomaterials* **2004**, *15,* 3029-3040.
9. Kim, D.; Zhang, Y.; Voit, W.; Rao, K.; Muhammed, M. *J. Magn. Magn. Mater.* **2001**, *1,* 30-36.

10. Yamaura, M.; Camilo, R.; Sampaio, L.; Macedo, M.; Nakamura, M.; Toma, H. *J. Magn. Magn. Mater.* **2004***, 2,* 210-217.

11. Wang, N.; Zhu, L.; Wang, D.; Wang, M.; Lin, Z.; Tang, H. *Ultrason. Sonochem.* **2010***, 3,* 526-533.

12. Shen, L.; Laibinis, P. E.; Hatton, T. A. *Langmuir* **1999***, 2,* 447-453.

13. Massart, R.; Dubois, E.; Cabuil, V.; Hasmonay, E. *J. Magn. Magn. Mater.* **1995***, 1,* 1-5.

14. Unsoy, G.; Yalcin, S.; Khodadust, R.; Gunduz, G.; Gunduz, U. *J. Nanopart. Res.* **2012***, 11,* 1-1

15. Muthiah, M.; Park, I.; Cho, C. *Biotechnol. Adv.* **2013***, 8,* 1224-1236.

16. Bhattacharya, D.; Sahu, S. K.; Banerjee, I.; Das, M.; Mishra, D.; Maiti, T. K.; Pramanik, P. *J. Nanopart. Res.* **2011***, 9,* 4173-4188.

17. Agrawal, P.; Strijkers, G. J.; Nicolay, K. *Adv. Drug Deliv. Rev.* **2010***, 1,* 42-58.

18. Mahmoudi, M.; Simchi, A.; Milani, A.; Stroeve, P. *J. Coll. Interface Sci.* **2009***, 2,* 510-518.

19. Hejazi, R.; Amiji, M. *Acs. Sym. Syr.* **2001**, 213-237.

20. Qu, H.; Caruntu, D.; Liu, H.; O'Connor, C. J. *Langmuir* **2011***, 6,* 2271-2278.

21. Thanou, M.; Verhoef, J.; Junginger, H. *Adv. Drug Deliv. Rev.* **2001**, S91-S101.

22. Zhang, Z.; Su, F.; Wen, F. *Coll. Polym. Sci.* **2008***, 286,* 837.

23. Legodi, M.; De Waal, D. *Dyes Pigments* **2007***, 1,* 161-168.

24. Cornell, R. M.; Schwertmann, U. *The iron oxides: structure, properties, reactions, occurrences and uses*; John Wiley & Sons, **2006**.

25. Kim, D.; Zhang, Y.; Voit, W.; Rao, K.; Muhammed, M. *J. Magn. Magn. Mater.* **2001***, 1,* 30-36.

26. Dodi, G.; Hritcu, D.; Draganescu, D.; Popa, M. I. *J. Magn. Magn. Mater.* **2015**, 49-58.

27. Verma, S.; Singh, D.; Pandey, D.; Yadav, R. *Nat. Acad. Sci. Lett.* **2013***, 5,* 535-540.

28. Tannenbaum, R.; King, S.; Lecy, J.; Tirrell, M.; Potts, L. *Langmuir* **2004***, 11,* 4507-4514.

29. Ozkaya, T.; Toprak, M. S.; Baykal, A.; Kavas, H.; Köseoğlu, Y.; Aktaş, B. *J. Alloys Comp.* **2009***, 1,* 18-23.

30. Zhu, A.; Yuan, L.; Liao, T. *Int. J. Pharm.* **2008***, 1,* 361-368.

31. Li, G.; Jiang, Y.; Huang, K.; Ding, P.; Chen, J. *J. Alloys Comp.* **2008***, 1,* 451-456.

32. Dorniani, D.; Hussein, M. Z. B.; Kura, A. U.; Fakurazi, S.; Shaari, A. H.; Ahmad, Z. *Int. J. Nanomed.* **2012**, 5745.

33. Wu, W.; He, Q.; Jiang, C. *ChemInform* **2009***, 24,* i.

34. Tran, H. V.; Dai Tran, L.; Nguyen, T. N. *Mater. Sci. Eng. C* **2010***, 2,* 304-310.

35. Zhang, L.; Zhu, X.; Sun, H.; Chi, G.; Xu, J.; Sun, Y. *Curr. Appl. Phys.* **2010***, 3,* 828-833..

36. Castelló, J.; Gallardo, M.; Busquets, M. A.; Estelrich, J. *Colloids Surf. Physicochem. Eng. Aspects* **2015**, 151-158.

37. Hernández, R. B.; Franco, A. P.; Yola, O. R.; López-Delgado, A.; Felcman, J.; Recio, M. A. L.; Mercê, A. L. R. *J. Mol. Struct.* **2008***, 1,* 89-99.

38. Zhou, Y.; Shi, H.; Zhao, Y.; Men, Y.; Jiang, S.; Rottstegge, J.; Wang, D. *CrystEngComm* **2011***, 2,* 561-567.

39. Yang, K.; Peng, H.; Wen, Y.; Li, N. *Appl. Surf. Sci.* **2010***, 10,* 3093-3097.

40. Mikhlin, Y. L.; Kuklinskiy, A.; Pavlenko, N.; Varnek, V.; Asanov, I.; Okotrub, A.; Selyutin, G.; Solovyev, L. *Geochim. Cosmochim. Acta* **2002***, 23,* 4057-4067.

41. Barrett, E. P.; Joyner, L. G.; Halenda, P. P. *J. Am. Chem. Soc.* **1951***, 1,* 373-380.

42. Song, J. Y.; Kim, B. S. *Bioproc. Biosyst. Eng.* **2009***, 1,* 79-84.

43. Kim, T.; Shima, M. *J. Appl. Phys.* **2007***, 9,* M516.

44. Klug, H. P.; Alexander, L. E. *X-Ray Diffraction Procedures for Polycrystalline and Amorphous materials;* Wiley: New York, **1974**.

45. Guibal, E.; M. Ruiz, T.; Vincent, A. Sastre, R. Navarro-mendoza, *Separ. Sci. Technol.* **2001,** *36,* 1017.

46. Rasband, W. *In Image J*: Image processing and analysis in java *http://rsb.info.nih.gov/ij/*, **2006**.

47. Lowell, S.; Shields, J. E. *Springer* **2013**, *2*.

48. Webb, P. A.; Orr, C. *Analytical methods in fine particle technology;* Micromeritics Instrument Corp, **1997**.

49. Shen, C.; Juang, J.; Tsai, Z.; Wu, S.; Tsai, F.; Wang, J.; Liu, C.; Yen, T. *Carbohydr. Polym.* **2011***, 2,* 781-787.

50. Schwertmann, U.; Cornell, R. M. *Iron oxides in the laboratory*; John Wiley & Sons, **2008**.

Chapter Five

Chitosan based Bi-component Nanofibers

5.1 Introduction

Electrospinning has been recognized as an efficient technique for the fabrication of polymer nanofibers. Despite the simplicity of the electrospinning setup, the actual mechanism of nanofiber formation is rather complex.[1] The electrospinning process is affected by solution properties such as the type and conformation of the polymer, viscosity, electrical conductivity and surface tension as well as operating conditions which include the applied voltage, the tip to collector plate distance and the feed rate of the polymer.[2]

It is widely reported that the electrospinning of chitosan and specifically, its quaternized derivatives is problematic due to their polycationic nature, rigid chemical structure and ability to form specific inter- and intramolecular interactions. The formation of hydrogen bonds prevents the free movement of the polymeric chains exposed to the electrical field, leading to jet break up during the process. Moreover, great repulsive forces exist between the ionic groups within the polymer backbone of quaternized chitosan polymers. These forces restrict the formation of smooth, continuous nanofibers during the jet stretching, whipping and bending phase. The high charge density along the polymer backbone creates unfavourable polymer-polymer and polymer-solvent interactions, thus producing an imbalance between the viscosity and surface tension required for nanofiber formation.[3-8]

The addition of a suitable non-ionogenic polymer partner with a flexible chain in the electrospinning solution of quaternized chitosan has been known to ease the charges along the polymer backbone, producing smooth, continuous nanofibers. The enhancement of material properties such as tensile strength and rheology is also reported in literature.[9] Suitable non-ionogenic polymers for blending with chitosan derivatives include polyvinyl alcohol (PVA),[10] polyethylene oxide (PEO),[11] polyacrylamide (PAM)[12] and polyvinyl pyrrolidone (PVP),[13] as presented in Figure 5.1.

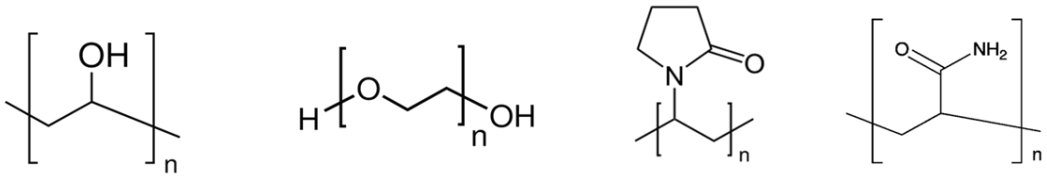

PVA PEO PVP PAM

Figure 5.1 Non-ionogenic polymers.

The strategic importance of analyzing different non-ionogenic polymers blended with modified chitosan and electrospun into bi-component nanofibers, is to determine which polymer is able to most efficiently interact with modified chitosan to facilitate the greatest cellular interaction and adhesion to mycobacteria.

5.1.1 Non-ionogenic polymers

a) Polyvinyl alcohol

PVA is a water-soluble, semi-crystalline, fully biodegradable, non-toxic, and biocompatible polymer which therefore finds use in a broad spectrum of applications. It is inherently hydrophilic and has desirable physical properties such as its rubbery or elastic nature and high degree of swelling in aqueous solutions. PVA has a flexible, linear chain and is able to impart mechanical stability and flexibility to natural polymers such as chitosan.[14-16]

b) Polyethylene oxide

PEO is a biocompatible, hydrophilic, water-soluble polymer and is one of the few synthetic polymers approved for internal use in food, cosmetics, personal care products and pharmaceuticals. PEO has a linear structure with flexible chains, and is able to form hydrogen bonds with other macromolecules such as chitosan. Within a chitosan blend, PEO acts as a plasticizer facilitating orientation and flow of chitosan by uncoiling and wrapping around chitosan chains.[17-19]

c) Polyvinyl pyrrolidone

PVP has found a wide variety of applications in the biomedical field due to properties which include non-toxicity, high hydrophilicity, biocompatibility, good complexation properties and film-forming ability. PVP exhibits stronger polymer–solvent interactions compared to polymer–polymer attraction forces, so the polymer chains are able to absorb solvent molecules rapidly, increasing the volume of the polymer matrix and allowing the polymer chains to readily loosen from their coiled shape.[20,21]

d) Polyacrylamide

Through the highly reactive amide (NH_2) group, PAM can be chemically modified to be a cationic or anionic polymer. It is a hydrophilic polymer, able to form aqueous solutions of very high concentrations and is most often used to increase the viscosity of water or to encourage flocculation of suspended particles present in water. In flocculation, polymer chains adsorb onto particle surfaces to form bridges between one or more adjacent particles.[22]

5.2 Results and Discussion

The aim of this study was to electrospin the quaternized derivative of chitosan, *N*-trimethylammonium chitosan chloride (TMC) into nanofibers by blending the polymer with suitable non-ionogenic polymer partners, followed by crosslinking of the nanofibers to render aqueous stability.

5.2.1 Electrospinning TMC/non-ionogenic polymer bi-component nanofibers

As described in the literature chapter, many parameters influence polymer jet stability during electrospinning. The variables affect one another, so careful control of each is required to ensure smooth, bead-free nanofibers. A polymer concentration of 10 wt. % was found to be the ideal concentration of TMC in the polymer electrospinning solution. The non-ionogenic polymers were electrospun at ideal weight percentages of 8 wt. %, 10 wt. %, 12 wt. % and 18 wt. % for PEO, PVA, PAM and PVP, respectively. These conditions were determined experimentally, and are dependent upon a number of parameters, some of which include solution viscosity and molecular weight, for sufficient chain entanglement.

A certain minimum polymer concentration is required to facilitate fiber formation during electrospinning.[23] At these concentrations, sufficient polymer chain entanglement occurs to stabilize the solution ejected from the needle tip, causing nanofiber formation as the solvent evaporates. Below this critical concentration value, application of voltage results in electrospraying and bead formation primarily due to the Rayleigh instability phenomenon (capillary wave break up). At such low polymer concentrations, an insufficiently deformable entangled network of polymer chains exist.[24] The progressive increase in PEO polymer concentration electrospun into PEO/TMC nanofibers is presented in Figure 5.2, in order to exemplify this observation.

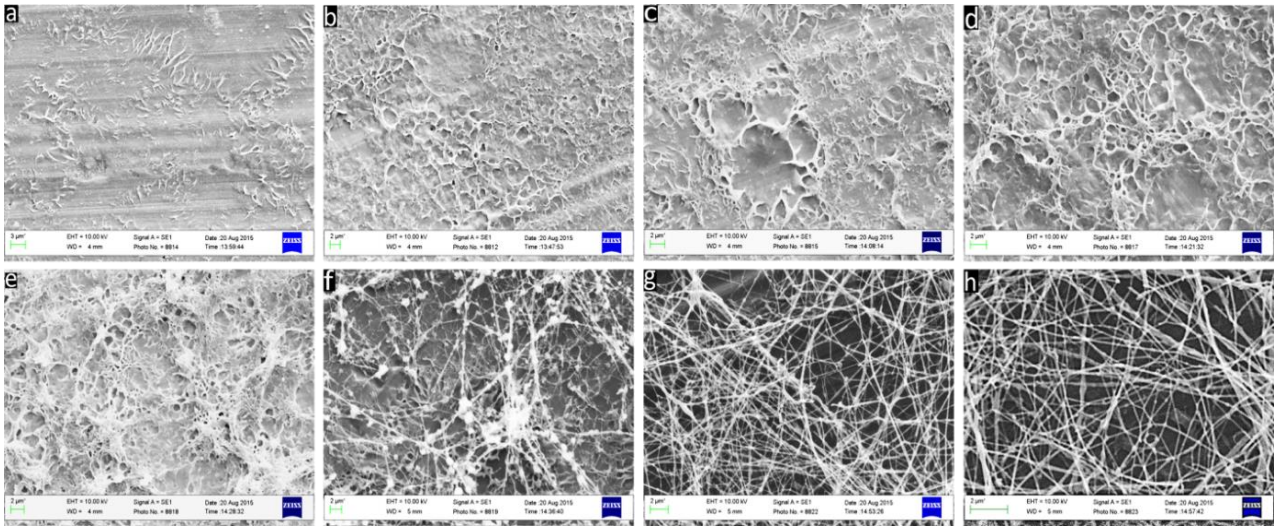

Figure 5.2 Scanning electron microscopy images of PEO polymer solution in water, DMSO and NONIDAC at (a) 1 wt. % (b) 2 wt. % (c) 3 wt. % (d) 4 wt. % (e) 5 wt. % (f) 6 wt. % (g) 7 wt. % and (h) 8 wt. % polymer, mixed with TMC 10 wt. %, 70/30 (v/v) ratio.

As the PEO concentration increased from 1- to 5 wt. %, the polymer morphology transformed from a sputtered electrospray of networked droplets to a porous sponge-like morphology. At 6 wt. % PEO polymer inclusion, nanofibers started to take form as higher degrees of chain entanglement facilitated the formation of a more structured ball-on-string morphology. At 7 wt. % PEO polymer concentration, beaded nanofibers resulted and finally, at 8 wt. %, smooth continuous nanofibers were produced. An upper limit of polymer concentration exists above 8 wt. % for this system, where the high solution viscosity impeded the electrospinning process.

After each separate polymer solution was prepared and homogenised for 24 h, TMC was blended with the non-ionogenic polymer solutions in a ratio of 70/30 (non-ionogenic polymer/TMC, v/v). Various studies conducted have concluded that the addition of PVA to a quaternized chitosan solution facilitated nanofiber formation, but only at lesser inclusions of quaternized chitosan relative to PVA.[25-27] The ratio of 70/30 was thus chosen and kept constant among all polymer blends so as to obtain comparable results. Since all polymers used are water-soluble, efforts were made to electrospin TMC/PVA, TMC/PEO, TMC/PVP and TMC/PAM in solvent systems of pure water. With careful control of process parameters, continuous nanofibers were fabricated. Electrospinning from a solvent system of pure water is advantageous in many respects, but the nanofibers obtained from purely aqueous electrospinning, however, had very low throughputs and slight fusion of adjacent nanofibers was observed due to the slow evaporation rate of water.

To obtain better nanofibrous structures and electrospinning throughputs, NONIDAC was introduced into the solution as a non-ionic surfactant as well as dimethyl sulfoxide (DMSO) (10 %, v/v) as a co-solvent in order to improve processing conditions and increase fiber yields through the relaxation of polymer chain entanglement.[18] Scanning electron microscopy (SEM) was used to

analyse the size and morphology of the electrospun bi-component polymer nanofibers, the results of which are presented in Figure 5.3.

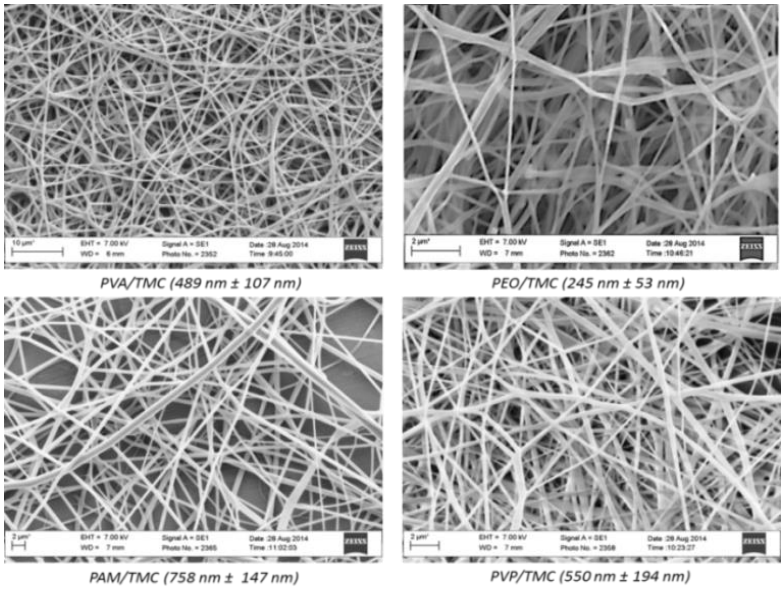

Figure 5.3 SEM images of (a) PVA/TMC nanofibers, (b) PEO/TMC nanofibers, (c) PAM/TMC nanofibers and (d) PVP/TMC nanofibers.

The nanofibers obtained had average diameters of 245 ± 53 nm, 489 ± 107 nm, 550 ± 194 nm and 758 ± 147 nm for PEO/TMC, PVA/TMC, PVP/TMC and PAM/TMC polymer combinations, respectively. The diameter range distributions are illustrated in Figure 5.4. PVA/TMC nanofibers and PEO/TMC nanofibers had the smallest diameters and diameter range distributions.

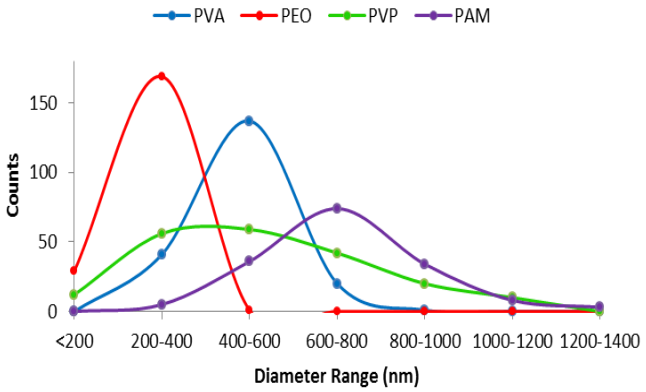

Figure 5.4 PVA/TMC, PEO/TMC, PVP/TMC and PAM/TMC bi-component nanofiber diameter distribution curves.

5.2.2 Crosslinking TMC/non-ionogenic polymer bi-component nanofibers

The *N*-quaternized derivatives, such as TMC, are water soluble due to their permanently charged ammonium ion groups. This is a highly sought after attribute in biological applications. Whilst a favourable attribute in some respects, the nanofibrous mats would lose all morphological structure in solution, owing to high swelling ratios and aqueous instability. Crosslinking is a method used to

improve the water stability of polymer nanofibers.[28] Crosslinking agents are molecules with at least two reactive functional groups that allow for the formation of bridges between polymeric chains.[29] Two crosslinking agents (glutaraldehyde and genipin) typically used in the crosslinking of chitosan, are presented in Figure 5.5.

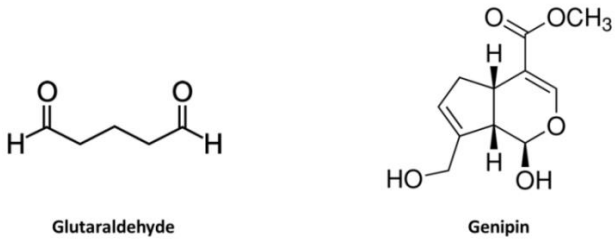

Figure 5.5 Chemical structures of crosslinking agents: glutaraldehyde (left) and genipin (right).

Glutaraldehyde (GA) or 1,5-pentanodial is extensively used in protein immobilization and crosslinking through amino groups because it is a low-cost and convenient way to promote fixation.[30] The aldehyde groups of glutaraldehyde form covalent imine bonds with the amino groups of chitosan, due to the resonance established with adjacent double ethylenic bonds via a Schiff reaction.[29] A considerable drawback, however, is that it is generally considered to be cytotoxic.[31]

More pertinently, it is difficult to control the reaction rate and experimental conditions when exposing the nanofibrous mats to GA vapour within a desiccator for crosslinking. Often, the nanofibrous morphology was completely lost after crosslinking and unwanted polymer films were produced. By careful control of the crosslinking process, however, PVA/TMC nanofibers were able to crosslink via glutaraldehyde in dilute concentration conditions. Less success was attained in the crosslinking of PEO/TMC and PAM/TMC nanofibers. Figure 5.6 shows the rapid progression of nanofibers to film formation of PEO/TMC nanofibers with increasing GA vapour exposure times.

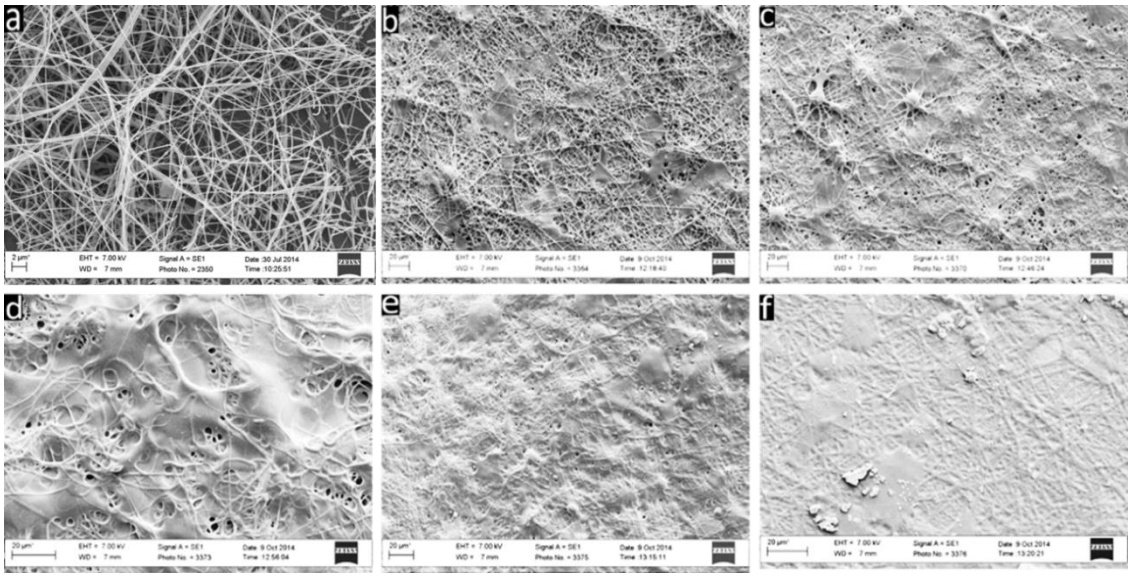

Figure 5.6 SEM images displaying the progression of PEO/TMC nanofibers to film formation by exposure to 15 % GA vapour for (a) 1h, (b) 2 h, (c) 4 h, (d) 8 h (e) 24 h and (f) 48 h.

Other covalent crosslinking agents for chitosan were therefore investigated as alternatives. Genipin is a natural and water-soluble crosslinking agent, which has drawn considerable attention in recent years. It is obtained from geniposide, a component of traditional Chinese medicine and is isolated from the fruits of the plant, *Gardenial jasminoides* Ellis. Genipin is a fully biocompatible reagent and approximately 10 000 times less cytotoxic than glutaraldehyde.[32] Genipin was therefore chosen as suitable crosslinking agent for PEO and PAM chitosan based nanofibers, which were unable to be efficiently crosslinked using GA vapour.

As the PVA/TMC nanofibers could also be crosslinked using genipin, a comparison between the effects of the two crosslinking agents, namely, glutaraldehyde and genipin, could be drawn for PVA/TMC nanofibers. This was done in order to analyse the influence that the crosslinking agent had on nanofiber formation and morphology, as well as to determine whether there was any effect on the binding ability of chitosan based nanofibers to mycobacteria. The latter will be discussed in Chapter 6.

SEM was used to observe the morphological effects of crosslinking. The covalent crosslinking of PVA/TMC nanofibers using genipin and dilute GA vapour was successfully achieved as shown in Figure 5.7 (b) and (c), respectively. In comparison to the as-spun nanofibrous mats, fusion of adjacent nanofibers and a high degree of swelling after water vapour exposure was observed for the genipin crosslinked nanofibers.

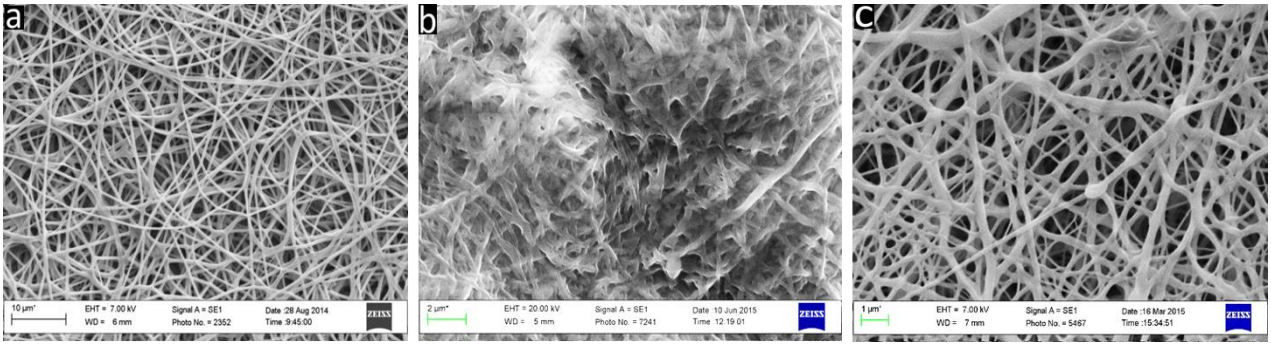

Figure 5.7 SEM images of PVA/TMC nanofibers (a) as electrospun, (b) post genipin crosslinking and water absorption and (c) post 5% GA vapour crosslinking.

Disparately, crosslinking of modified chitosan nanofibers by glutaraldehyde caused a less significant transformation of morphology. The colour of genipin-crosslinked chitosan mats changed from white to dark blue and is associated with the reaction of genipin with the amino groups of chitosan.[33] This colour change was facilitated by the water vapour absorption of the nanofibrous mats, which was achieved by placing the mats in a desiccator containing a specific amount of water at 30 °C for 24 h, post electrospinning.

It has been proven that GA crosslinked chitosan mats exhibited less swelling in solution than genipin crosslinked chitosan mats. An extensive analysis on the swelling degrees of GA and genipin crosslinked chitosan mats was done by the group of Mirzaei, and it was found that the swelling ratios of chitosan mats did not decrease significantly using genipin as crosslinking agent, whilst crosslinking by GA reduced the swelling ratio significantly in comparison with the uncrosslinked mats (P value < 0.05). In this way, crosslinking by genipin did not decrease the water absorption capability of chitosan nanofibers, unlike that of GA crosslinked mats.[28] This is an important consideration for biological applications which require the adhesion of bacteria to substrates immersed in aqueous based solutions.

Difficulties were again incurred through the use of glutaraldehyde, genipin and sodium triphosphate (TPP) as crosslinking agents for modified chitosan based polyacrylamide (PAM) nanofibers. TPP is a multivalent anion that can form crosslinks by ionic interaction between positively charged ammonium ($–NH_3^+$) groups of chitosan and multivalent negatively charged TPP molecules.[35] Although smooth nanofibers were obtained from the electrospinning process, crosslinking the nanofibers to form water stable structures for use in future solution phase processes such as mycobacterial incubation, proved challenging. Film formation resulted after 1 h GA vapour (5%) exposure, as observed using SEM analysis in Figure 5.8.

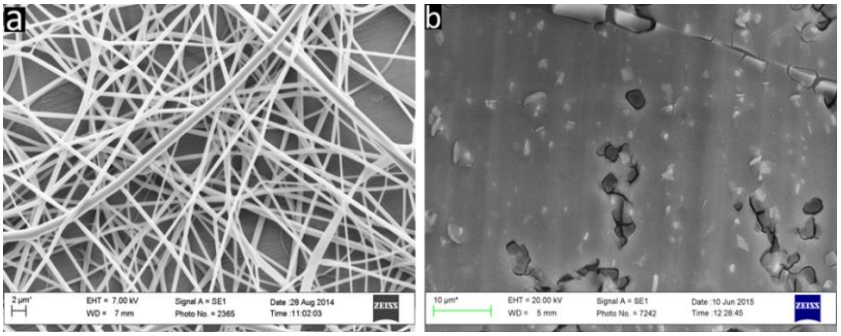

Figure 5.8 SEM images of (a) as electrospun and (b) post glutaraldehyde crosslinking of PAM/TMC nanofibers.

When solubility studies were done, a loss of nanofiber integrity occurred after 30 min of suspension in phosphate buffered solution (PBS), forming a viscid polymeric gum. Genipin and TPP are crosslinking agents that are added to the polymer solution 5 min prior to electrospinning. These methods produced an electrospray of polymer droplets, which could not be used to form a relative comparison with PVA/TMC, PEO/TMC and PVP/TMC nanofibers. For these reasons, the PAM/TMC blend was removed from the study.

PVP/TMC nanofibers were crosslinked via thermal treatment. Figure 5.9 (a) shows the SEM image of PVP/TMC nanofibers 1 h after electrospinning, prior to thermal crosslinking. PVP is intensely hygroscopic, able to absorb up to 40% of its weight in atmospheric moisture.[34] PVP/TMC

nanofibers thus readily lost its nanofibrous structure if crosslinking did not ensue immediately after electrospinning. Figure 5.9 (b) shows the consolidated nanofibrous morphology of PVP/TMC nanofibers after thermal treatment at 200 °C for 4 h.

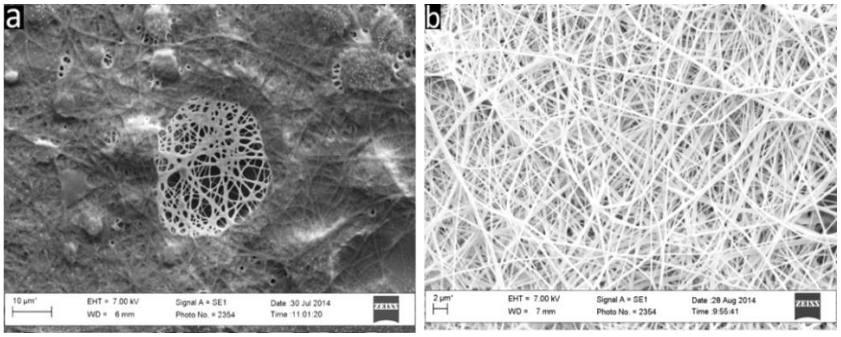

Figure 5.9 SEM images of (a) as electrospun and (b) post thermal crosslinking PVP/TMC nanofibers.

5.2.3 Wettability of chitosan based bi-component nanofibers

The wettability of a polymer influences its behaviour in solution and has a significant effect on its ability to interact with bacteria to facilitate attachment and binding. Surfaces of materials have been commonly classified as hydrophobic, with water contact angles larger than 90°, and hydrophilic with contact angles of smaller than 90°.[36] The water contact angles associated with different types of surface effects are reiterated in Figure 5.10.

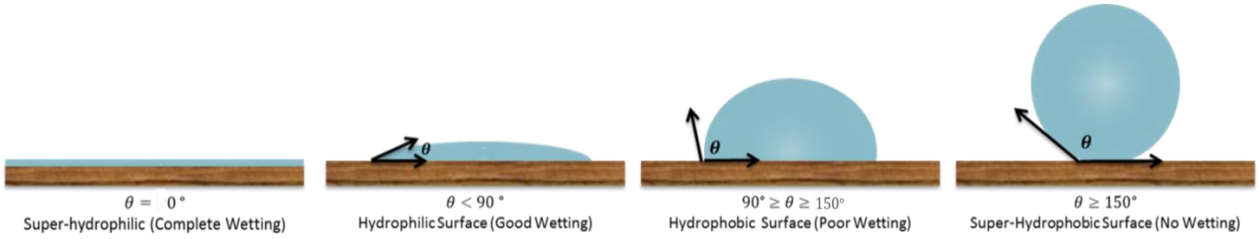

Figure 5.10 Hydrophilic surfaces cause spreading of water droplets to increase the contact surface area and hydrophobic surfaces cause contraction to minimize the contact surface area.

Quaternized chitosan and the non-ionogenic polymers used in this study are inherently hydrophilic, water-soluble polymers. Consequently, the electrospinning of these aqueous polymer solutions produced water soluble nanofibers, able to disintegrate via atmospheric moisture uptake and handling. Contact angle measurements of all of the uncrosslinked mats exhibited complete wetting ($\theta = 0°$), indicating superhydrophilicity. All of the crosslinked nanofibrous mats were also found to be hydrophilic in nature, though it should be noted that the crosslinking methodology had an influence on the water contact angle measured. The crosslinked mats showed higher contact angles, which indicated that they were therefore more hydrophobic in nature than the uncrosslinked mats, though near complete wetting was observed for all of the mats tested. Water contact angles of 12°, 7° and 5° were measured for the crosslinked PVA/TMC, PEO/TMC and PVP/TMC nanofiber mats.

In order to obtain a more accurate representation of the hydrophilic/hydrophobic nature of the various polymers, solvent cast polymer films were analysed for water contact angle measurements. The chitosan based polymer, TMC, was more hydrophilic than PVA, PEO and PVP. PAM was the most hydrophilic of all the polymers tested, and could in part account for the difficulties incurred in crosslinking this polymer based blend of nanofibers. The water droplet spreads over the PAM polymer film in order to maximise its surface contact, seen in Figure 5.11 (f). PVA was the most hydrophobic of all non-ionogenic polymers tested. By blending PVA with TMC, a slight decrease in the hydrophobicity of the film was achieved, as observed in Figure 5.11 (c). Water contact angle measurements of 89°, 87° and 46° were obtained for PVA, PVA/TMC blend and TMC polymer films, respectively. Water contact angle measurements of 72°, 57° and 30° were obtained for the other non-ionogenic polymers, namely PVP, PEO and PAM, respectively.

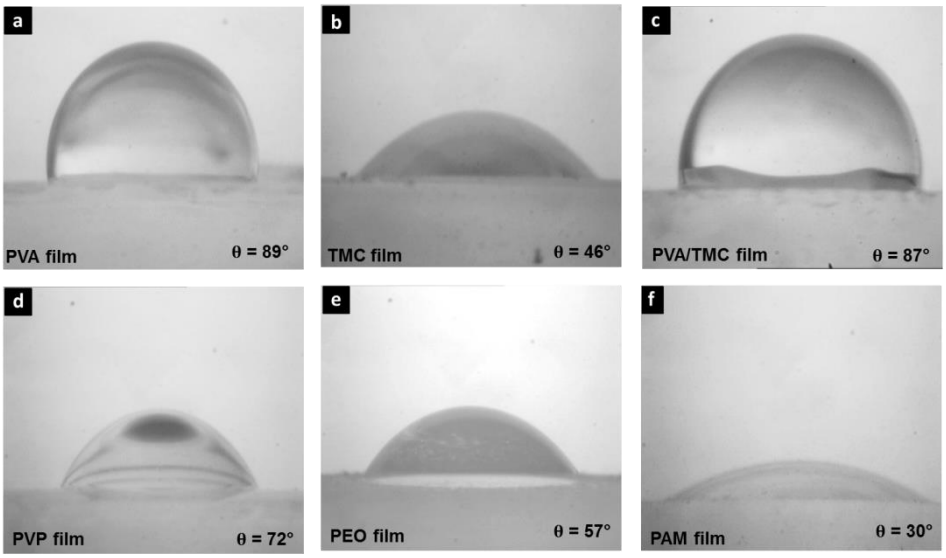

Figure 5.11 Water contact angle measurements of polymer films illustrating degree of hydrophilicity.

5.2.4 Surface Area and Porosity Analysis

Nanofibers prepared via the electrospinning technique typically have unique properties such as high specific surface area and high porosity with fine pores. The specific surface area and porosity of PVA/TMC, PEO/TMC and PVP/TMC nanofibers were measured by Brunauer–Emmett–Teller (BET) analysis, the results of which are presented in Table 5.1.

Table 5.1 Surface area and porosity analysis

Bi-component nanofiber	*Specific surface area (m^2/g)*	*Total pore volume (cm^3/g)*	*Average pore width (Å)*
PVA/TMC	442.16	0.0794	7.190
PEO/TMC	452.35	0.0797	7.050
PVP/TMC	438.14	0.0790	7.216

BET analysis revealed high specific surface areas for all three nanofibrous mats, with similar and comparable results being obtained for each nanofiber system. PEO/TMC nanofibers were found to have the greatest BET surface area, followed by PVA/TMC nanofibers and lastly PVP/TMC nanofibers having the smallest surface area. These results are in good agreement with the measured average fiber diameters though use of SEM imaging which was measured to be 245 nm, 489 nm, 550 nm for PEO/TMC, PVA/TMC and PVP/TMC nanofibers, respectively. The chitosan based nanofibers have corresponding average pore sizes, which allow for the classification of these nanofibers into the mesoporous structure group (pore size 2 – 50 Å).[37]

5.3 Conclusion

The high charge densities along the polymer backbones of quaternized chitosan derivatives create the unfeasibility of fiber formation via the electrospinning process. A suitable non-ionogenic polymer was blended with quaternized chitosan in order to minimize the charge repulsion between the polymer chains thereby facilitating sufficient chain entanglement for the formation of nanofibers.

Uncrosslinked electrospun chitosan based nanofibrous mats lose their fibrous structure in contact with water owing to their high swelling ratio and solubility in aqueous media. Crosslinking is a method in which to improve the water stability of these nanofibers by binding to and linking the free amino groups of chitosan and its derivatives. In this study, genipin was used as a safe and biocompatible crosslinking agent for chitosan instead of glutaraldehyde which is the more commonly used, but cytotoxic crosslinking agent.

In comparison to the as-spun nanofibrous mats, fusion of adjacent nanofibers and a high degree of swelling after water vapour exposure was observed for the genipin crosslinked nanofibers. Conversely, crosslinking of modified chitosan nanofibers by glutaraldehyde caused a less significant transformation of morphology. Further research on chitosan crosslinked nanofibrous

mats revealed that crosslinking with genipin, compared to glutaraldehyde, did not significantly decrease the nanofiber swelling ratios in aqueous suspension and the nanofibers were thus able to retain water absorption capability. Glutaraldehyde had the opposite effect, where the water absorption capability of the nanofibers was significantly decreased. The swelling of nanofibers in solution is an important consideration for biological applications such as the adhesion of bacteria to substrates, which requires the mobility of bacteria in physiological fluid and aqueous media.

5.4 Experimental

5.4.1 Materials

The following non-ionogenic polymers were utilised in this part of the project: polyvinyl alcohol (PVA) (M_W = 160 kD), polyethylene oxide (PEO) (M_W = 300 kD), polyvinyl pyrrolidone (PVP) (M_W = 360 kD) and polyacrylamide (PAM) (M_W = 100 kD) were purchased from Aldrich. The following chemicals were utilised in this part of the project: glutaraldehyde (50% in H_2O, Merck), genipin (Sigma-Aldrich, ≥98%), dimethyl sulfoxide (Merck, ≥99.9%) and NONIDAC 11 P S0-70 (Sasol).

5.4.2 Characterization Techniques

a) Scanning electron microscopy (SEM)

Images of the nanoparticles were obtained using a Leo® 1430VP scanning electron microscope (SEM). The sample fibers on aluminum foil were cut into approximately 1 cm^2 squares and attached onto the SEM stub with double sided carbon tape. The SEM stubs were then sputter coated with gold under vacuum prior to imaging. The images were analyzed using *SEM Image Studio*, an imaging analysis program, to obtain data regarding the fiber diameter and size distributions.

b) Water Contact Angle

The hydrophobicity or hydrophilicity of polymer surfaces was determined using static contact angle measurements. Magnification was achieved using a Zeiss microscope unit. A 1 μL drop of distilled water was placed onto the sample mat and the magnified image was captured using a Nikon SMZ-2T (Japan). Static contact angles were measured using Carl Zeiss AxioVision LE software. Figure 5.12 illustrates the captured image of a water droplet with the marked parameters that were needed to calculate the contact angle. Equation 5.1 was used to determine the static contact angle.

$$\theta = 2 \times tan^{-1}\left(\frac{H}{R}\right) \quad (5.1)$$

An average of 10 droplets was used in order to determine the static contact angle.

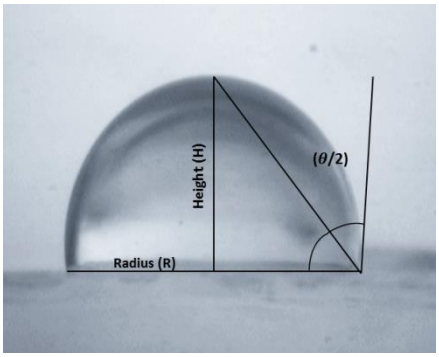

Figure 5.12 Static contact angle parameters needed for determination of the contact angle.

d) Surface Area and Porosity Analysis

The specific surface areas (SSA) and porosity analyses of the nanofibrous mats were determined via the Brunauer–Emmett–Teller (BET) method.[38] The activation conditions of the mats included degassing at 100°C for 4 h with a Micrometrics ASAP 2010 (Accelerated Surface Area and Porosity System) using nitrogen gas as an adsorbent. Each degassed sample (0.1 – 0.4 g) was weighed accurately to four decimal places and placed in a sample tube. Analyses were performed using an automatic multi-point adsorption programme, measuring the volume of nitrogen adsorbed by the sample at a range of N_2 pressures.

5.4.3 Experimental procedures

a) Electrospinning set-up

A horizontal, single-needle electrospinning setup was used for nanofiber production shown in Figure 5.13. It comprises a high-voltage power supply, a syringe pump, a syringe containing polymer solution and a conductive collection surface. Disposable 3 mL syringes and 8 mm diameter steel needle tips were utilized in all electrospinning procedures.

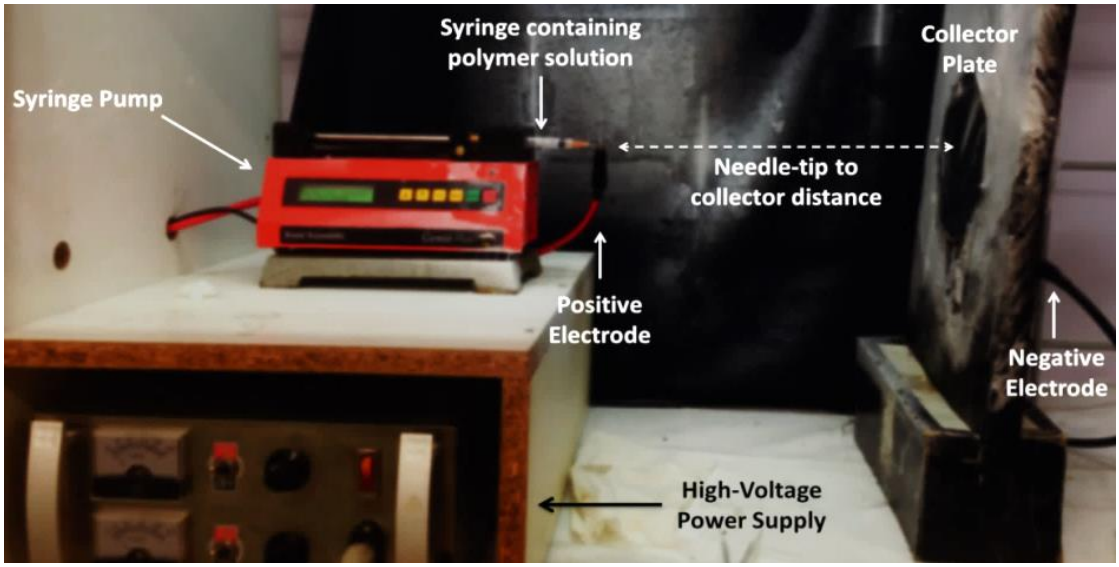

Figure 5.13 Horizontal electrospinning setup.

b) Preparation of bi-component nanofibers

i) PVA/TMC nanofibers

A TMC polymer solution (10 wt. %) and a PVA polymer solution (10 wt. %) were prepared separately by dissolving TMC and PVA in Milli-Q water under magnetic stirring at room temperature for 24 h. The obtained solutions were then combined in a 70/30 ratio of PVA/TMC (10 mL, v/v). DMSO (10%, v/v) and NONIDAC (0.5 wt. %) were then added to the polymer blend solution, and magnetic stirring continued for 24 h. PVA/TMC nanofibers were fabricated by electrospinning the polymer solution at a flow rate of 0.013 mL/min, a spinning distance of 20 cm, a positive voltage of 10 kV and a negative voltage of -5 kV. The nanofibers were collected on a watch glass covered with aluminium foil.

ii) PEO/TMC nanofibers

A TMC polymer solution (10 wt. %) and a PEO polymer solution (8 wt. %) were prepared separately by dissolving TMC and PEO in Milli-Q water under magnetic stirring at 50 °C for 24 h. The obtained solutions were then combined in a PEO/TMC ratio of 70/30 (10 mL, v/v). DMSO (10%, v/v) and NONIDAC (0.5 wt. %) were then added to the polymer blend solution, and magnetic stirring continued for 24 h. PEO/TMC nanofibers were fabricated by electrospinning the polymer solution at a flow rate of 0.014 mL/min, a spinning distance of 20 cm, a positive voltage of 15.5 kV and a negative voltage of -5 kV. The nanofibers were collected on watch glass covered with aluminium foil.

iii) PVP/TMC nanofibers

A TMC polymer solution (10 wt. %) and a PVP polymer solution (18 wt. %) were prepared separately by dissolving TMC and PVP in Milli-Q water under magnetic stirring at room temperature for 24 h. The obtained solutions were then combined in a PEO/TMC ratio of 70/30 (10 mL, v/v). DMSO (10%, v/v) and NONIDAC (0.5 wt. %) were then added to the polymer blend solution, and magnetic stirring continued for 24 h. PEO/TMC nanofibers were fabricated by electrospinning the polymer solution at a flow rate of 0.015 mL/min, a spinning distance of 20 cm, a positive voltage of 15 kV and a negative voltage of -5 kV. The nanofibers were collected on a watch glass covered with aluminium foil.

iv) PAM/TMC nanofibers

A TMC polymer solution (10 wt. %) and a PAM polymer solution (12 wt. %) were prepared separately by dissolving TMC and PAM in Milli-Q water under magnetic stirring at room temperature for 24 h. The obtained solutions were then combined in a PAM/TMC ratio of 70/30 (10 mL, v/v). DMSO (10%, v/v) and NONIDAC (0.5 wt. %) were then added to the polymer blend solution, and magnetic stirring continued for 24 h. PAM/TMC nanofibers were fabricated by electrospinning the polymer solution at a flow rate of 0.005 mL/min, a spinning distance of 20 cm, a positive voltage of 10 kV and a negative voltage of -5 kV. The nanofibers were collected on a watch glass covered with aluminium foil.

c) Crosslinking bi-component nanofibrous mats

i) Crosslinking with glutaraldehyde vapour

To obtain glutaraldehyde-crosslinked modified chitosan nanofibers, the electrospun nanofibrous mats of PVA/TMC, PEO/TMC and PAM/TMC were exposed to the vapour of 5% (w/v) GA aqueous solution in a desiccator at room temperature for 24 h, separately. The resultant nanofibrous mats were dried under vacuum at 37 °C for 24 h, and stored for further analysis.

ii) Crosslinking with genipin

To obtain genipin-crosslinked modified chitosan nanofibers, 0.1% (w/v) genipin was added to the polymer blend solutions of PVA/TMC, PEO/TMC and PAM/TMC at room temperature with constant stirring, 5 min prior to electrospinning each polymer blend solution. The obtained nanofibrous mats were removed from the collector plate and immediately exposed to water vapour in a desiccator at 30 °C for 24 h. To create the water vapour chamber, a glass Petri dish was filled with 5 mL distilled

water and placed at the bottom of a desiccator. After 24 h, the mats were washed with ethanol, dried under vacuum at 37 °C for 24 h, and stored for further analysis.

iii) Crosslinking by thermal treatment

The PVP/TMC nanofibrous mat was carefully removed from the foil and placed on a watch glass, which was then placed in a vacuum oven at 200 °C for 4 h, rendering water stability. At this temperature, PVP oxidises and crosslinks.[39]

5.5 References

1. Kim, T.G.; Park, T.G. *Biotechnol. Progr*. **2006**, *22*, 1108-1113.
2. Tang, C.; Saquing, C. D.; Harding, J. R.; Khan, S. A. *Macromolecules* **2009***, 2,* 630-637.
3. Duan, B.; Wu, L.; Yuan, X.; Hu, Z.; Li, X.; Zhang, Y.; Yao, K.; Wang, M. *J. Biomed. Mater. Res. A* **2007***, 3,* 868-878.
4. Li, L.; Hsieh, Y. *Carbohydr. Res.* **2006***, 3,* 374-381.
5. Desai, K.; Kit, K.; Li, J.; Zivanovic, S. *Biomacromolecules* **2008***, 3,* 1000-1006.
6. Geng, X.; Kwon, O.; Jang, J. *Biomaterials* **2005***, 27,* 5427-5432.
7. Park, W. H.; Jeong, L.; Yoo, D. I.; Hudson, S. *Polymer* **2004***, 21,* 7151-7157.
8. Shukla, A. *Intelligent Medical Technologies and Biomedical Engineering: Tools and Application*; Igi Global, **2010**.
9. Sun, K.; Li, Z. *Exp. Polym. Lett.* **2011***, 4,* 342-361.
10. Ding, B.; Kim, H.; Lee, S.; Shao, C.; Lee, D.; Park, S.; Kwag, G.; Choi, K. *J. Polym. Sci. B* **2002***, 13,* 1261-1268.
11. Deitzel, J.; Kleinmeyer, J.; Hirvonen, J.; Tan, N. B. *Polymer* **2001***, 19,* 8163-8170.
12. Desai, K.; Kit, K. *Polymer* **2008***, 19,* 4046-4050.
13. Ignatova, M.; Manolova, N.; Rashkov, I. *Eur. Polym. J.* **2007***, 4,* 1112-1122.
14. Mansur, H. S.; Oréfice, R. L.; Mansur, A. A. *Polymer* **2004***, 21,* 7193-7202..
15. Peresin, M. S.; Habibi, Y.; Zoppe, J. O.; Pawlak, J. J.; Rojas, O. J. *Biomacromolecules* **2010***, 3,* 674-681.
16. Asran, A. S.; Henning, S.; Michler, G. H. *Polymer* **2010***, 4,* 868-876.
17. Harris, J. M. *; Springer* **2013**.
18. Bhattarai, N.; Edmondson, D.; Veiseh, O.; Matsen, F. A.; Zhang, M. *Biomaterials* **2005***, 31,* 6176-6184.
19. Kriegel, C.; Kit, K.; McClements, D. J.; Weiss, J. *Polymer* **2009***, 1,* 189-200.
20. Yang, Q.; Li, Z.; Hong, Y.; Zhao, Y.; Qiu, S.; Wang, C.; Wei, Y. *J. Polym. Sci. B* **2004***, 20,* 3721-3726.
21. Yu, D.; Wang, X.; Li, X.; Chian, W.; Li, Y.; Liao, Y. *Acta. Biomaterialia* **2013***, 3,* 5665-5672.
22. Singh, R. P.; Nayak, B. R.; Biswal, D. R.; Tripathy, T.; Banik, K. *Mater. Res. Innov.* **2003***, 5,* 331-340.
23. Shenoy, S. L.; Bates, W. D.; Frisch, H. L.; Wnek, G. E. *Polymer* **2005***, 10,* 3372-3384.

24. Tan, S.; Huang, X.; Wu, B. *Polym. Int.* **2007**, *11,* 1330-1339.

25. Ohkawa, K.; Cha, D.; Kim, H.; Nishida, A.; Yamamoto, H. *Macromol. Rapid Comm.* **2004**, *18,* 1600-1605.

26. Dai, J.; Gong, A. *J. Yangtze Univ.* **2009**, 058.

27. Zheng, H.; Du, Y.; Yu, J.; Huang, R.; Zhang, L. *J Appl. Polym. Sci.* **2001**, *13,* 2558-2565.

28. Mirzaei, E.; Faridi-Majidi, R.; Shokrgozar, M. A.; Asghari Paskiabi, F. *Nanomed. J.* **2014**, *3,* 137-146.

29. Berger, J.; Reist, M.; Mayer, J. M.; Felt, O.; Peppas, N.; Gurny, R. *Eur. J. Pharm. Biopharm.* **2004**, *1,* 19-34.

30. Beppu, M.; Vieira, R.; Aimoli, C.; Santana, C. *J. Membr. Sci.* **2007**, *1,* 126-130.

31. Carreno-Gomez, B.; Duncan, R. *Int. J. Pharm.* **1997**, *2,* 231-240.

32. Nishi, C.; Nakajima, N.; Ikada, Y. *J. Biomed. Mater. Res.* **1995**, *7,* 829-834.

33. Mi, F.; Sung, H.; Shyu, S. *J. Polym. Sci. A1* **2000**, *15,* 2804-2814.

34. Xie, J.; Mao, H.; Yu, D.; Williams, G. R.; Jin, M. *Fiber Polym.* **2014**, *1,* 78-83.

35. Fernandes, S. C.; de Oliveira, Inês Rosane WZ; Fatibello-Filho, O.; Spinelli, A.; Vieira, I. C. *Sensor Actuat. B-Chem.* **2008**, *1,* 202-207.

36. Drelich, J.; Chibowski, E. *Langmuir* **2010**, *24,* 18621-18623.

37. McCusker, L.; Liebau, F.; Engelhardt, G. *Pure Appl. Chem.* **2001**, *2,* 381-394.

38. Brunauer, S.; Emmett, P. H.; Teller, E. *J. Am. Chem. Soc.* **1938**, *2,* 309-319.

39. Díaz, J. E.; Barrero, A.; Márquez, M.; Loscertales, I. G. *Adv. Func. Mater.* **2006**, *16,* 2110.

Chapter Six

Affinity Studies between Modified Chitosan Nano-substrates and Mycobacteria

6.1 Introduction

Bacterial adhesion is a complex process governed by numerous factors. Broadly, these include the distinctive characteristics of the bacteria itself, the properties of the substrate (polymer nanofibers and nanoparticles) and environmental factors. The environmental factors generally comprise temperature, pH, period of incubation, bacterial concentration, chemical treatment and the presence of antibiotics.[1] Knowledge of the unique behaviour of *Mycobacterium tuberculosis* (*M. tuberculosis*) is required in order to understand the binding mechanism of this bacterium to specific substrates.

6.1.1 Cell Wall Chemistry

M. tuberculosis has a highly complex bacterial cell wall envelope. The cell wall of the pathogen resembles that of a Gram-positive bacterium, though it is not classified as being either Gram-positive or Gram-negative. Current understanding of its structure reveals a three-compartment entity composed of a plasma membrane; the cell wall core and the extractable noncovalently linked glycans, lipids, and proteins.[2,3] The lipid complexes include acyl glcolipids and other complexes such as free lipids and sulfolipids, and there are porins in the membrane to facilitate transport.[4] The cell envelope contains a polypeptide layer, a peptidoglycan layer, and free lipids. In addition, there is also a complex structure of fatty acids such as mycolic acids.[5] The *M. tuberculosis* cell wall contains three classes of mycolic acids: alpha-, keto- and methoxymycolates.[6]

There are various distinct charged groups present in the bacterium cell wall that may associate or dissociate upon changes in pH or ionic strength of the suspending fluid. These groups define certain affinity when a bacterium approaches the charged surface of another bacterium or a substrate. The involved surface electrostatic interactions may induce particular changes in the conformation of charged molecules in favour of repulsion or adhesion to surfaces. Moreover

changes in the associated peptidoglycan layer of the bacterial cell wall may change its permeability to solvent, solutes and ions.[7,8] A section of the mycobacterial cell wall of *M. tuberculosis* is schematically illustrated in Figure 6.1, highlighting the complex structure.[9]

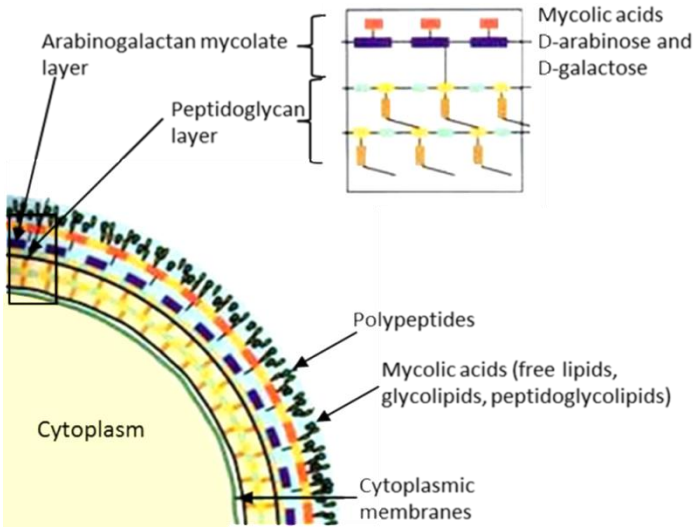

Figure 6.1 Simplified construction of the outer cell wall of Mycobacterium tuberculosis.

6.1.2 Nonspecific Interactions

Bacteria adhere to host cells and to artificial substrates through both biospecific and selective interactions based on the cell wall chemistry of the bacteria as well as nonspecific interactions such as hydrophobic and electrostatic interactions. Substrate surfaces possessing chemically bonded hydrophobic polycations of quaternary ammonium salts have been found to possess bacterial adhesive properties. The substrate surfaces which possess ammonium salts or quaternary ammonium groups have been proven to damage a host of cells through the disruption of their cellular membranes, by disrupting the net negative charge of the membrane of the bacteria, causing cell lysis and death.[10,11]

It has been established that the alkyl chain length of quaternary ammonium cations have an influence on bacterial activity. Studies were directed towards understanding these effects and it was found that those compounds containing alkyl chains of 12 – 16 carbons showed resistance to Gram-positive bacteria, whereas alkyl chain lengths of 12 – 14 carbons were more effective against Gram-negative bacterial cells. Alkyl groups containing <4 and >18 carbons were proven to be ineffective against bacteria. These studies were based on the bactericidal activity of polycations, but can be related to bacterial adhesion as it precedes cell lysis and death.[12-15]

6.2 Results and Discussion

Modified chitosan based bi-component nanofibers and modified chitosan coated SPMN nanocomposites were tested for their affinity towards *M. tuberculosis*. The compounds chosen in this study for the modification of chitosan were selected based on possible chemical interaction with this bacterium, for which bacillus Calmette–Guérin (BCG) was used as an *M. tuberculosis*-mimic as it is an attenuated derivative of *Mycobacterium bovis*, a virulent tubercle bacillus genetically similar to *M. tuberculosis*.[16] BCG also belongs to the *Mycobacterium tuberculosis* complex (MTC). Affinity studies were therefore conducted to evaluate the interaction between BCG and the modified chitosan based nano-substrates, the chemical binding of which may be referred to as 'capture'.

The general procedure entailed the incubation of mycobacteria at specific concentrations with the modified polymer nano-substrates, after which thorough washing with phosphate buffered solution (PBS) ensued. It was assumed that any mycobacteria found on the surfaces of the nano-substrates after extensive wash steps would be as a result of the chemical interaction between BCG and the modified chitosan nano-substrates. The capture of mycobacteria by the various modified chitosan nano-substrates was evaluated by fluorescence microscopy (FM), light microscopy (LM), transmission electron microscopy (TEM) and field emission scanning electron microscopy (FE-SEM). This chapter will be divided into two sections: part one comprising the affinity studies of bi-component nanofibers and part two comprising that of the SPMN nanocomposites.

6.2.1 Part one – Bi-component nanofibers

N-trimethylammonium chitosan chloride (TMC) was chosen as representative chitosan derivative to be blended with polyvinyl alcohol (PVA), polyethylene oxide (PEO) and polyvinyl pyrrolidone (PVP). These polymer blends were electrospun into nanofibers, crosslinked and characterized, as detailed in Chapter 5.

a) Affinity Studies

A specific amount (10 mg, approximately 1 cm^2) of the crosslinked, modified chitosan based bi-component nanofibers, namely PVA/TMC, PEO/TMC and PVP/TMC nanofibers were added to a specific volume (5 mL) of BCG culture followed by incubation at 37 °C for 30 min, with agitation. PVA/TMC nanofibers were separately crosslinked using both glutaraldehyde and genipin, thereby enabling the analysis of both crosslinked forms for mycobacterial affinity. The polymer nanofibers were subsequently removed from the tubes containing the BCG culture and washed twice with

PBS (10 min) so as to remove any loosely adhering mycobacteria not properly attached to the surfaces of the modified polymer nanofibers. The nanofibrous mats were initially incubated at an intermediate concentration of 10^6 BCG/mL to determine the overall optimum polymer system for the most efficient capture of mycobacteria. Subsequently, serial dilutions were prepared to a final volume of 5 mL per sample from the original concentration of bacteria so as to establish the sensitivity of each substrate to BCG by determining the minimum detection limit.

The fluorescence and transmission modes of a confocal microscope were used for the detection of BCG captured onto the surface of the nanofibers. Mycobacteria were visualized by staining it with two fluorescent nucleic acid-binding stains, namely propidium iodide and SYTO-9. Propidium iodide is a red dye that penetrates bacterial cells with damaged membranes and SYTO-9 is a green dye that penetrates all bacterial cells – those with intact membranes and those with damaged membranes. Viable bacterial cells with intact membranes are thus stained fluorescent green and nonviable cells with damaged membranes are stained fluorescent red.[17]

An evaluation and comparison of the modified polymer blend nanofibers which were tested for BCG capture, is presented in Figure 6.2. In the column (i), FM allows for the visualization of the overlay of viable (SYTO-9 stained) and nonviable (propidium iodide stained) bacteria on the nanofibrous mats and in column (ii), LM allows for the visualization of the morphology at those coordinates. Each nanofibrous mat was additionally tested for any inexplicable fluorescence by means of negative controls (refer to Addendum C) which were dispersed in growth medium and phosphate buffered solution (PBS), with the exclusion of any mycobacteria. No fluorescence was observed. The nanofibrous morphology deteriorated somewhat over time due to the extended period in solution state.

Fluorescence microscopy is able to scan the entire area of the sample and analysis thereof indicated that the strongest mycobacterium-nanofiber surface interaction occurred for polyvinyl alcohol/*N*-trimethylammonium chitosan chloride (PVA/TMC) nanofibers which were crosslinked via genipin, as greater quantities of BCG were visible on the surfaces of these nanofibers.

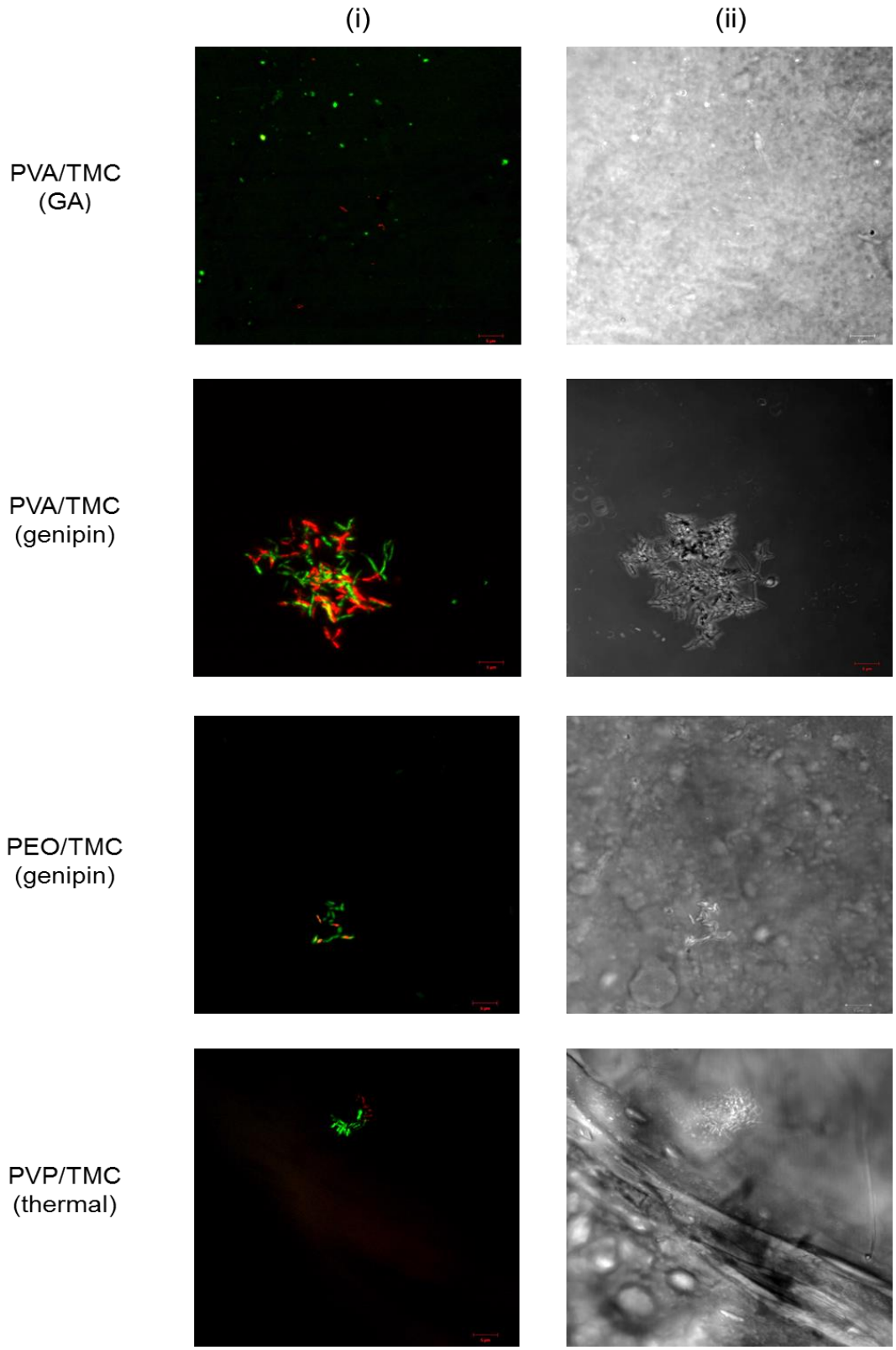

Figure 6.2 Fluorescence Microscopy (FM) and Light Microscopy (LM) images of TMC/non-ionogenic polymer bi-component nanofibers incubated with BCG at a concentration of 10^6 BCG/mL. Images captured at constant magnification.

PVA/TMC crosslinked with genipin showed the greatest affinity towards mycobacteria. The split confocal image of viable/nonviable bacteria and light microscopy, as well as the confocal overlay image of this mat is presented in Figure 6.3 to highlight in detail the rod-like bacterial colony of BCG which was captured. An equivalent ratio of viable/non-viable BCG is observed. This result is in good agreement with literature, which verified that quaternary ammonium moieties of antimicrobial compounds, such as chitosan, interact with the cell wall of bacteria due to the electrostatic interaction between the negatively charged bacterial outer membrane and the positively charged quaternary ammonium moiety of the polymer. Contact between quaternized chitosan and the cell membrane, which is essentially a negatively charged phospholipid bilayer, may slightly change the membrane's permeability, causing general perturbations in the lipid bilayers. The binding also promptly neutralizes and even reverses the surface charge of the bacteria. The increased membrane permeability leads to the destabilization of the cell membrane and leakage of intracellular substances, causing the death of cells.[18–21] The quantity of dead mycobacteria (red) would increase over time due to increased interaction with the cationic moieties of chitosan as well as environmental factors which become non-ideal.

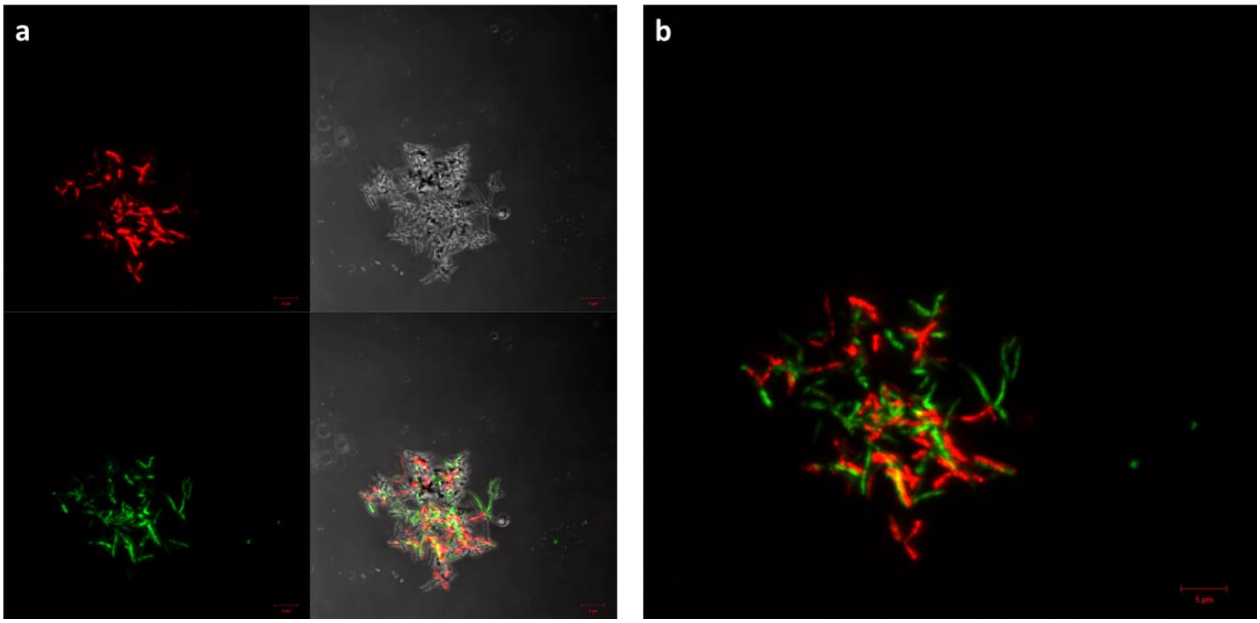

Figure 6.3 PVA/TMC nanofibers crosslinked with genipin and incubated with BCG at a concentration of 10^6 BCG/mL, with the split image on the left in Figure 6.2 (a) and the overlay on the right in Figure 6.2 (b). The green rod-like structures are the bacteria that have been stained with SYTO-9 and are indicative of live bacteria. The red rod-like structures have been stained with propidium iodide and are indicative of dead bacteria.

By serial dilution of mycobacterial cultures, the results also indicated that PVA/TMC and PEO/TMC nanofibers were able to detect mycobacteria at a level as low as 10 BCG/mL. PVP/TMC nanofibers were only able to detect mycobacteria at a level of 10^4 BCG/mL (refer to Addendum D). Based on

these results it can be concluded that BCG was captured onto the nanofibrous surfaces most likely due to the ionic interaction between the negatively charged BCG cell wall and the positively charged quaternary ammonium moiety of modified chitosan, as well as through hydrophobic-hydrophobic interaction between the mycolic acids of the BCG cell wall and the aliphatic methyl groups of TMC.

Crosslinking of PVA/TMC mats via glutaraldehyde (GA) seemed to have inhibited the aggregation of colonies of mycobacteria, a recognized characteristic of this type of bacteria. This could be attributed to the fixative effects associated with this crosslinking agent. It is extensively used in protein immobilization and crosslinking through amino groups, despite its cytotoxicity. Glutaraldehyde has a broad spectrum of activity against bacteria and kills cells quickly by crosslinking their proteins, followed by immobilization.[22]

b) Conditions for bacterial adhesion

It has been established that surfaces which restrict the adhesion of bacteria (inert surfaces) have the following structural characteristics: (1) they are hydrophilic, (2) they are overall electrically neutral, (3) they are hydrogen bond acceptors and (4) they are not hydrogen bond donors.[11,24,25]

The component of the bi-component nanofiber principally responsible for nonspecific interaction with BCG is the charged polycationic modified chitosan polymer, namely TMC, as the non-ionogenic polymers which formed part of this study exhibit overall electrical neutrality. The non-ionogenic polymers are all inherently hydrophilic in nature, though it was proven through water contact angle measurements of solvent cast polymer films (Chapter 5) that PVA is the least hydrophilic polymer.

With regard to points (3) and (4), namely, the hydrogen bond donating or accepting abilities of the monomers which make up the non-ionogenic polymer – by analysing the chemical structure of each non-ionogenic polymer, reiterated in Figure 6.4, it becomes apparent that polyacrylamide (PAM) and polyvinyl pyrrolidone (PVP) both comprise hydrogen bond accepting carbonyl moieties and that polyethylene oxide (PEO) comprises the hydrogen bond accepting ether moieties. Polyvinyl alcohol (PVA) is the only polymer which comprises hydrogen bond donating hydroxyl moieties, without any hydrogen bond accepting groups.

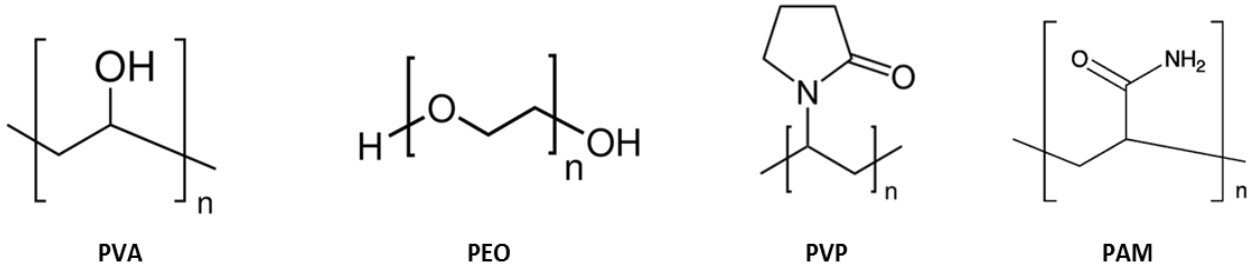

Figure 6.4 Non-ionogenic polymers blended with TMC and tested for mycobacterial affinity.

PVA may thus be categorized as being less chemically inert, as it is the only polymer which does not satisfy all of the points mentioned above for the determination of chemically unreactive substrates. PVA is therefore regarded as being the most facilitative of cellular adhesion, when compared to any other non-ionogenic polymer forming part of this study. This theory supports the findings conducted during the affinity studies of the various chitosan based non-ionogenic polymer blended nanofibers and BCG.

6.2.2 Part Two – SPMNs and nanocomposite materials

The modified chitosan coated superparamagnetic magnetite nanoparticles (SPMN nanocomposites) were tested for their affinity towards mycobacteria. The synthesis and characterization of TMC SPMNs, HTCC SPMNs, CS-qC_8 SPMNs, CS-qC_{10} SPMNs and CS-qC_{12} SPMNs are detailed in Chapter 4.

a) Affinity Studies

A specific mass (50 mg) of pristine SPMNs and polymer coated SPMNs was added to a specific volume (5 mL) of BCG culture and incubated at 37 °C for 30 min, with agitation. The SPMNs and SPMN nanocomposites were subsequently washed twice with PBS (10 min) so as to remove any loosely adhering or residual mycobacteria not properly captured by the SPMN nanocomposites. This was achieved efficiently by means of magnetic decantation, using a 0.35 T permanent magnet. In this way, the residual BCG culture could be removed from the tube, leaving behind the magnetically adhering nanoparticles held in place by magnetic force. The use of controlled magnetization (superparamagnetism) is a convenient way to attract, immobilize and transfer pathogenic species and bacteria easily, provided there exists an affinity for that species.

The various SPMNs were initially analysed in the uncrosslinked state, but subsequent FM analyses showed discrepancies between the FM and LM images of the polymer coated nanoparticles, possibly indicating dissolution of the polymer coating within the aqueous and physiological media

(Addendum E.1). This deduction was validated through the analysis of the polymer coating via thermogravimetric analysis (TGA), found in Addendum E.2. The TGA weight loss curves revealed a 1.1% loss in polymer coating after nanoparticles were dispersed in water for 1 h and a 3.2% loss after 24 h. The SPMNs were then synthesized with the additional step of crosslinking, as described in the experimental section of Chapter 4.

b) Autofluorescence of SPMN nanocomposites

FM was used to analyse the interaction between the modified chitosan SPMNs and mycobacteria. Commonly used stains used to visualise bacteria were found to be inadequate in successfully visualising BCG on the polymer coated SPMNs. Among the stains tested were propidium iodide and SYTO-9, 4',6-diamidino-2-phenylindole (DAPI), Hoechst, 6-aminofluorescein and carboxyfluorescein diacetate succinimidyl ester (CFDA-SE). It was presumed that the various chitosan derivatives were reacting with the stains via amine linking of the polysaccharide to the amino and carbonyl groups of the stains, thereby producing overall fluorescence and ineffective characterization of the mycobacteria captured with the modified chitosan coated SPMNs. It was later revealed, however, that the polymer coated SPMNs were in fact autofluorescent in nature, thus able to naturally absorb photons causing a transition to a higher energy electronic state and then being able to emit those photons to the initial state in $<10^{-9}$ seconds.[27] This deduction was made by analysing non-stained samples without bacteria. The observation occurred to a larger extent for CS-qC_8, CS-qC_{10} and CS-qC_{12} coated SPMNs and to a lesser extent for TMC and HTCC coated SPMNs. The phenomenon is exemplified in Figure 6.5, where CS-qC_{12} SPMNs were stained with propidium iodide and SYTO-9. A small colony of BCG is observed in the centre of the FM image, but overall fluorescence emission is too intense to draw a deduction as to the presence of bacteria, especially that of viable bacteria emitting green fluorescence when stained with SYTO-9.

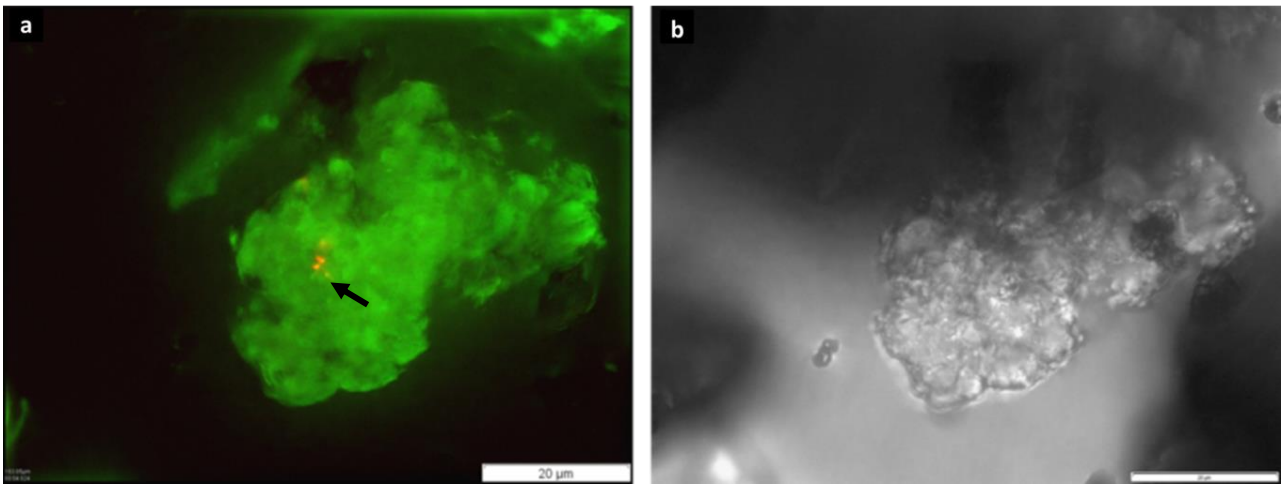

Figure 6.5 (a) FM image and (b) LM image of CS-qC_{12} SPMNs incubated with BCG (10^6 BCG/mL) at 37 °C.

The autofluorescent nature of the polymer coated SPMNs can be attributed to the crosslinking of the amine moiety of the cationic polymers with glutaraldehyde. This provided structural integrity and involved the formation of an autofluorescent $n-\pi^*$ transition chemical bond. Fluorescent Schiff base bonds (C=N) and double bonds (C=C) could therefore have been produced simultaneously by crosslinking the cationic polymer with monomeric glutaraldehyde.[27]

c) Fluorescent reporter strain of BCG

To circumvent the difficulty posed by autofluorescence, a reporter BCG strain was made to express the fluorescent protein, mCherry, constitutively in order to enable the visualization of individually fluorescing mycobacteria. This approach proved successful, as evidenced in Figure 6.6, where the mycobacteria are clearly observed as the red rod-like structures. The red- and blue-channels were overlaid to produce an FM image exhibiting the SPMN nanocomposites as the purple background, which could be achieved due to the wide range of wavelengths over which SPMN nanocomposites emitted autofluorescence.

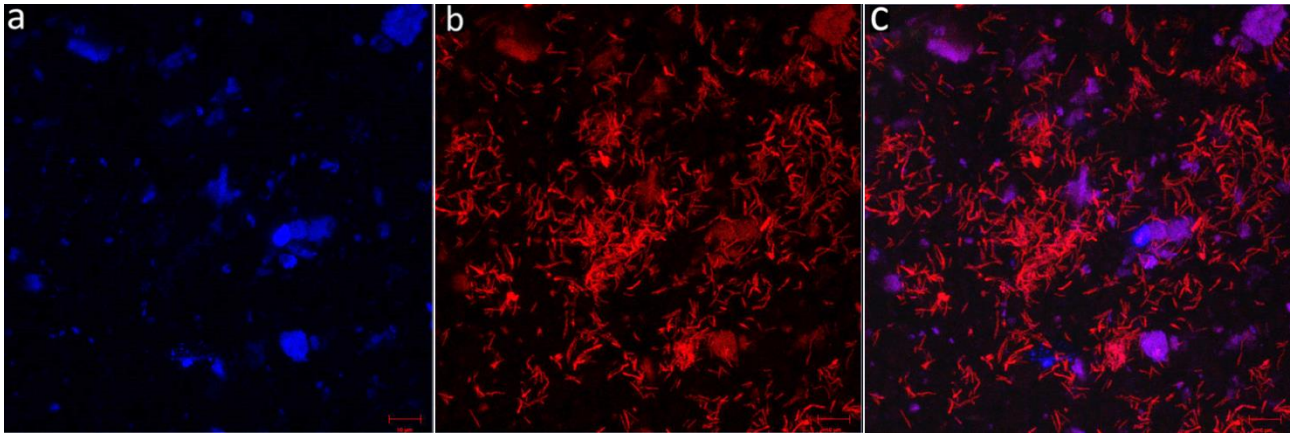

Figure 6.6 Split Image of (a) blue filter emission, (b) red filter emission and (c) overlay of red- and blue-channels obtained via confocal fluorescence microscopy for CS-qC$_{12}$ SPMNs incubated with BCG at 10^8 BCG/mL.

A relative comparison of the mean fluorescence intensities of mCherry expressing BCG (BCG-mCherry) was drawn for the various modified chitosan coated SPMNs. Uncoated SPMNs were incubated with BCG as negative controls and emitted no fluorescence and hence captured no mycobacteria without the polymeric coating. The negative controls of each SPMN nanocomposite were also analysed for inexplicable fluorescence and none was found (Addendum F). CS-qC$_{12}$ SPMNs were found to capture the BCG-mCherry the most efficiently, as it was observed to have the greatest relative mean fluorescence intensity of all SPMN nanocomposites tested. The chemical structures of polymers which coated the SPMNs are reiterated in Figure 6.7.

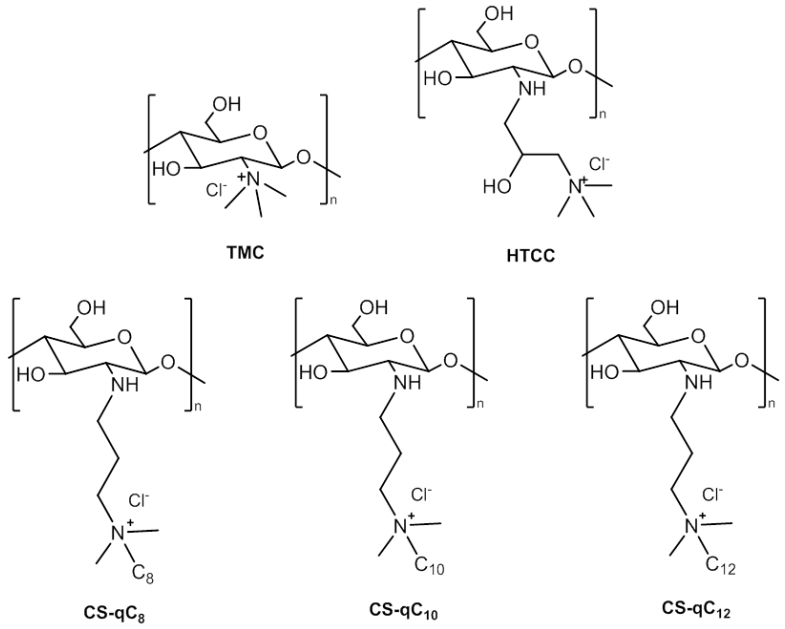

Figure 6.7 Quaternized chitosan derivatives tested for mycobacterial affinity.

A trend in the mycobacterial capture was observed; as the alkyl chain length substitution increased from an 8-carbon chain to a 12-carbon chain so too did the quantity of captured BCG (CS-qC_8 SPMNs < CS-qC_{10} SPMNs < CS-qC_{12} SPMNs) with CS-qC_{12} SPMNs exhibiting the highest quantity of captured BCG. TMC SPMNs were able to capture more mycobacteria than HTCC SPMNs, but not as much as the CS-qC_{12} SPMNs. This could be attributed to the pronounced hydrophilicity of HTCC which comprises hydroxyl moieties able to form hydrogen bonds with water molecules, compared to that of TMC which is more hydrophobic.

Dispersion studies were also conducted in the physiological fluid, as demonstrated in Figure 6.8, where greater or lesser dispersion was observed for the various SPMN nanocomposites after the 30 min period of incubation with BCG.

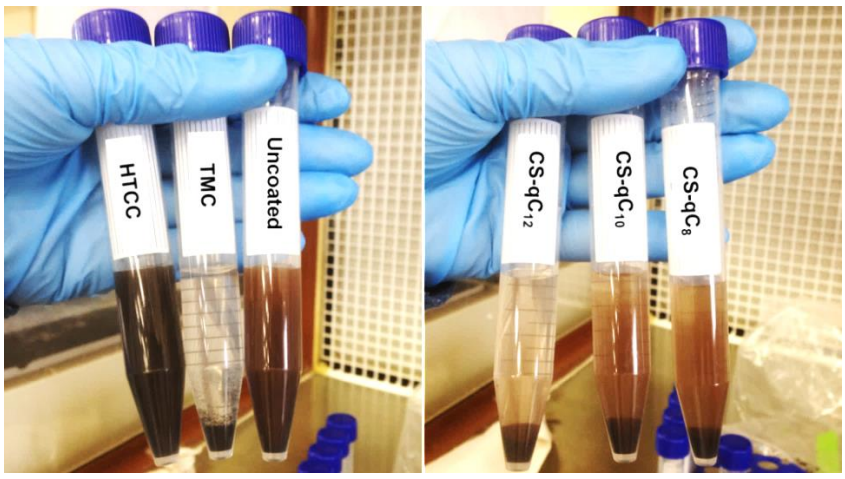

Figure 6.8 Dispersion of SPMN nanocomposites in aqueous media.

The dispersion states of nanoparticles have been proven to influence the ensuing cellular interaction and response.[27] It has been established that a higher hydrophobicity of the surface of a particle leads to greater interaction of that particle with a bacterium having a hydrophobic cell wall. When two hydrophobic molecules collide with each other they increase the entropy and although there is no force of attraction between the hydrophobic molecules, they will associate with each other by hydrophobic-hydrophobic interaction and expel water molecules.[29,30] BCG has a largely hydrophobic cell wall, which could in part account for the stronger interaction of the bacterium with the more hydrophobic (less dispersed) polymer coated SPMNs of CS-qC_{12} and TMC.

These results are derived from the FM images presented in Figure 6.9 and 6.10, where the modified chitosan coated SPMN nanocomposites were incubated with BCG-mCherry at concentrations of 10^8 and 10^7 BCG/mL, respectively, washed twice with PBS and kept at 4 °C for further analysis, which commenced in under 24 h. *M. tuberculosis* and *M. bovis* BCG are slow growing mycobacteria, limiting the risk of mycobacterial multiplication on the substrate after the initial capture.[31]

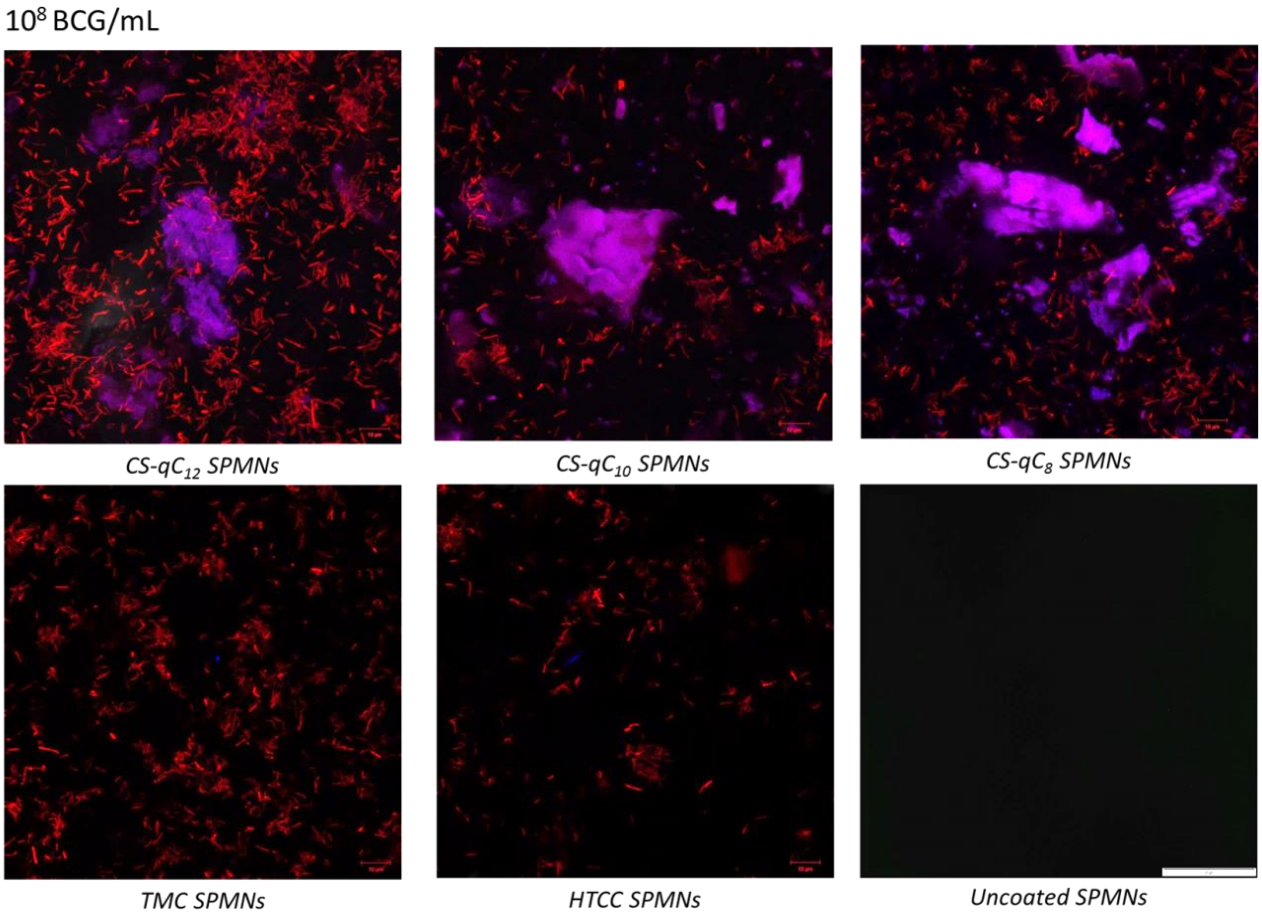

Figure 6.9 FM images of modified chitosan coated SPMNs incubated with BCG at a concentration of 10^8 BCG/mL. The red rod-like structures are the mCherry expressing bacteria (BCG) and the purple structures are as a result of the autofluorescence of specifically modified chitosan coated SPMNs.

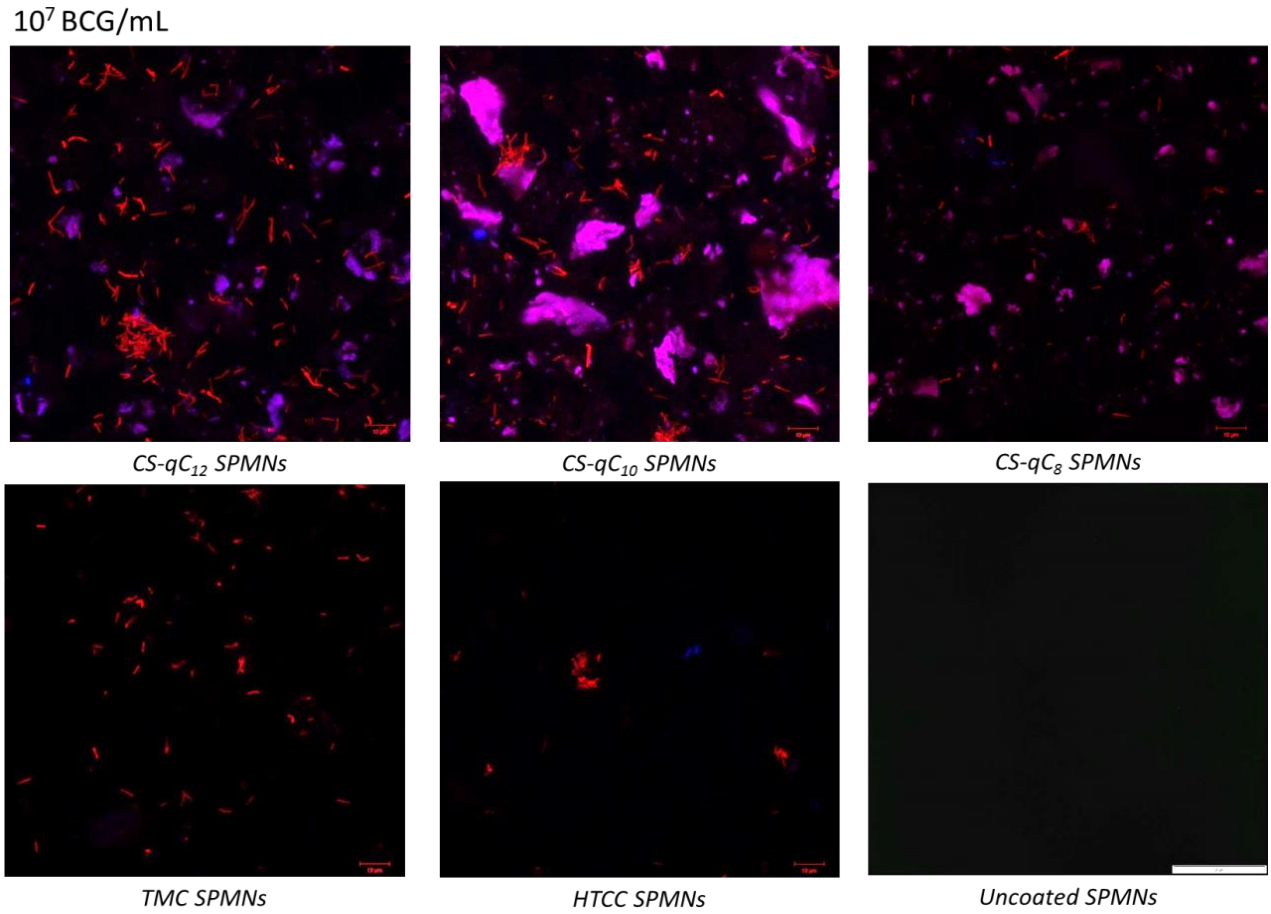

Figure 6.10 FM images of modified chitosan coated SPMNs incubated with BCG at a concentration of 10^7 BCG/mL. The red rod-like structures are the mCherry expressing bacteria (BCG) and the purple structures are as a result of the autofluorescence of specifically modified chitosan coated SPMNs.

As the previous affinity studies indicated that the CS-qC$_{12}$ SPMNs capture BCG the most efficiently, ten-fold serial dilutions were prepared to a final volume of 5 mL per sample from the original concentration of bacteria so as to determine the minimum concentration that CS-qC$_{12}$ SPMNs could capture mycobacteria. The results showed that mycobacteria could be detected at a level as low as 10^3 BCG/mL, the FM images of which can be found in Addendum G.

Analysis of the FM images also indicated that the sensitivity of the modified chitosan SPMN nanocomposites is lower than that of modified chitosan nanofibers. The SPMN nanocomposites could possibly exhibit weaker ionic strength and thus lesser interaction with mycobacteria as a result of the binding of modified chitosan's ammonium ion groups to the hydroxyl groups at the periphery of the SPMN core. It is also possible that the crosslinking agent (glutaraldehyde) possibly inhibited the mycobacterial adhesion of these SPMN nanocomposites to BCG.

d) Interaction of SPMN nanocomposites with mycobacteria

Transmission electron microscopy (TEM) and field emission scanning electron microscopy (FE-SEM) were used as characterization techniques to observe the physical adhesion of the SPMN nanocomposites to mycobacteria, after thorough washing with PBS to remove any unbound, residual mycobacteria.

i) TEM

CS-qC_8 SPMNs and CS-qC_{12} SPMNs were selected and compared for mycobacterial interaction by TEM analysis at an intermediate concentration of 10^6 BCG/mL for both SPMN samples. The nanocomposite SPMNs underwent identical sample preparation steps and were analysed 24 h after incubation with BCG, followed by washing steps and ambient drying. The dried samples (5 mg) were redispersed in 5 mL distilled water before TEM analysis. The TEM images are presented in Figure 6.11 and 6.12.

CS-qC_8 SPMNs

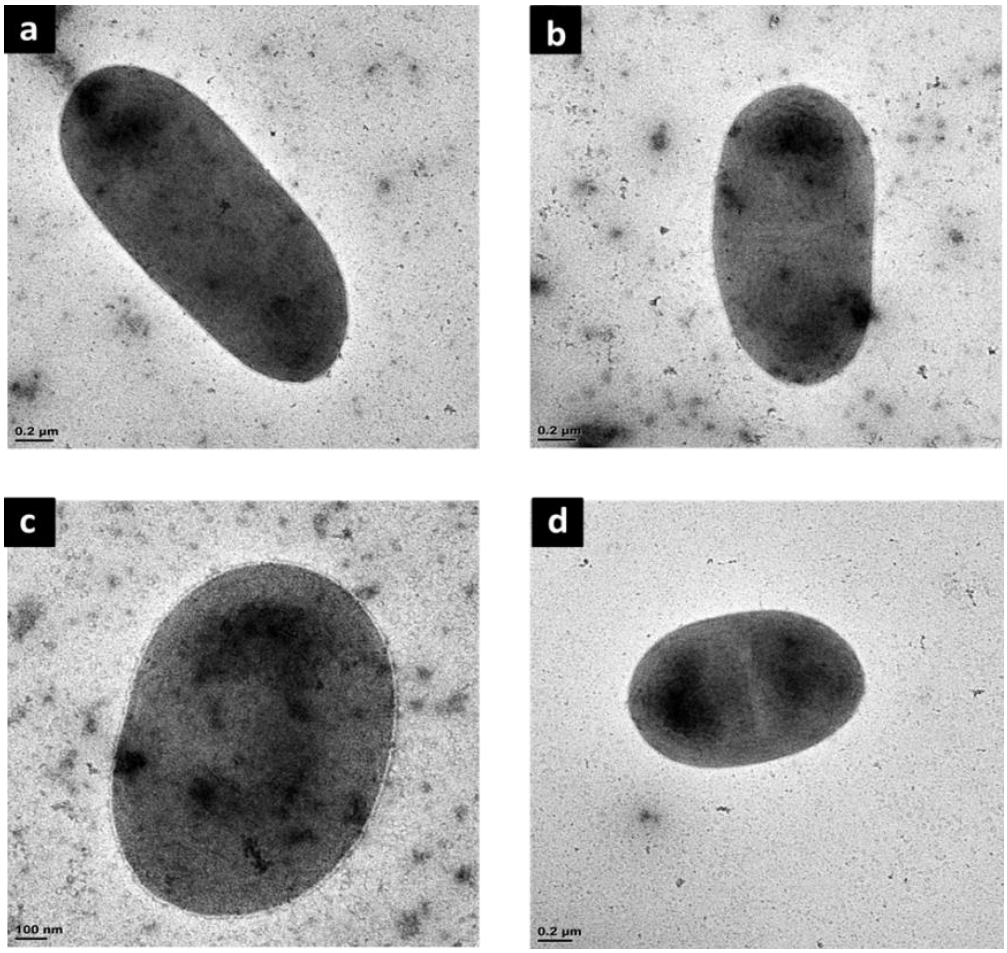

Figure 6.11 TEM images of washed CS-qC_8 SPMNs incubated with BCG at a concentration of 10^6 BCG/mL and subsequently dried under ambient conditions.

CS-qC$_{12}$ SPMNs

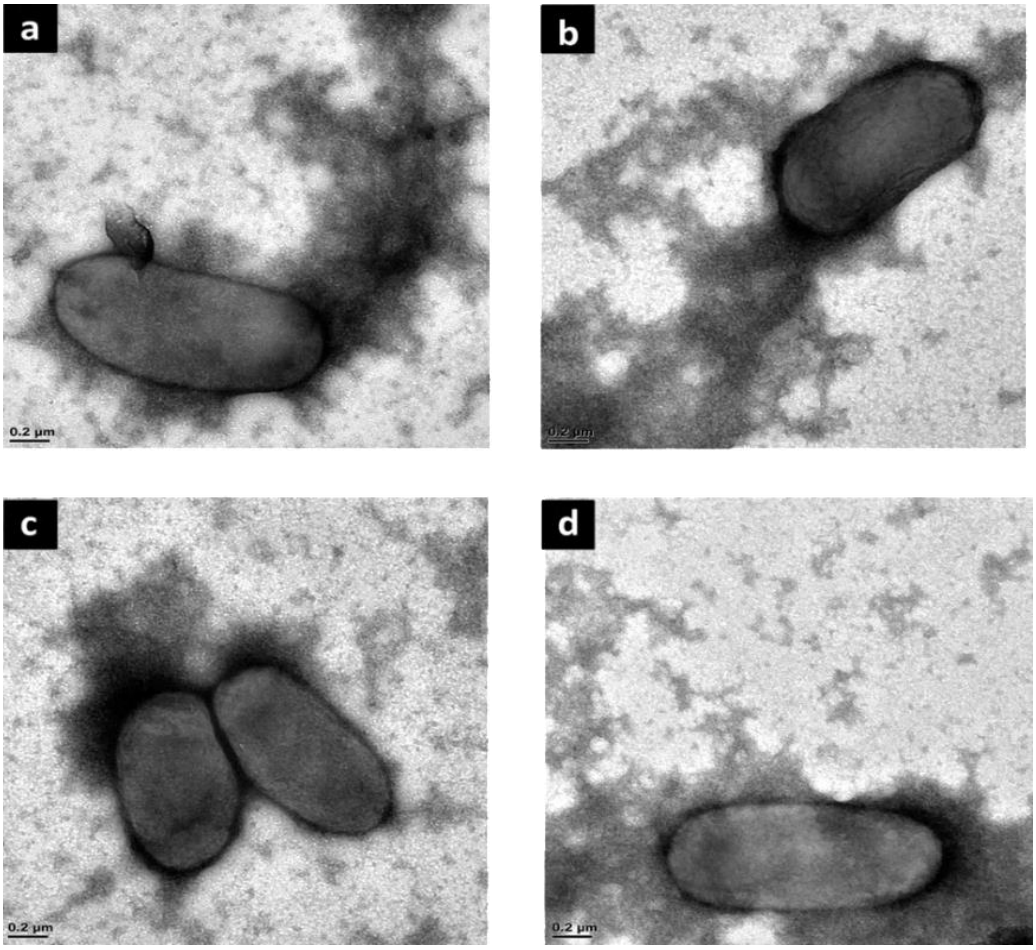

Figure 6.12 TEM images of washed CS-qC$_{12}$ SPMNs incubated with BCG at a concentration of 10^6 BCG/mL and subsequently dried under ambient conditions.

BCG is reported to have an average diameter of 2 – 4 μm in length, and is observed as the larger rod-shaped mass in the TEM images. The darker areas of the TEM images in Figure 6.11 and 6.12 are indicative of the polymer coated SPMNs as the surrounding nanoparticles have consistent average diameters as compared to the negative controls (nanoparticles dispersed in culture medium and PBS, without BCG).

A larger density of SPMNs surrounding the mycobacteria is observed for CS-qC$_{12}$ SPMNs, as compared to that of CS-qC$_8$ SPMNs. These results are in good agreement with those obtained via fluorescence microscopy. It appears as if the cell wall of the mycobacterium observed in Figure 6.11 (a) has been destabilized, causing leakage of intracellular substances, likely due to the electrostatic interaction which occurs as a result of the cationic modified chitosan layer surrounding the SPMN and the anionic phospholipid layer of the mycobacterium.[31]

It is uncertain whether the nanoparticles are attached to the outer cell membrane of the mycobacteria or whether they have penetrated the cell wall. The internalization of modified nanoparticles through endocytosis (the process of uptake of macromolecules into cells by enclosing them in membrane vesicles) upon contact with the cell membrane is reported in literature and could possibly occur through a variety of mechanisms, as reviewed by Verma *et al*.[32]

TEM analysis revealed an interesting phenomenon of cell reproduction by binary fission. A sample of nanocomposite SPMNs (CS-qC_{12} SPMNs) was analysed by TEM 10 days after incubation with BCG. The SPMNs observed in Figure 6.13 were dried and stored in an airtight polytop at room temperature after incubation and wash steps. The fact that BCG was able to reproduce in such an environment is confirmation of its complex layered cell wall which profoundly influences its resilience against environmental stresses and allows it to inhabit various environmental reservoirs.[33] The mycobacterial cell wall contains large quantities of lipids, causing higher hydrophobicity in comparison with other bacteria which make them impermeable and resistant to immunological systems.[10] Most known rod-shaped bacteria grow along their axes and divide by binary fission, which is a type of asexual reproduction that leads to the production of genetically identical offspring. Cell division occurs by formation of a division septum at the midcell region (refer to Figure 6.13 (b)) after chromosome replication has been completed and the two daughter chromosomes have segregated into two halves within the cell.[34]

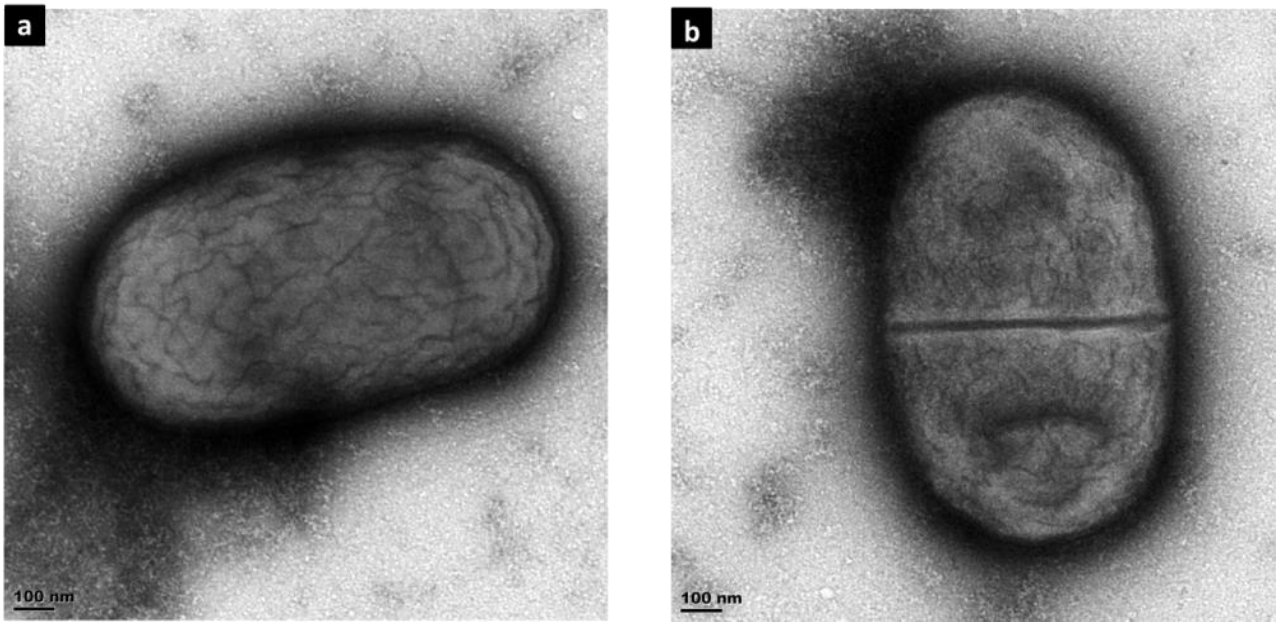

Figure 6.13 TEM image of (a) M. bovis BCG and (b) M. bovis BCG undergoing binary fission.

ii) FE-SEM

After FM revealed the most efficient capture of mycobacteria via CS-qC$_{12}$ SPMNs, these nanoparticles were chosen as representative SPMN nanocomposites for the visualization of mycobacteria via field emission scanning electron analysis. Figure 6.14 shows the CS-qC$_{12}$ SPMNs which serve as the negative control. The nanoparticles were treated to the same conditional environment that the pathogen-incubated nanoparticles were treated to (dispersion in the liquid growth medium and phosphate buffer solution), but with the exclusion of BCG.

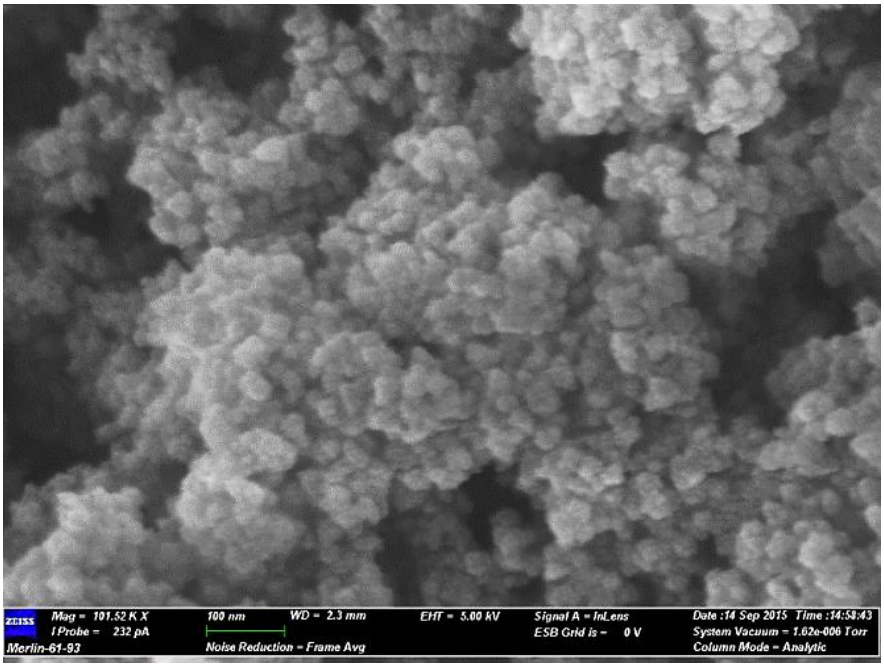

Figure 6.14 FE-SEM image of CS-qC12 SPMNs dispersed in 7H9 growth medium and PBS, and subsequently dried under ambient conditions, as negative control.

Compared to conventional SEM, field emission SEM was able to provide topographical and elemental information at high magnifications, with virtually unlimited depth of field. The nanoparticles analysed via FE-SEM had an average diameter of 10.3 $\pm$ 1.2 nm, which is comparable to the diameter estimations by other characterization techniques. The SPMNs further conformed into nanosized spheres of diameter 32.3 $\pm$ 0.8 nm. It is not unforeseeable that these nanoclusters would form upon ambient drying from PBS and culture medium solution. It is most likely as a result of the stabilization of intermolecular forces resulting from the affinity studies undertaken with BCG in physiological fluids. Figure 6.15 and Figure 6.16 clearly indicate the adhesion of mycobacteria to the modified chitosan coated SPMNs.

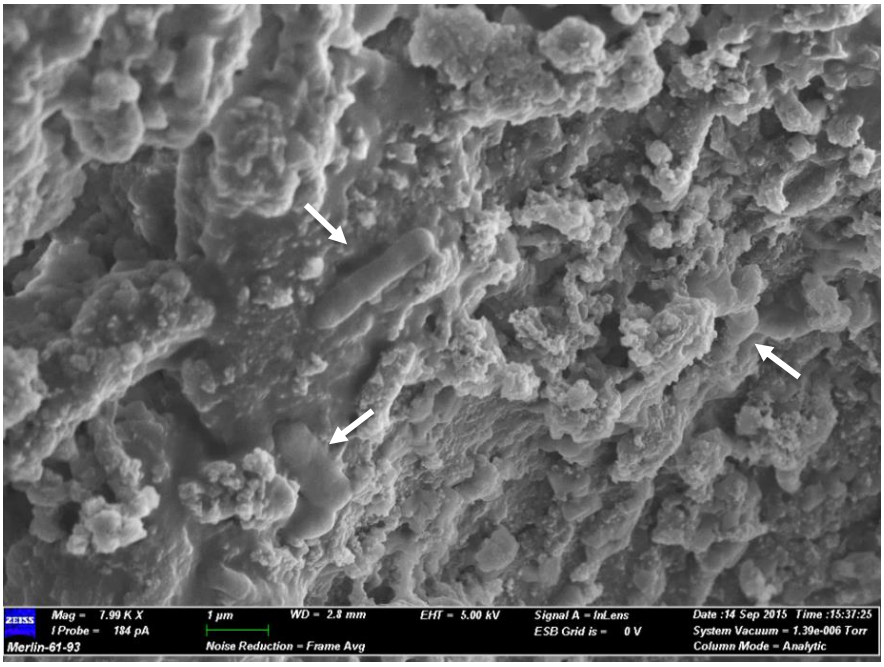

Figure 6.15 FE-SEM image of washed CS-qC$_{12}$ SPMNs incubated with BCG at a concentration of 10^{8} BCG/mL for 30 min, and subsequently dried under ambient conditions. The rod-like structures, some of which are indicated with arrows, are the mycobacteria.

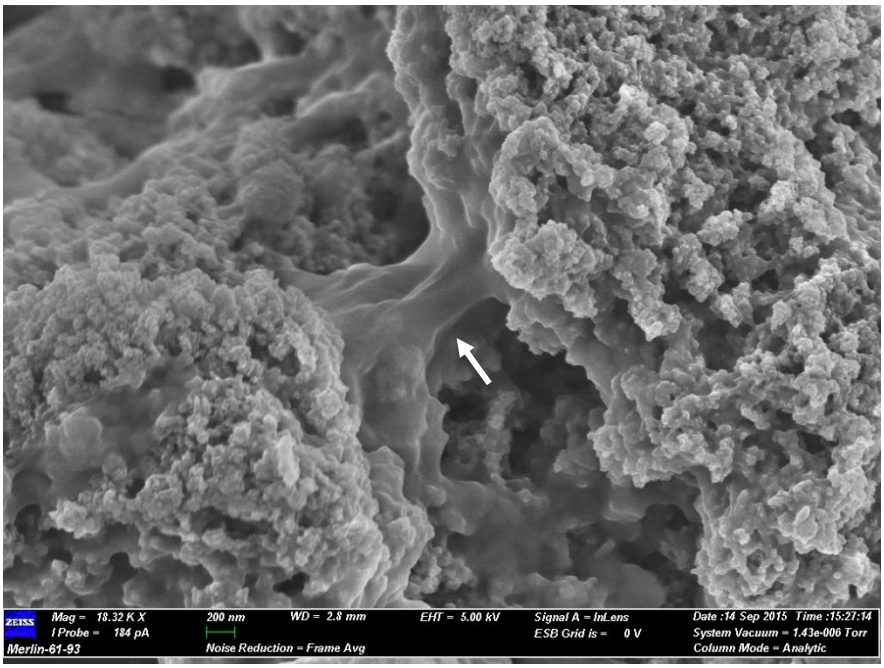

Figure 6.16 FE-SEM image of washed CS-qC$_{12}$ SPMNs incubated with BCG at a concentration of 10^{7} BCG/mL for 30 min, and subsequently dried under ambient conditions. The rod-like structures adjoining the clusters of nanoparticles are indicated by the arrow as a mycobacterial colony of BCG.

6.3 Conclusion

BCG was used as a non-pathogenic *M. tuberculosis*-mimic, and was successfully captured onto the surfaces of modified chitosan/non-ionogenic polymer nanofibers and modified chitosan coated superparamagnetic magnetite nanoparticles. The polymers used to create the nano-substrates were derived from chitosan and were modified to possess a quaternary ammonium group and various lengths of aliphatic chains, or methyl groups with or without a hydroxyl moiety.

The nanofibers electrospun from a blend of polyvinyl alcohol and *N*-trimethylammonium chitosan chloride (PVA/TMC) were observed via FM and LM to capture the mycobacteria most efficiently, with a sensitivity of 10 BCG/mL. The substrate conditions for chemical inertness aid the elucidation of this finding. PVA satisfies the criterion of having hydrogen bond donating groups yet not having hydrogen bond accepting groups, of which PVP, PAM and PEO do not satisfy. Furthermore, the PVA/TMC nanofibers which were crosslinked with genipin exhibited greater capture efficiency as opposed to those crosslinked with glutaraldehyde vapour. This could be attributed to the higher degree of swelling in aqueous media for genipin crosslinked PVA/TMC nanofibers.

The various SPMN nanocomposites were tested for their affinity towards mycobacteria. The challenges which accompany autofluorescence were overcome through the use of a BCG strain expressing the fluorescent protein mCherry. CS-qC_{12} SPMNs were observed to capture mycobacteria most efficiently, with good results being obtained for TMC SPMNs. The sensitivity of CS-qC_{12} coated SPMNs was 10^3 BCG/mL.

Based on these results it may be concluded that BCG was captured onto the modified chitosan nano-substrates through ionic interaction between the negatively charged BCG cell wall and the positively charged quaternary ammonium moiety of modified chitosan, as well as through hydrophobic-hydrophobic interaction between the mycolic acids of the BCG cell wall and the aliphatic C_{12} hydrocarbon chain, or the three methyl groups of the modified polymer.

6.4 Experimental

6.4.1 Characterization Techniques

a) Field emission scanning electron microscopy (FE-SEM)

Images of the nanoparticles were obtained using a MERLIN FE-SEM microscope. The sample fibers on aluminum foil were cut into approximately 1 cm^2 squares and attached onto the SEM stub with double sided carbon tape. Alternatively, a 1 μL droplet of SPMN fluid dispersed in PBS was

placed onto the SEM stub with double sided carbon tape and was left to dry in ambient conditions. The SEM stubs were then sputter coated with gold under vacuum prior to imaging.

b) Transmission electron microscopy (TEM)

Nanoparticle and mycobacteria interaction was visualised via TEM, using a JEM 1200EXII model (JEOL, Japan) microscope. In general, an accelerated voltage of 120 kV was used throughout. A drop of PBS suspended SPMN nanocomposite sample was placed on a carbon-coated 200 mesh copper grid, followed by drying at ambient conditions before it was attached to the sample holder on the microscope. The mean diameter and size-distribution was determined by measuring more than 100 particles from TEM images using *SEM IMAGE STUDIO,* a public domain image processing program.[35]

c) Fluorescence microscopy (FM)

Images of the modified chitosan nanofibers were obtained using an Olympus IX-81 microscope, coupled to an MT-20 Xenon burner. The samples were placed on a microscope slide and incubated with SYTO-9 nucleic acid and propidium iodide for 15 minutes. The samples were excited using a Xenon-Arc burner (Olympus Biosystems GMBH) as light source, with 472 nm or 572 nm excitation filter. Emission was collected using a UBG triple-bandpass emission filter cube. Transmission images were obtained in the same scan. Confocal microscopy was utilized additionally.

Images of the modified chitosan coated SPMNs were obtained using a Zeiss LSM 880 confocal microscope with ZEN 2 software, coupled to an Argon multiline laser. There was no need for sample preparation. For excitation of mCherry fluorescence, an argon laser with an excitation wavelength of 543 nm was used, with a GaAsP detector 32+2 PMT. Transmission images were obtained in the same scan with a transmitted light detector T-PMT.

6.4.2 Experimental procedures

a) Culture

One mL BCG (containing pJV 75 Amber) freezer stock was inoculated in 10 mL Middlebrook 7H9 medium containing 0.2% glycerol, 0.05% Tween-80, 10% ADC and 25 µg/ml kanamycin and grown to an optical density of 0.78, when measured at 600 nm in a spectrophotometer (OD_{600nm}). The cells were pelleted by centrifugation at 3000 x g for 10 minutes at 4 °C and resuspended in 10 mL Middlebrook 7H9 medium containing 0.2% glycerol and 10% ADC and 0.05% Tween-80.

The centrifugation and resuspension steps were repeated. The cells were inoculated to approximate OD_{600nm} of 0.05 in 7H9 medium containing 0.2% glycerol, 10% ADC, 25 µg/mL kanamycin and 0.05% Tween-80 (50-100 mL cultures) and grown to approximate OD_{600nm} of 0.8-1.

M. bovis BCG expressing mCherry (Nordic BioSite) was inoculated into 5 ml Sauton's medium containing 30 ug/ml kanamycin and grown to an optical density OD_{600nm} of 0.8-1 at 37 °C. The culture was subsequently used to inoculate 20 ml Sauton's medium (OD_{600nm} = 0.05) and further incubated at 37 °C until the culture reached an OD_{600nm} of 0.8-1.

b) Affinity Studies

i) Nanofibers

A 5 mL aliquot of BCG culture dispersion (pH ~ 7) was pipetted into a tube with a screw lid. A 10 mg piece of modified nanofibrous mat was added to the BCG culture in the tube, taking care to ensure that the polymer did not adhere to the side of the tube and was moving freely in the culture. The tube was closed and incubated at 37 °C for 30 min, with agitation. A tube with PBS and 7H9 growth medium, instead of BCG culture, was included as negative control. The polymer mat was subsequently removed and washed twice in PBS for 10 min and returned to a clean eppendorf tube.

ii) Nanoparticles

A 5 mL aliquot of BCG culture dispersion (pH ~ 7) was pipetted into a tube with a screw lid. A mass of 50 mg of SPMNs was added to the BCG culture in the tube. The tube was closed and incubated at 37 °C for 30 min, with agitation. A tube with PBS and 7H9 growth medium, instead of BCG culture, was included as a negative control. The BCG was subsequently removed via magnetic decantation and the nanoparticles were washed twice in PBS for 10 minutes and returned to a clean eppendorf tube.

6.5 References

1. Katsikogianni, M.; Missirlis, Y. *Eur. Cell Mater.* **2004***, 3,*.

2. Esin, S.; Counoupas, C.; Aulicino, A.; Brancatisano, F.; Maisetta, G.; Bottai, D.; Luca, M.; Florio, W.; Campa, M.; Batoni, G. *Scand. J. Immunol.* **2013***, 6,* 460-469.

3. Alsteens, D.; Verbelen, C.; Dague, E.; Raze, D.; Baulard, A. R.; Dufrêne, Y. F. *Pflügers Archiv. Eur. J. Phys.* **2008***, 1,* 117-125.

4. Van der Geize, R.; Yam, K.; Heuser, T.; Wilbrink, M. H.; Hara, H.; Anderton, M. C.; Sim, E.; Dijkhuizen, L.; Davies, J. E.; Mohn, W. W. *P. Nat. A. Sci.* **2007***, 6,* 1947-1952.

5. *Cole, S.; Brosch, R.; Parkhill, J.; Garnier, T.; Churcher, C.; Harris, D.; Gordon, S.; Eiglmeier, K.; Gas, S.; Barry, C. Nature* ***1998****, 6685, 537-544.*

6. Thomas, S. T.; VanderVen, B. C.; Sherman, D. R.; Russell, D. G.; Sampson, N. S. *J. Biol. Chem.* **2011***, 51,* 43668-43678.

7. Cronje, L. *Surface modification of styrene maleic anhydride nanofibers for efficient capture of Mycobacterium tuberculosis,* Phd Thesis, Stellenbosch University, **2012**.

8. Daffe, M.; Brennan, P. J.; McNeil, M. *J. Biol. Chem.* **1990***, 12,* 6734-6743.

9. Hahn, F.; E. Mechanism of Action of Antibacterial Agents*; Springer,* **1979***.*

10. RamanáSuri, C. *Chem. Comm.* **2010***, 31,* 5755-5757.

11. Ostuni, E.; Chapman, R. G.; Liang, M. N.; Meluleni, G.; Pier, G.; Ingber, D. E.; Whitesides, G. M. *Langmuir* **2001***, 20,* 6336-6343.

12. Tiller, J. C.; Liao, C. J.; Lewis, K.; Klibanov, A. M. *Proc. Natl. Acad. Sci. U. S. A.* **2001***, 11,* 5981-5985.

13. Buffet-Bataillon, S.; Tattevin, P.; Bonnaure-Mallet, M.; Jolivet-Gougeon, A. *Int. J. Antimicrob. Agents* **2012***, 5,* 381-389.

14. Lu, G.; Wu, D.; Fu, R. *React Funct Polym.* **2007***, 4,* 355-366.

15. Chen, C. Z.; Beck-Tan, N. C.; Dhurjati, P.; van Dyk, T. K.; LaRossa, R. A.; Cooper, S. L. *Biomacromolecules* **2000***, 3,* 473-480.

16. Wong, S. Y.; Moskowitz, J. S.; Veselinovic, J.; Rosario, R. A.; Timachova, K.; Blaisse, M. R.; Fuller, R. C.; Klibanov, A. M.; Hammond, P. T. *J. Am. Chem. Soc.* **2010***, 50,* 17840-17848.

17. Mahairas, G. G.; Sabo, P. J.; Hickey, M. J.; Singh, D. C.; Stover, C. K. *J. Bacteriol.* **1996***, 5,* 1274-1282.

18. Baena-Ruano, S.; Jiménez-Ot, C.; Santos-Dueñas, I.; Cantero-Moreno, D.; Barja, F.; García-García, I. *Process Biochemistry* **2006***, 5,* 1160-1164.

19. Kong, M.; Chen, X. G.; Xing, K.; Park, H. J. *Int. J. Food Microbiol.* **2010***, 1,* 51-63.

20. Gilbert, P.; Moore, L. *J. Appl. Microbiol.* **2005***, 4,* 703-715.

21. Chen, C. Z.; Cooper, S. L. *Biomaterials* **2002***, 16,* 3359-3368.

22. Tan, H.; Ma, R.; Lin, C.; Liu, Z.; Tang, T. *Int. J. Mol. Sci.* **2013***, 1,* 1854-1869.

23. McDonnell, G.; Russell, A. D. *Clin. Microbiol. Rev.* **1999***, 1,* 147-179.

24. Chapman, R. G.; Ostuni, E.; Liang, M. N.; Meluleni, G.; Kim, E.; Yan, L.; Pier, G.; Warren, H. S.; Whitesides, G. M. *Langmuir* **2001***, 4,* 1225-1233.

25. Chen, S.; Zheng, J.; Li, L.; Jiang, S. *J. Am. Chem. Soc.* **2005***, 41,* 14473-14478.

26. Lakowicz, J. R. *Principles of fluorescence spectroscopy;* Springer, **2013**.

27. Cole, S.; Brosch, R.; Parkhill, J.; Garnier, T.; Churcher, C.; Harris, D.; Gordon, S.; Eiglmeier, K.; Gas, S.; Barry, C. *Nature* **1998***, 6685,* 537-544.

28. Moore, T. L.; Rodriguez-Lorenzo, L.; Hirsch, V.; Balog, S.; Urban, D.; Jud, C.; Rothen-Rutishauser, B.; Lattuada, M.; Petri-Fink, A. *Chem. Soc. Rev.* **2015***, 17,* 6287-6305.

29. Curtis, R.; Steinbrecher, C.; Heinemann, M.; Blanch, H.; Prausnitz, J. *Biophys. Chem.* **2002***, 3,* 249-265.

30. Hjertén, S.; Wadström, T. *Pathogenesis of Wound and Biomaterial-Associated Infections;* Springer, **1990**, 245-253.

31. Zhao, H.; Xu, J.; Dong, P.; Luo, G. *Chem. Eng. J.* **2013**, 784-790.

32. Verma, A.; Stellacci, F. *Small* **2010***, 1,* 12-21.

33. Singh, B.; Ghosh, J.; Islam, N. M.; Dasgupta, S.; Kirsebom, L. A. *A. Van Leeuw.* **2010***, 2,* 165-177.

34. Harry, E.; Rodwell, J.; Wake, R. *Mol. Microbiol.* **1999***, 1,* 33-40.

35. W. Rasband, *In Image J*: Image processing and analysis in java http://rsb.info.nih.gov/ij/, **2006**.

Chapter Seven

Conclusions and Recommendations

7.1 Conclusions

The synthesis and characterization of a variety of modified chitosan polymers, which were electrospun into nanofibers and which were used to coat superparamagnetic magnetite nanoparticles, were presented in this thesis. The modified chitosan based nano-substrates were evaluated as modes of capture for the bacillus Calmette-Guérin (BCG) strain of *Mycobacterium bovis*. *Mycobacterium tuberculosis (M. tuberculosis)* is a pathogenic bacterial species and hence BCG was used as the attenuated (virulence-reduced) *M. tuberculosis*-mimic bacteria.

7.1.1 Polymer Modification

Chitosan was modified with a variety of compounds to yield quaternized derivatives of permanent cationic charge through the introduction of quaternary ammonium moieties. The derivatization of the 2-amino-2-deoxy-β-d-glycopyranose (GlcN) residue of chitosan, at the C-2 position bearing amino functionality increased the solubility of chitosan at neutral and alkaline pH values, allowing for processes and analyses to take place in aqueous media. The derivatives of chitosan were synthesized based on possible chemical interaction with BCG and hence the *M. tuberculosis* cell wall.

Quaternization of the primary amino groups of chitosan to produce *N*-trimethylammonium chitosan chloride (TMC) was accomplished using methyl iodide in an alkaline solution of *N*-methyl-2-pyrrolidone. The quaternization took place at the primary amino group of chitosan via a nucleophilic substitution reaction with methyl iodide and sodium iodide used as catalysts.

Glycidyltrimethylammonium chloride (GTMAC) was selected as a quaternizing agent due to its inherent quaternary ammonium group to produce *N*-(2-hydroxy)propyl-3-trimethylammonium chitosan chloride (HTCC). The quaternary ammonium group inclusion is obtained after the ring-opening reaction of the primary amino group of chitosan at the C-2 position with GTMAC.

Furthermore, the modification of chitosan via the precursor polymer *N*-substituted chitosan to yield the relevant modified chitosan derivatives, *N*-propyl-3-*N',N'*-dimethyl-*N'*-octylammonium chitosan chloride (CS-qC_8), *N*-propyl-3-*N',N'*-dimethyl-*N'*-decylammonium chitosan chloride (CS-qC_{10}) and *N*-propyl-3-*N',N'*-dimethyl-*N'*-dodecylammonium chitosan chloride (CS-qC_{12}) was also attained. The direct *N*-substitution of chitosan was achieved by the reaction between the primary amino groups of chitosan and (3-bromopropyl)dimethylamine, under heterogeneous conditions in the presence of a strong base. ^{1}H NMR, ^{13}C NMR and ATR-FTIR characterization techniques were used to ascertain the formation of these compounds.

7.1.2 Bi-component nanofibers

TMC was successfully blended with polyethylene oxide (PEO), polyvinyl alcohol (PVA) and polyvinyl pyrrolidone (PVP) and electrospun into polymer nanofibers of diameter 245 $\pm$ 53 nm, 489 $\pm$ 107 nm, 550 $\pm$ 194 nm, respectively. Glutaraldehyde and genipin were explored as crosslinking agents for PVA/TMC nanofibers, with the latter being used in the crosslinking of PEO/TMC nanofibers. PVP/TMC nanofibers were thermally crosslinked. PAM was removed from the study due to the inability of PAM/TMC nanofibers to be efficiently crosslinked, whilst maintaining nanofibrous morphology. Crosslinking is essential for rendering the modified chitosan nanofibers insoluble in water and was crucial for the preservation of the nanofibrous structure when immersed in water for extended periods. Scanning electron microscopy (SEM) was used to analyse the morphology, diameter and size distributions of the electrospun nanofibers. Water contact angle measurements and surface area and porosity analyses were also conducted in order to develop a broader understanding of the morphology and solution behaviour of the chitosan based bi-component nanofibers.

7.1.3 Superparamagnetic magnetite nanoparticles (SPMNs) and SPMN nanocomposites

The SPMNs were produced via the chemical co-precipitation of ferrous (Fe^{2+}) and ferric (Fe^{3+}) ions by a base ($NH_3.H_2O$) in aqueous solution under anaerobic conditions. Anaerobic conditions protect the SPMNs from critical oxidation and limit core growth. The formation of relatively pure and crystalline SPMNs was proven by XRD analysis and the SPMNs were magnetically characterized by SQUID analysis. The SPMNs revealed superparamagnetic behaviour which illustrated zero coercivity and zero remanence on the magnetization curve with a saturation magnetization (M_S) of 34.6 emu/g at 300 K. The surface area analysis results indicated that the SPMNs had mesoporous structures with a very high specific surface area of 505.2 m^2/g.

The synthesized SPMNs were coated with quaternized chitosan derivatives so as to prevent aggregation and to specifically tailor the pristine nanoparticles for chemical interaction with mycobacteria. The SPMN nanocomposites were characterized by transmission electron microscopy (TEM), attenuated total reflectance Fourier transform infrared (ATR-FTIR) spectroscopy, surface area and porosity analyses, energy-dispersive X-ray (EDX) spectroscopy and thermogravimetric analysis (TGA). These served to prove that the modified chitosan polymers had successfully coated the pristine SPMNs. Additionally, a SQUID analysis was conducted for TMC coated SPMNs, which revealed a decrease in the M_S value to 22.7 emu/g compared to the pristine SPMNs. More important to note, however, is that the polymer coated SPMNs maintained superparamagnetic character. The polymer coating enabled stability in aqueous solution and also conferred surface functional groups for interaction with the BCG / *M. tuberculosis* cell wall. The coating of the SPMNs was achieved via a chemical co-precipitation *in situ* coating procedure, where ferrous and ferric ions were chelated by the amino groups of modified chitosan and which provided a nucleation site for magnetite crystal growth. The crystal growth of the core was restricted by the iron ions diffusion, which in turn, was restricted by the chelation effect of chitosan.

7.1.4 Affinity Studies

Affinity studies were conducted between the modified chitosan nano-substrates and BCG, to determine whether the mycobacteria could be captured onto the surface of the chitosan based nanofibers and nanoparticles. Fluorescence microscopy (FM), light microscopy (LM), field emission scanning electron microscopy (FE-SEM) and TEM were used to observe the interaction.

FM images indicated that PVA/TMC nanofibers were able to capture more bacteria than any other bi-component nanofibrous mat. These results may be interpreted by examining the structural characteristics of substrates which are known to be chemically inert: (1) they are hydrophilic, (2) they are overall electrically neutral, (3) they are hydrogen bond acceptors and (4) they are not hydrogen bond donors. Naturally, electrical neutrality is inherent to each non-ionogenic polymer in this study, namely, PVA, PEO, PVP and PAM. The other three criteria were therefore considered. PVA is the only polymer to comprise hydrogen bond donating groups yet not comprise hydrogen bond accepting groups. Additionally, water contact angle measurements revealed that PVA was the least hydrophilic of the non-ionogenic polymers forming part of this study. Therefore, it may be concluded that PVA is the least chemically inert polymer, capable of facilitating the greatest degree of cellular adhesion.

PVA/TMC blend nanofibers crosslinked with genipin were observed to capture BCG more efficiently than those crosslinked with glutaraldehyde. Genipin crosslinked mats caused the swelling of nanofibers when exposed to water vapour, observed via SEM and supported in

literature. This could account for the higher BCG capture efficiency of the PVA/TMC nanofibrous mat crosslinked with genipin over that crosslinked with glutaraldehyde.

Of the SPMN nanocomposites tested for BCG affinity, CS-qC_{12} coated SPMNs exhibited the most efficient capture surface for BCG, which was observed to be greater than that of CS-qC_{10} SPMNs and CS-qC_8 SPMNs, in order of descending aliphatic chain length. TMC SPMNs were able to capture more mycobacteria than HTCC SPMNs. This could be attributed to the pronounced hydrophilicity of HTCC which comprises hydroxyl moieties able to form hydrogen bonds with water molecules, compared to that of TMC which is more hydrophobic. Based on these results it is concluded that BCG can be captured onto the modified chitosan nano-substrates through ionic interaction between the negatively charged BCG cell wall and the positively charged quaternary ammonium moiety of modified chitosan, as well as through hydrophobic-hydrophobic interaction between the mycolic acids of the BCG cell wall and the aliphatic C_{12} hydrocarbon chain, or the three methyl groups of the modified polymer.

The optimum nano-substrate from each substrate group can be compared in terms of mycobacterial sensitivity. PVA/TMC bi-component nanofibers were able to detect mycobacteria at a concentration as low as 10 BCG/mL and CS-qC_{12} coated SPMNs were able to detect mycobacteria at a concentration of 10^3 BCG/mL. This indicated that the modified chitosan nanofibers are more sensitive than the modified chitosan coated magnetite nanoparticles, which is notable due to the fact that only 30 % of the nanofiber sample was made up of the active, cationic polymer compound (TMC) and the other 70 % was the electrically neutral polymer (PVA). The SPMN nanocomposites could possibly exhibit weaker ionic strength and thus interaction with mycobacteria as a result of the binding of modified chitosan's ammonium ion groups to the hydroxyl groups at the periphery of the SPMN core. It is also possible that the crosslinking agent (glutaraldehyde) may have inhibited the mycobacterial adhesion of these SPMN nanocomposites to BCG, as compared to possibly using a different crosslinking agent such as genipin.

The objectives of this study as outlined in Chapter 1 have essentially been met. Therefore, in this thesis, the use of modified chitosan based nanofibers and coated superparamagnetic magnetite nanoparticles as affinity substrates for the successful capture of mycobacteria was explored and evaluated. These modified nano-substrates can be used for the concentration of pathogenic bacteria for early diagnostic tests and preliminary pathogenic screening. Moreover, these nano-substrates can be used to concentrate the bacteria from a smaller specimen volume from a patient infected with TB, which may directly improve the sensitivity of other diagnostic techniques. This procedure may allow for the preliminary analysis of pathogens by studying their morphology via FM, SEM and TEM.

7.2 Recommendations for future research

The results presented in this study indicated, principally, the potential of superparamagnetic nanocomposites modified with a 12-carbon aliphatic chain and quaternary ammonium moiety to be used as a nano-substrate for the separation, concentration and immobilization of bacteria, specifically the pathogen *M. tuberculosis*. The results also indicated towards the higher sensitivity of nanofibers compared to nanoparticles. Polyvinvyl alcohol (PVA) was found to be the best performing non-ionogenic polymer to blend with quaternized chitosan to produce nanofibers of mycobacterial affinity. Future work on nano-substrates is multi-faceted and can be summarised as follows:

In terms of the modified polymer and nano-substrate:

The polymer CS-qC_{12} could be electrospun into polymer nanofibers by blending with PVA. Blend ratios other than 70/30, non-ionogenic polymer/modified chitosan, could be explored as a means to increase the modified chitosan component of the nanofibers.

An interesting result would be in the addition of chitosan coated superparamagnetic nanoparticles into the electrospinning solution of PVA/CS-qC_{12}. The sensitivity of these polymer coated superparamagnetic nanoparticles could possibly be optimized by crosslinking with genipin instead of glutaraldehyde. The modified chitosan coating could possibly overcome some challenges associated with the inclusion of magnetic nanoparticles into electrospun nanofibers, which includes poor dispersion of these nanoparticles in the polymer electrospinning solution. Nano-substrates which are dual-functional, in that they are able to become magnetically responsive and unresponsive when an applied magnetic field is applied and removed, respectively, is a sought after biomedical feature of materials created through nanotechnology.

The carbohydrate binding protein, Concanavilin A (Con A), could be explored as a linker between modified chitosan and *M. tuberculosis*. Recent findings in our research group has indicated towards the strong interaction between electrospun poly(styrene-*co*-maleic anhydride) nanofibers functionalized with Con A and the *M. tuberculosis* cell wall, through BCG capture. Studies have proven that the arabinogalactan isolated from the cell wall of *Mycobacterium bovis* is able to interact with Con A, a lectin derived from the the jack bean.[1] It is plausible that Con A should form an interaction between the arabinogalactan, a biopolymer consisting of arabinose and galactose monosaccharides on the mycobacterial cell wall, and modified chitosan, which is also a carbohydrate.[2]

In terms of the detection methods:

The polymerase chain reaction (PCR) was used as a technique for which to detect if mycobacteria had been captured onto the surfaces of the SPMN nanocomposites. PCR is used to amplify a single copy or a few copies of a piece of DNA across several orders of magnitude, generating thousands to millions of copies of a particular DNA sequence, with high sesitivity.[3]

The conditions needed to assess PCR results are stringent and require careful optimization and control of parameters. More specifically, a suitable release buffer is required to remove the DNA to be amplified from the nano-substrate which has demonstrated the capture of mycobacteria. By adjusting the pH of the release buffer in such a way as to destabilize the ionic interaction between the affinity nano-substrate and mycobacteria, release of mycobacteria can be achieved. Microscopy tools such as FM, FE-SEM and TEM proved that mycobacteria had been captured onto the nano-substrate, but the PCR protocol which was used did not corroborate these findings. Future research should focus on the methodology and control of release between the nano-substrate and BCG, through careful optimization of a suitable release buffer so as to corroborate microscopy analyses with PCR.

7.3 References

1. Goldstein, I. J.; Misaki, A. *J. Bacteriol.* **1970**, *2,* 422-425.

2. Nothnagel, E. A.; Bacic, A.; Clarke, A. E*;* Springer Science & Business Media: 2012; .

3. Hadidi, A.; Candresse, T. *Viroids* **2003**, 115-122.

Addendum A

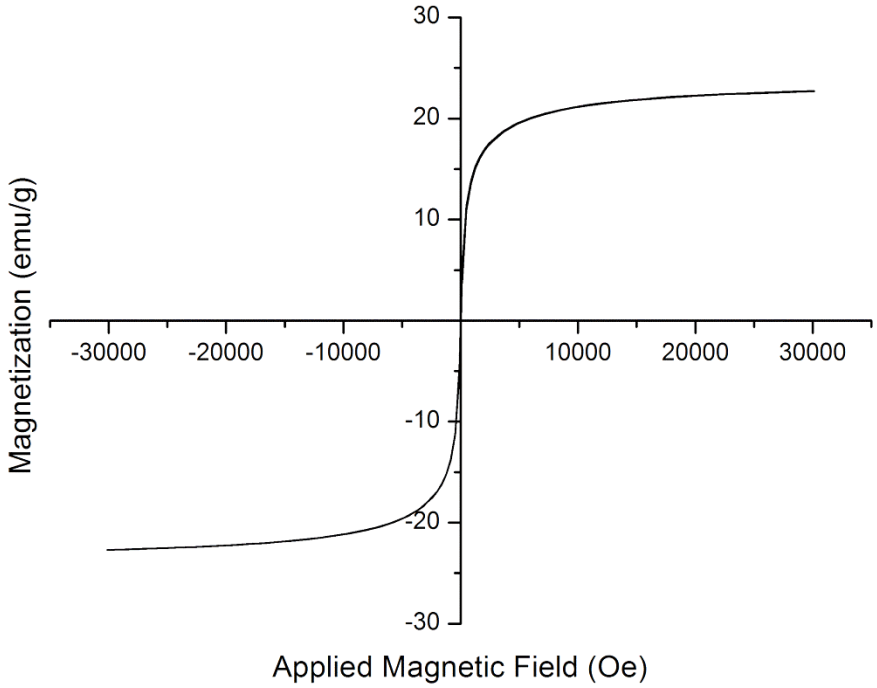

Figure A.1 Magnetization curve of TMC coated Fe_3O_4 nanoparticles demonstrating superparamagnetism.

Addendum B

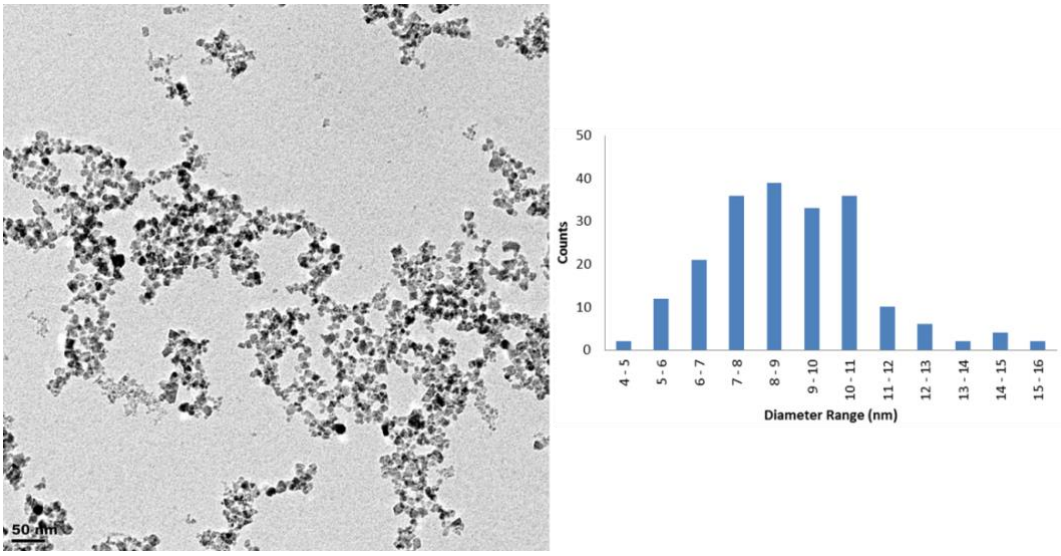

Figure B.1 TEM image and size distribution histogram of HTCC coated Fe_3O_4 nanoparticles

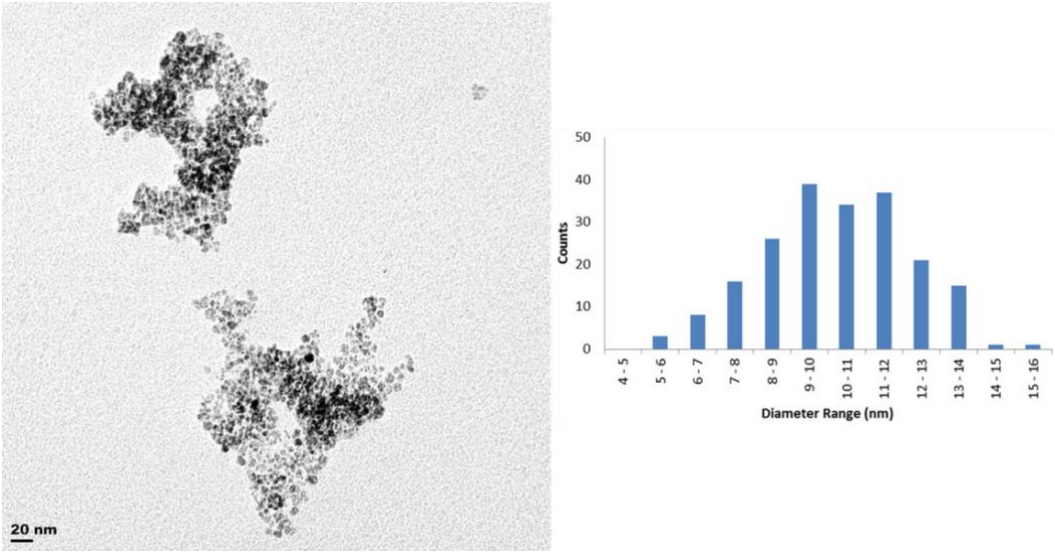

Figure B.2 TEM image and size distribution histogram of CS-qC_8 coated Fe_3O_4 nanoparticles.

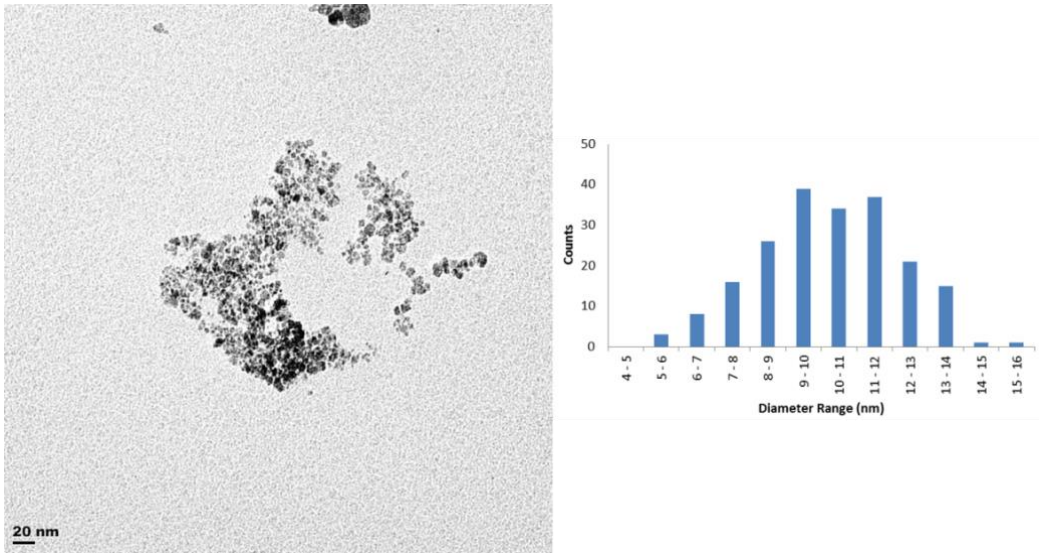

Figure B.3 TEM image and size distribution histogram of CS-qC_{10} coated Fe_3O_4 nanoparticles.

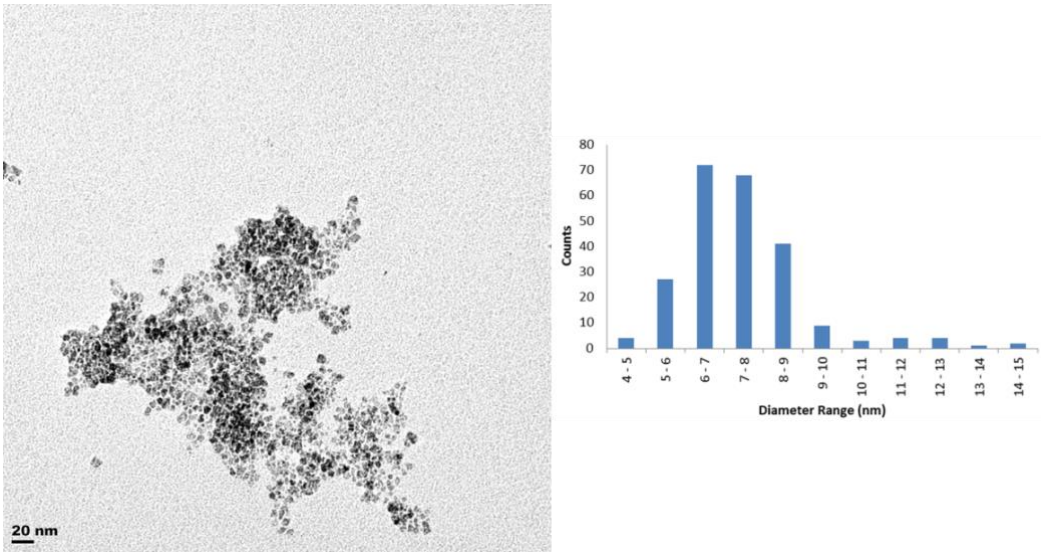

Figure B.4 TEM image and size distribution histogram of CS-qC_{12} Fe_3O_4 nanoparticles.

Addendum C

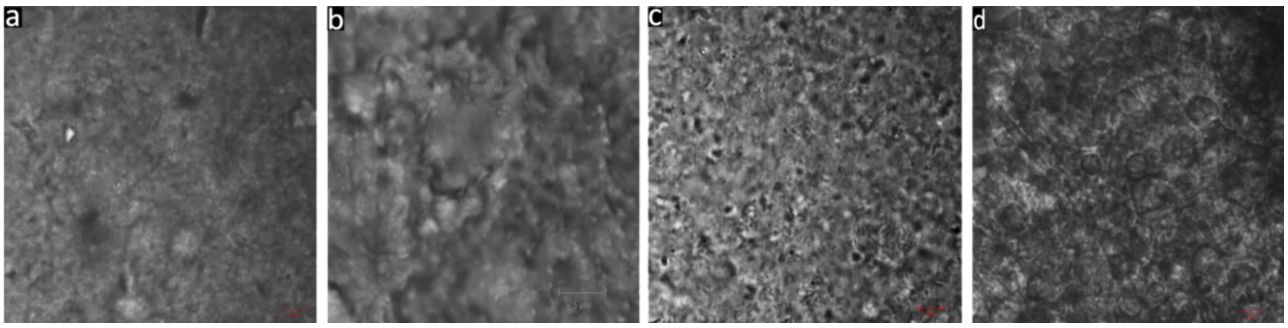

Figure C.1 FM and LM overlay images of (a) PVA/TMC nanofibers crosslinked with GA, (b) PVA/TMC nanofibers crosslinked with genipin, (c) PEO/TMC nanofibers and (d) PVP/TMC nanofibers washed in PBS and culture medium (no BCG) as negative controls.

Addendum D

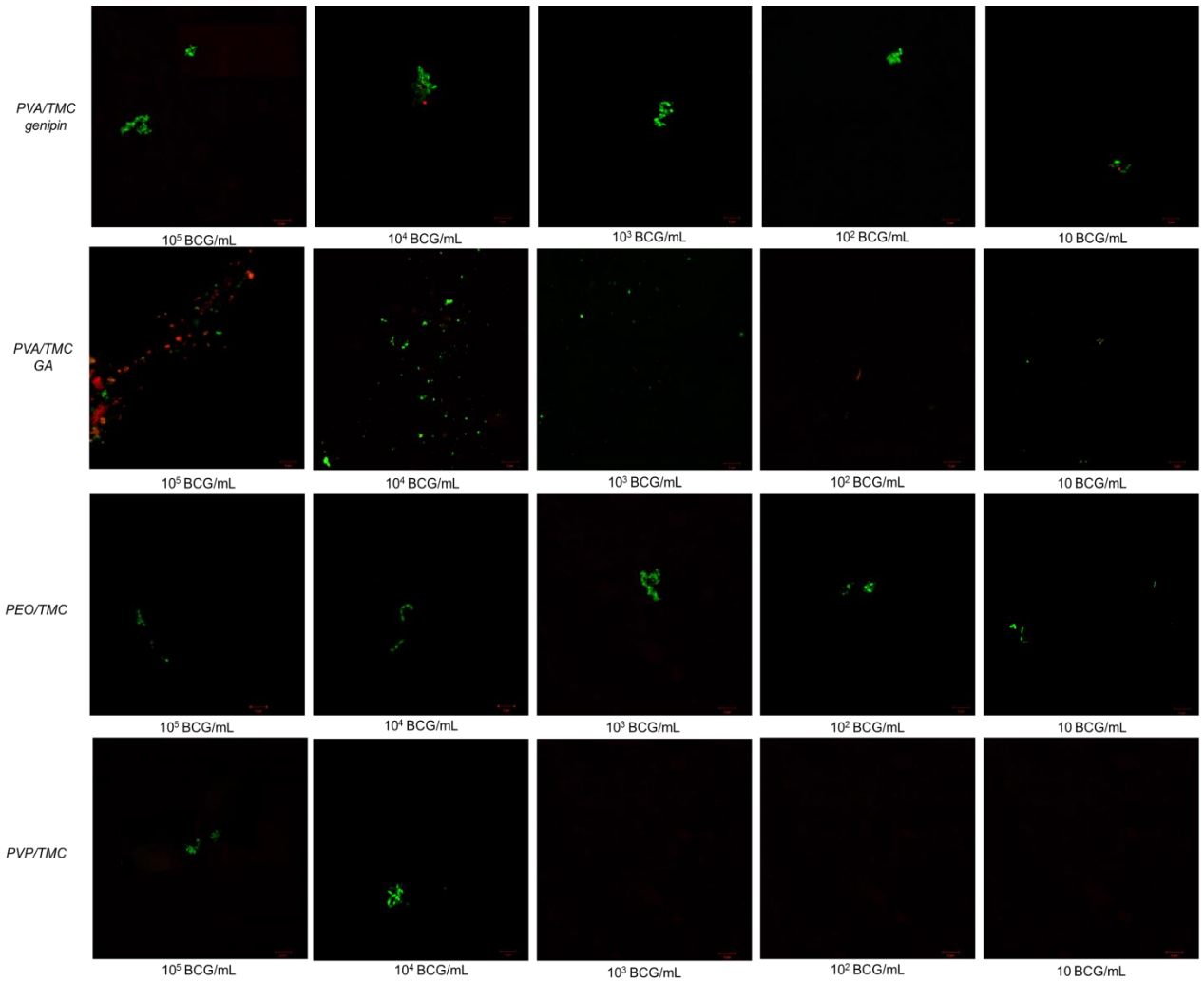

Figure D.1 FM images of modified chitosan based bi-component nanofibers incubated with BCG at various concentrations.

Addendum E

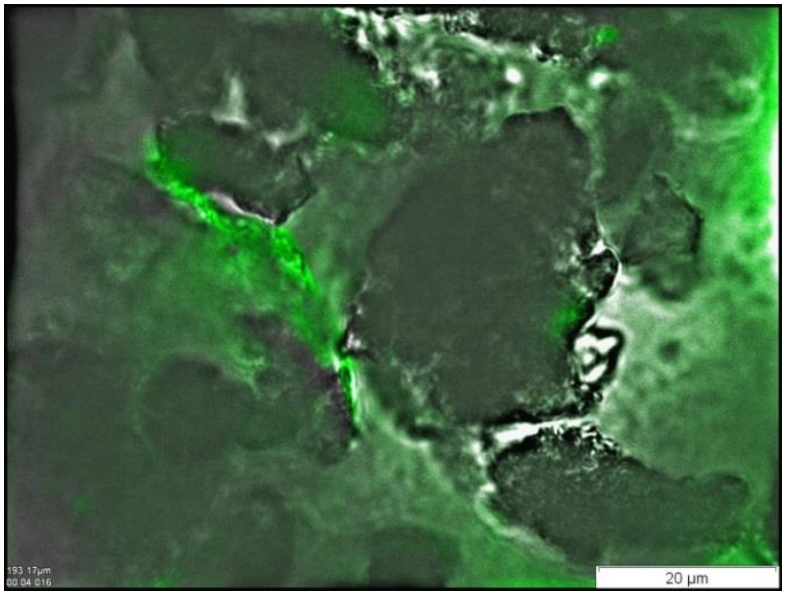

Figure E.1 Overlay of FM and LM image of TMC SPMNs having disparate fluorescence emission.

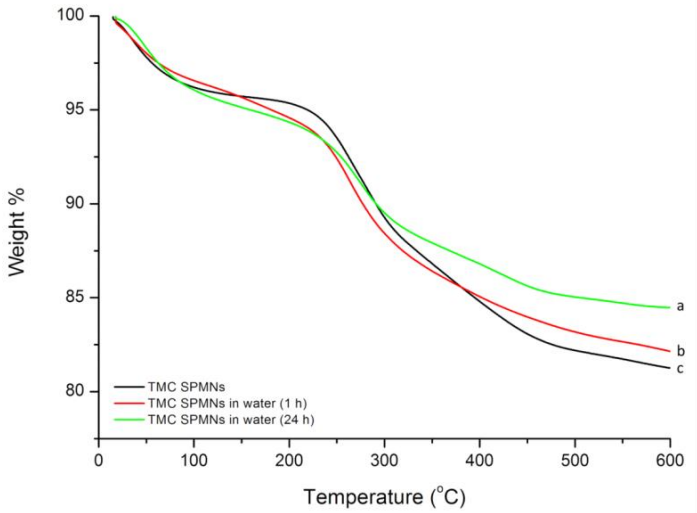

Figure E.2 TGA curves of (a) TMC SPMNs dispersed in water for 24 h and (b) TMC SPMNs dispersed in water for 1 h and (c) TMC SPMNs in dried form. There is a 1.1% and 3.2% decrease in polymer coating for the TMC SPMNs which were left in water for 1 h and 24 h, respectively.

Addendum F

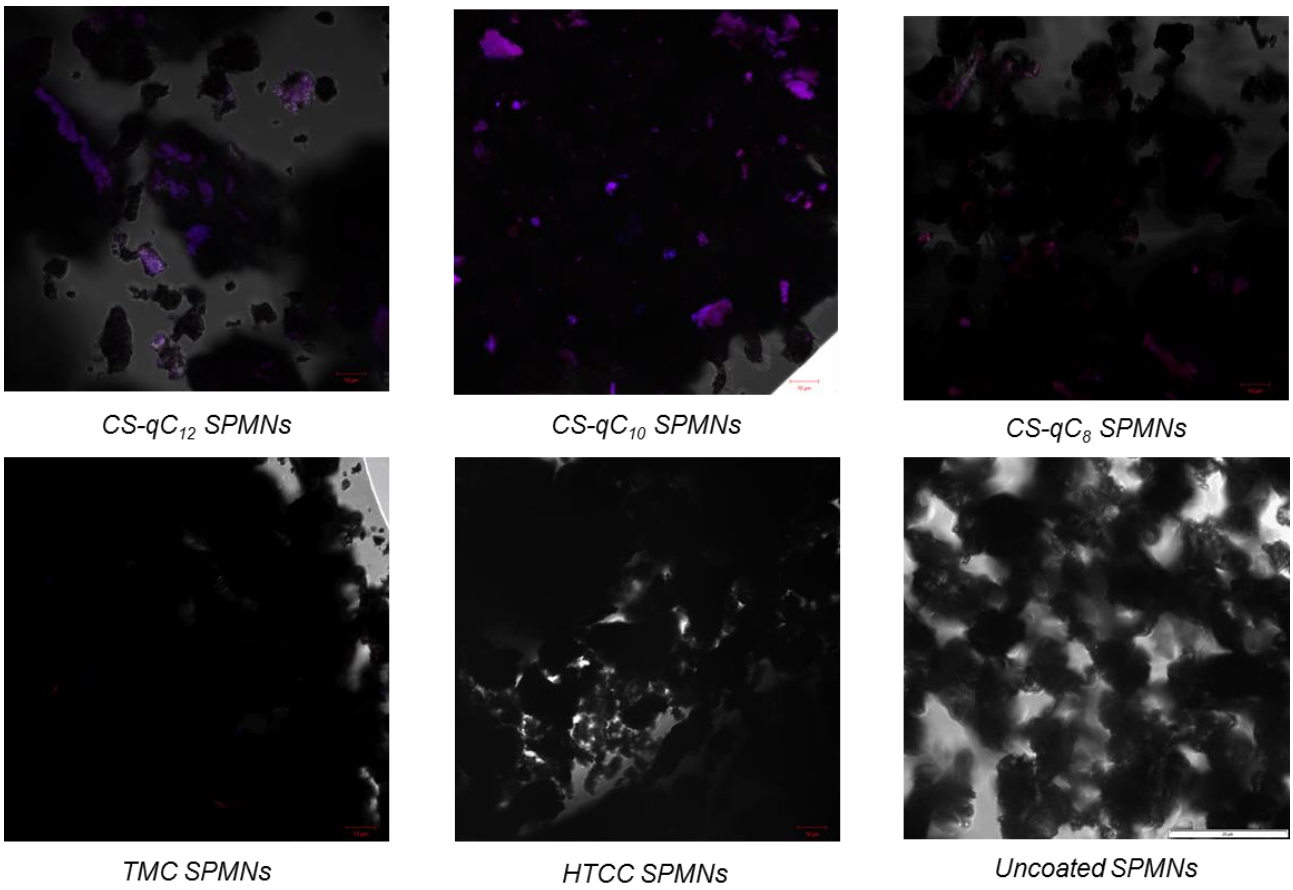

Figure F.1 FM and LM overlay images of modified chitosan coated SPMNs and uncoated SPMNs dispersed in PBS and 7H9 culture medium without any mycobacteria, as negative controls.

Addendum G

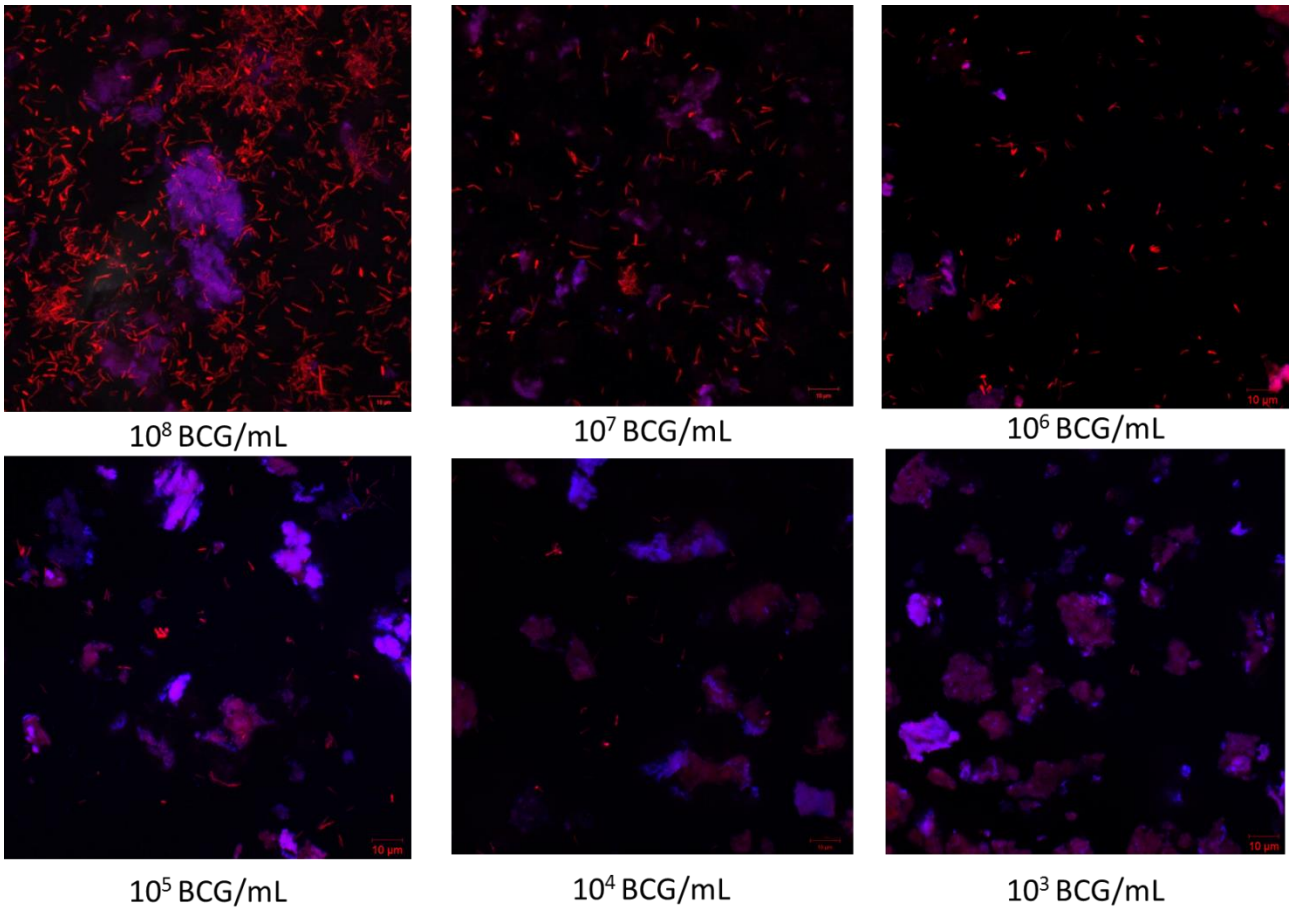

Figure G.1 FM images of CS-qC$_{12}$ coated SPMNs incubated with BCG at various concentrations.

‘